

# SOUND FROM SAND

A Dissertation

Presented to the Faculty of the Graduate School  
of Cornell University

in Partial Fulfillment of the Requirements for the Degree of  
Doctor of Philosophy

by

Danielle Sweimann Tan

January 2012

© 2012 Danielle Sweimann Tan  
ALL RIGHTS RESERVED

## SOUND FROM SAND

Danielle Sweimann Tan, Ph.D.

Cornell University 2012

Various methods of producing sound from 'sounding' sand in the laboratory are explored. Low amplitude sound with frequency similar to that of 'booming' during spontaneous avalanches was produced in a small inclined chute and rotating flask. Shearing of dried sand with a stylus, and pouring from buckets or shaking in a jar produced loud sound in 200-500Hz range. Dryness of the sand and flowrate have significant effect on the produced sound.

A model based on kinetic theory is proposed to explain the production of oscillations in avalanching flows. The avalanching layer behaves like a breathing mode with infinite wavelength, and perturbations in volume fraction allow oscillatory behaviour to be sustained in the inclined shear flow.

Finally, a phase transition model is used to explain the presence, and characteristics, of oscillations observed in numerical simulations of inclined flows near their stopping angle.

## **BIOGRAPHICAL SKETCH**

Danielle Tan hails from sunny Singapore. She majored in mechanical engineering at Imperial College London, and after nearly 10 years away from home finds autumn to be her favourite season. Her time at Cornell University has given her a little more insight into table-top experiments, and exactly how much time programming and debugging really takes. When free she loves playing the piano, joining others for Chinese dance, making greeting cards and singing when nobody is around.

To my beloved family, the fruit of your many years of support and  
encouragement.

## ACKNOWLEDGEMENTS

Heartfelt gratitude goes out to...

**the Tan family** for years of unwavering love and support. Without you there would not be me, let alone this dissertation.

**Jim Jenkins, Wolfgang Sachse & Steve Keast** for loads of help, advice, and companionship in the lab. Your time and advice, especially on the final stretch, were invaluable.

**Nathalie Vriend, Melanie Hunt & Natalie Becerra** for advice, suggestions and thoughts regarding 'booming' and 'burping' sand.

**Patrick Richard** for providing numerical simulations which aided in understanding and exploring inclined granular flows.

**Mark Shattuck** for assistance particularly with respect to modelling the phase transition in granular material.

**Itai Cohen** for insightful questions and comments.

**Hsiu-Yu Yu** for regular morale boosts and providing a listening ear at all times.

**Dan Mittler, Rick Schmidt & Corie Scott** for all the little ways you provided me with assistance, be it equipment, room-scheduling or friendly advice.

... and all the very many other people who have helped me out one way or another.

## TABLE OF CONTENTS

Biographical Sketch . . . . .	iii
Dedication . . . . .	iv
Acknowledgements . . . . .	v
Table of Contents . . . . .	vi
List of Tables . . . . .	viii
List of Figures . . . . .	ix
<b>1 Sound-Producing Sand</b> . . . . .	<b>1</b>
1.1 Review of Research on Sound-Producing Sand . . . . .	2
1.1.1 1900s - ‘Roaring’, ‘Humming’, ‘Booming’ and ‘Squeaking’ . . . . .	2
1.1.2 2004 - Rayleigh Waves, Resonance within Avalanching Layer, or Instability . . . . .	6
1.1.3 2007 - Waveguide model for ‘Booming’ . . . . .	10
1.2 Overall Picture . . . . .	13
<b>2 Granular Materials Used</b> . . . . .	<b>15</b>
2.1 Drying . . . . .	17
<b>3 Small-scale Inclined Chute Flow</b> . . . . .	<b>18</b>
3.1 Experimental Setup . . . . .	18
3.2 ‘Burping’ over Time . . . . .	20
3.3 Next Step . . . . .	22
<b>4 Large-scale Inclined Chute Flow</b> . . . . .	<b>23</b>
4.1 Experimental Setup . . . . .	23
4.2 ‘Burping’ over Time . . . . .	25
4.3 Conclusion . . . . .	27
<b>5 Rotating Flask</b> . . . . .	<b>28</b>
5.1 Motor-Rotated Flask . . . . .	28
5.1.1 Setup Sound Contribution . . . . .	30
5.1.2 Results . . . . .	32
5.2 Drill-Rotated Flask . . . . .	34
5.2.1 Results . . . . .	36
5.3 Conclusion . . . . .	37
<b>6 Perturbation Theory</b> . . . . .	<b>42</b>
6.1 Preliminary Model - Fully Dense Flow . . . . .	42
6.2 Equation Derivation . . . . .	46
6.2.1 Approximate Solution . . . . .	47
6.2.2 Matlab Solution Comparison . . . . .	48
6.2.3 Exact Solution . . . . .	49
6.2.4 Comparing Exact Solution to Experiment . . . . .	50

6.3	Second Model - Dense and Dilute Layers . . . . .	50
6.3.1	Two Hanging Chains . . . . .	53
6.3.2	Hanging Chain with Point Mass . . . . .	54
6.3.3	Comparing Theory to Experiment . . . . .	57
<b>7</b>	<b>Shearing with a Stylus</b>	<b>59</b>
7.1	Experimental Setup 1 - Baking Tray . . . . .	60
7.2	Experimental Setup 2 - Large Chute . . . . .	61
7.3	Experimental Setup 3 - Narrow Chute . . . . .	64
7.4	Conclusion . . . . .	66
<b>8</b>	<b>Pouring &amp; Shaking</b>	<b>70</b>
8.1	Pouring . . . . .	70
8.2	Jar Shaking . . . . .	72
8.2.1	Manual Jar Shaking . . . . .	72
8.2.2	Long Tube . . . . .	73
8.2.3	Controlled Shaking . . . . .	76
8.3	Summary . . . . .	79
<b>9</b>	<b>Phase Transition</b>	<b>84</b>
9.1	Homogeneous Phase Transition . . . . .	86
9.1.1	Cubic Curve . . . . .	87
9.1.2	Two Branches . . . . .	92
9.2	Non-homogeneous Phase Transition . . . . .	96
9.2.1	Discretised system . . . . .	99
<b>10</b>	<b>Summary</b>	<b>109</b>
<b>11</b>	<b>Future Work</b>	<b>113</b>
<b>A</b>	<b>Seismic Refraction Survey</b>	<b>116</b>
<b>B</b>	<b>'Depth-Average' PDE Approximate Solution</b>	<b>118</b>
	<b>Bibliography</b>	<b>120</b>

## LIST OF TABLES

5.1	Angular velocities corresponding to speed dial . . . . .	29
6.1	Lowest $a_0$ values for flow with dense and dilute layers, using hanging chain with point mass analogy. . . . .	56
6.2	Expressions for frequency; $A = \frac{1.20-\nu_0}{0.60-\nu_0}$ , $J_0^*$ are roots of $J_0(x)$ , $a_0$ determined numerically based on $h$ and $H$ values. . . . .	57
6.3	Lower mode frequencies for $d = 0.4\text{mm}$ , fitted parameter $\hat{c} = 0.50$ , $e_{eff} = 0.05$ , $\phi = 42^\circ$ , $\mu_w = 0.30$ , $\alpha = 0.70$ , and width= $25d$ . $h = 25.0d$ and $H = 8.88d$ are determined numerically. These parameters give $\nu_H=0.506$ , $A=7.38$ and $\nu_H=0.448$ , $A=4.95$ for the two-chains and chain-and-point-mass models respectively. . . . .	57
10.1	Experimental Results Summary - Avalanching and Shearing . . .	110
10.2	Experimental Results Summary - Pouring . . . . .	111

## LIST OF FIGURES

1.1	Douady et al's rotating blade experiment . . . . .	7
1.2	Waveguide Model used by Vriend et al. . . . .	12
2.1	Ottawa Sand - diameter 0.9mm; as seen under light microscope .	15
2.2	Eureka Dune Sand - average diameter 0.4mm; mean major to minor axis ratio 1.5, standard deviation 0.2; as seen under light microscope & LEICA 440 Scanning Electron Microscope respec- tively . . . . .	16
2.3	Dumont Dune Sand - average diameter 0.4mm; mean major to minor axis ratio 1.5, standard deviation 0.3; as seen under light microscope & LEICA 440 Scanning Electron Microscope respec- tively . . . . .	16
3.1	Small Inclined Slope Setup . . . . .	19
3.2	Frequency spectrum ratios of Eureka Dune sand (thick red line), glass beads (thin blue line) and Ottawa sand (dotted black line) over time . . . . .	20
4.1	The large inclined-flow setup . . . . .	24
4.2	Frequency spectrum ratios of Dumont dune sand and glass beads over time . . . . .	26
5.1	Rotating flask setup (max. sand volume) . . . . .	29
5.2	Frequency spectra of rotating flask containing different materi- als as rotation speed is increased and then decreased in steps ev- ery 15s. Counterclockwise from top right: empty flask, Dumont dune sand, glass beads . . . . .	31
5.3	Spectrogram and time-trace of rotating flask when motor is turned on and off. Spectra on the right are: (top) when the mo- tor is running but the flask is not included in the setup; (bottom) when the motor is on and the flask is rotating. . . . .	32
5.4	Frequency spectra when air is blown across flask mouth . . . . .	33
5.5	Frequency spectra when microphone is inside or outside rotating flask . . . . .	34
5.6	Frequency spectra of empty rotating flask, at different speeds . .	35
5.7	Frequency spectra of different materials in rotating flask, at dif- ferent speeds . . . . .	36
5.8	Eureka dune sand at speed '2' in rotating flask . . . . .	37
5.9	Eureka dune sand at speed '5' in rotating flask . . . . .	38
5.10	Eureka dune sand at speed '8' in rotating flask . . . . .	39
5.11	Drill-rotated flask setup . . . . .	39
5.12	Frequency spectra over time of Dumont dune sand in flask ro- tating at $\approx 100$ rpm . . . . .	40

5.13	'Power' in 105-150 Hz range over time of Dumont dune sand in flask rotating at $\approx 100$ rpm, for 2 experiment runs . . . . .	41
6.1	Schematic for fully-dense inclined shear flow perturbation model	43
6.2	Schematic of inclined shear flow with both dilute and dense layers	52
7.1	Stroking stylus through sand . . . . .	59
7.2	Frequency spectra ratios from stroking different styluses in baking tray . . . . .	60
7.3	Baking tray for stroking experiment . . . . .	61
7.4	Time progression of stroking frequency spectra in baking tray . .	62
7.5	Frequency spectra with depth of sand bed in baking tray . . . . .	63
7.6	Large chute with styluses for stroking experiment . . . . .	64
7.7	Frequency vs position in large chute . . . . .	65
7.8	Frequency vs stylus depth in large chute . . . . .	66
7.9	Frequency at different stroke velocities in large chute . . . . .	67
7.10	Frequency and amplitude at different stroke velocities in large chute . . . . .	68
7.11	Narrow chute for stroking experiment . . . . .	68
7.12	Frequency spectra of different styluses in narrow chute . . . . .	69
8.1	Spectrograms of poured Dumont dune sand at increasing flowrates (0.88kg/s in top left spectrogram, increasing down the column and the next to 5.0kg/s in the bottom right spectrogram.)	71
8.2	Frequency spectra of the portion of the signals where the frequency has decreased to a steady value. Each spectra corresponding to a different flowrate is displaced by a decade for clarity.	72
8.3	Peak frequency during pouring at different flowrates . . . . .	73
8.4	Peak frequency amplitude at different flowrates . . . . .	74
8.5	Large displacement shaking sequence . . . . .	74
8.6	Jar of dried Dumont dune sand . . . . .	75
8.7	Frequency spectra ratios of shaken jars of Eureka dune and Ottawa sand . . . . .	75
8.8	Spectrogram of shaken jar of Dumont dune sand . . . . .	76
8.9	Spectrogram of shaken jar of glass beads . . . . .	76
8.10	Glass tube 3ft long, 1.62inch diameter . . . . .	77
8.11	Spectrogram and time-trace when tube is tilted from horizontal to vertical . . . . .	77
8.12	Shaker with mounted glass jar . . . . .	78
8.13	Microphone signals of Dumont dune sand and glass beads at different shaking frequencies . . . . .	78
8.14	Microphone signals of Dumont dune sand and glass beads shaken at 50 Hz with increasing excitation amplitude (lowest at bottom) . . . . .	79

8.15	Original Dumont dune sand signal displaced +0.2V; below: difference in signal between Dumont dune sand and 'empty' jar, shaken at 50 Hz. . . . .	80
8.16	Original glass beads signal displaced +0.2V; below: difference in signal between glass beads and 'empty' jar, shaken at 50 Hz. . . .	81
8.17	Spectrogram of signal difference between Dumont dune sand and 'empty' jar, shaken at 50 Hz . . . . .	82
8.18	Spectrogram of signal difference between glass beads and 'empty' jar, shaken at 50 Hz . . . . .	83
9.1	Oscillations in kinetic energy at different particle stiffnesses; reproduced with permission from Richard et al.[29]. . . . .	85
9.2	Homogeneous phase transition model . . . . .	86
9.3	Cubic relationship between $p/\rho_s T$ and solid volume fraction $\nu = \nu_0 + \nu_1$ , going from a random collisional regime to an ordered collisional regime as $\nu$ increases. The horizontal line indicates the current force-equilibrium value $p_0/\rho_s T_0$ , and the corresponding three force-equilibrium points. Placing the origin at one of these points gives $p_1/\rho_s T_0$ against $\nu_1$ . . . . .	88
9.4	Relationship between pressure fluctuation and volume fraction fluctuation when steady state corresponds to a stable force-equilibrium point. . . . .	89
9.5	Relationship between pressure fluctuation and volume fraction fluctuation when steady state corresponds to an unstable force-equilibrium point. . . . .	90
9.6	Excursions in $\nu$ for steady states $\nu_0=0.580$ (solid line), 0.605 (dashed line) and 0.620 (dotted line). Local maxima is at 0.598. . . .	91
9.7	Relationship between $p/\rho_s T$ and $\nu$ , with cubic curve representing collisional regime and monotonic curve representing contact regime. The horizontal line corresponds to the steady state ratio $p_0/\rho_s T_0$ for inclination $\phi$ , at which $p_1=0$ . . . . .	92
9.8	Relationship between $p/\rho_s T$ and $\nu$ . For $\nu \geq \nu^*$ the curve is the sum of the cubic curve representing collisions and the straight line representing particles in contact. The horizontal line shows the steady state ratio $p_0/\rho_s T_0$ at inclination $\phi$ , and the corresponding three force-equilibrium points. . . . .	93
9.9	Fluctuations in kinetic energy corresponding to small perturbations about the unstable force-equilibrium point $\nu_b=0.621$ . The other equilibria are at $\nu=0.581$ and 0.700, and $\nu^{ast}=0.603$ . Particle stiffnesses $K = 2 \times 10^4, 2 \times 10^5$ and $2 \times 10^6$ mg/d (blue, green and red lines). . . . .	95

9.10	Oscillations in kinetic energy corresponding to small perturbations about the unstable force-equilibrium point $\nu_b$ . Here $\nu^*$ is taken to be 0.05 of the distance from the local maxima to $\nu_b$ . Stiffness is $K=2\times 10^4$ mg/d; equilibrium points are $\nu=0.581, 0.621$ and $0.700$ ; and the initial conditions are $\nu_1 = 3(\nu_b - \nu^*)$ , and $\dot{\nu}_1 = 0$ . Total flow depth $H = 40d$ (dotted line), $80d$ (dashed line) and $160d$ (solid line) respectively. . . . .	96
9.11	Non-homogeneous phase transition model . . . . .	97
9.12	Volume fraction fluctuations against time. $\nu_a = 0, \nu_b = 0.04, \nu_c = 0.119$ . . . . .	101
9.13	Volume fraction fluctuations against time. $\nu_a = 0, \nu_b = 0.0002, \nu_c = 0.0012$ . . . . .	102
9.14	Steady state results and predicted solution for $\nu_a = 0, \nu_b = 0.0002, \nu_c = 0.0012$ . . . . .	103
9.15	Volume fraction fluctuations against time. $\nu_0 = 0.5993, \nu_a = -0.0002, \nu_b = 0, \nu_c = 0.001$ . Initial perturbation in $\nu_1$ varies linearly from 0.0001 at base to 0 at surface. . . . .	104
9.16	Steady state results and predicted solution for $\nu_a = -0.0002, \nu_b = 0, \nu_c = 0.001$ . . . . .	105
9.17	Volume fraction fluctuations against time for varying $T_0$ . $\nu_a = 0, \nu_b = 0.0002, \nu_c = 0.0012$ . . . . .	107
9.18	Volume fraction fluctuations against time for varying $T_0$ . $\nu_a = -0.0002, \nu_b = 0, \nu_c = 0.001$ . . . . .	108
A.1	Seismic Refraction Survey . . . . .	117

## CHAPTER 1

### SOUND-PRODUCING SAND

The song of 'booming' sand is a phenomenon that has appeared in many legends - as the tolling of unseen bells or the audible anger of mighty desert spirits. Bagnold[4] described it as a 'vibrant booming so loud' that shouting was necessary, which set off other sand dunes nearby resulting in 'a slow beat' which lasted 'for more than five minutes continuously'. Other sources have compared 'booming' to the low rumbling of airplane engines [24, 32]. This low frequency sets the phenomenon apart from the high frequency sound produced by 'squeaking' or 'singing' sand, which is commonly found on beaches and can be provoked simply by walking across when the sand is wet. 'Booming' sand locations are more rare, with only 27 known locations reported in 1976, and 4 more found a decade later [32, 35].

Comparison of the sand from various 'booming' locations have turned up no distinguishing characteristics that set such sand apart from 'silent' sand, i.e. sand without the capability of 'booming'. It has been noted however, that all 'booming' sands are moderately rounded and rather well-sorted. This is not to say that these are strict or sufficient conditions, as perfectly round glass spheres of constant size are unable to 'boom', and microscope images of some 'booming' sand grains clearly show angular grains. It does appear to be necessary for the sand to be extremely dry, as prolonged exposure to a humid atmosphere over time reduces the sand's ability to 'boom', which may be restored upon heating [4, 35, 37].

From recent research, we now know that low frequency sound can also be produced in the laboratory [10], but this is more properly characterised as 'burp-

ing', because the mechanism by which it is produced is different from that of 'booming' [37]. However, when 'booming' was first investigated this distinction was not known and all low frequency sound production was considered to be a single phenomenon.

## **1.1 Review of Research on Sound-Producing Sand**

### **1.1.1 1900s - 'Roaring', 'Humming', 'Booming' and 'Squeaking'**

Lewis [18] was one of the earliest to study the phenomena of 'booming' sand in nature. He separated it into two different sounds - 'roaring' and 'humming'. The lower frequency 'roar' could be produced by 'pushing the sands forward in a heaped-up manner', while 'humming' was produced when the sand was kept moving slowly down a slope. In fact, 'roaring' could be produced by a person sliding down a slope in jerks; the more violent the push and the greater the mass of sand disturbed, the louder is the roar'. Unsurprisingly as long as the sand was still moving, the 'roar' would be followed by the 'hum'.

Lewis attempted to identify the frequencies of these two sounds using a set of tuning pitch pipes - 'roaring' at low C (132 Hz) and 'humming' near D (297 Hz). However, these are only approximate frequencies because of the presence of overtones and noise. Sieving the sand, Lewis found them to have almost double the concentration of sands within 0.0059-0.0082 inch (0.15-0.21 mm) range, as compared to non-booming sand (74% vs 40%), and very few fine particles (8% vs 43%). He also found the grains to be 'perhaps slightly less angular, more rounded, and of a more uniform size and shape'.

Local inhabitants of the Kalahari desert were of the opinion that 'the sands roar much better after a long spell of dry weather and not at all well shortly after rain', and indeed Lewis' observations confirmed this view. Measuring the water content of sand samples that he brought back with him, he found their hygroscopic water content to be 0.012%, compared to sand which could not 'roar' with 0.03% content. Also, it was discovered that the sand samples brought back from the desert lost their ability to 'roar' very rapidly. Lewis was able to recover the ability by heating the sand in an oven, but the restored 'roar' could only be preserved if the heated sand was then sealed in glass jars. These jars, if rotated about their axis at a speed of 120-150 rpm, could produce a 'continuous roar', likened to the 'frictional noise of a dry wooden bearing'.

Lewis theorised that the 'roaring' could be due to electrical effects, as the 'roaring' sand exhibited these, but grounding the jars did not eliminate its ability to 'roar'. Another idea he considered was that the sand had a special mechanical makeup, but he found that sands from other sources could also produce 'roaring', after heating and sealing in jars - he even claimed to be able to do so with common salt. Lewis' final theories about 'roaring' were that it was due to a series of 'explosions of air trapped by breakers', or that it was the 'formation of a series of slip planes throughout the sand, alternating with a jump and a slump to natural angles of repose'. He noted however, that the post-avalanche angle of repose and packing fraction of 'roaring' sand were no different from that of non-'roaring' sand.

Poynting and Thomson [27] theorised that the relative motion of layers of grains resulted in the total volume undergoing a cyclic motion with the frequency corresponding to that of the emitted sound.

Bagnold [4] was unable to determine any common characteristics between 'whistling' and 'booming' sands, and similarly could not identify any distinct characteristics that 'booming' sand had that set it apart from 'silent' sand. He concluded that 'booming' sands were 'reasonably rounded' and 'uniform in size, but not more so than 'silent' sand'. He also found that Lewis' observation of the sand being 'cleaner' by not having very fine particles did not hold true for 'booming' sand in the Libyan desert, which in fact was dirtier - it had a larger deposit of iron oxide than the 'silent' sand in the vicinity.

Observing spontaneous avalanches in the Libyan desert, Bagnold noted that the 'booming' sound seemed to be emitted from the lower part of the avalanche, and began when the avalanche front encountered a decrease in slope at the base of the dune, causing the avalanche to be slowed and the following sand to pile up on top of it. He guessed the surface velocity to be 12 cm/s, and the 'booming' frequency to be 132 Hz. Bagnold found that he could artificially produce a similar sound by 'rocking a bottle around the base of a heap of 'booming' sand'. This artificially produced sound never started until after a few bottle movements were made, and a certain amount of downward force had to be applied. He estimated this force to be approximately the weight of 8-10 layers of sand.

Seeing that 'whistling' and 'booming' sands could have the same grain diameter, Bagnold concluded that the frequency of sound emitted was determined by the speed of the disturbance, because 'whistling' sand could not 'boom' and vice-versa. He also noted that only a small amount of 'whistling' sand needed to be disturbed to emit a sound, while a considerably larger mass was required for 'booming'. This led him to the theory that the narrow range of disturbance speeds for each sand, was a function of the mass disturbed and some unknown

grain property, perhaps the molecular surface structure.

Bagnold proposed that 'booming' could be produced as a result of the disturbance in a sand mass being relieved by slipping along a series of instantaneous shear planes. He also considered the possibility of an accumulation of electric charges in the avalanche through alignment of the grains' axes after continuous rolling.

Unlike Lewis' definition of 'roaring' and 'humming', Humphries [11] defined 'booming' sand as that which emits a 'low-pitched note of considerable magnitude and duration when induced to slide'. This sound starts nearly immediately upon stamping or sliding on the dune, and continues until the sand motion ceases. Humphries describes the motion of 'booming' sand as small-scale eddying superimposed on the overall downwards movement of the flowing sand, the thickness of which was about four inches. He also estimated the mean surface velocity to be 10 cm/s, and the frequency of the 'booming' to be between 50-100 Hz, with a beat frequency of approximately 1 Hz; while 'singing' sand had a frequency of about 1 kHz.

Comparing 'booming' sand from Korizo in the Sahara Desert with 'singing' or 'squeaking' sand found on the beach of Gower, South Wales, Humphries found that both sands were relatively well-sorted - the 'singing' sand more so than 'booming' sand - and that both had similar roundness - but were not as well-rounded as expected. In terms of their composition, both sands were very similar - mostly quartz with some small percentage of iron. They both had similar mean diameters of 0.26mm and 0.31mm respectively, with almost no fine material (less than 0.14mm diameter) present. Humphries believed that a relationship exists between the packing of the sand and sound production, but was

not sure whether the sound was produced as a result of the air volume changing with the changes in packing, or as a result of inter-particle collisions. He was also unable to explain the presence of the beats in the 'booming'.

As a whole, while 'booming' sands were found to be moderately rounded and rather well-sorted, they did not have any characteristics to distinguish them from 'silent' sands. The sand had to be very dry to produce 'booming', the sound produced during spontaneous avalanches estimated to be between 50-130 Hz, with the avalanche surface velocity at 10-12 cm/s.

### **1.1.2 2004 - Rayleigh Waves, Resonance within Avalanching Layer, or Instability**

Douady et al. [10] and Andreotti [2] first observed the 'booming' phenomena in Ghord Lamar, a desert in Tarfaya, Morocco. They proposed that the frequency of 'booming' is a function of grain diameter, as each dune field had a characteristic grain diameter and 'booming' frequency. Using data from [19] and [24], they verified the relationship  $f \propto \sqrt{g/d}$ . It was also noted that while gravity determines the frequency in spontaneous avalanching, triggering the avalanching by hand, leg or by pushing a plate results in different frequencies. Douady et al. dismissed resonance of the sand dune as a possible mechanism for 'booming', because the same 'booming' frequency could be obtained at different locations on one dune, and from different-sized dunes in the same dune field. Stick-slip was also eliminated as a mechanism because the grain motion during 'booming' was that of dry grains flowing unrestrictedly.

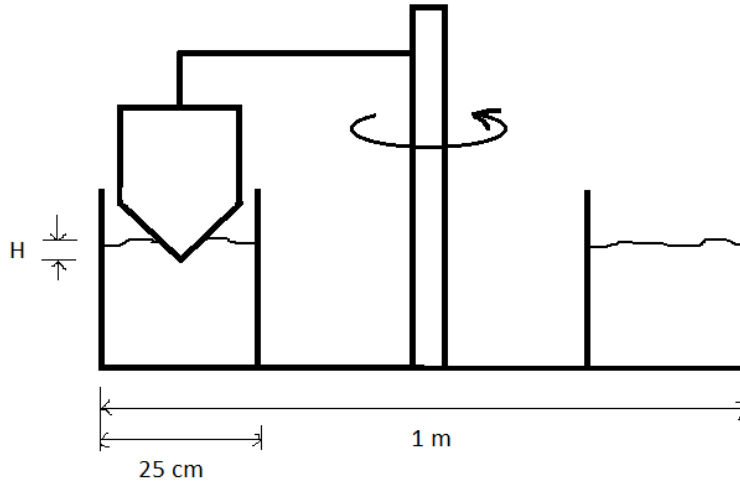


Figure 1.1: Douady et al's rotating blade experiment

Observation of a 'steady' granular flow in a laboratory setup of fixed width led them to approximate the velocity profile as linear. They theorised that the grains passed over each other and collided with the grains below periodically, so that eventually the energy balance between the kinetic energy gained through the overall downward motion and the energy lost during the collisions results in the layers of grains flowing with constant relative velocity [28]. This resulted in a linear velocity profile, the constant velocity gradient being the average collision frequency  $\Gamma \propto \sqrt{g/d}$ , measured to be  $100 \pm 5\text{Hz}$  [2] for grains of  $180\mu\text{m}$  diameter. This was exactly the same as the 'booming' frequency they measured in the desert, so it was naturally assumed that the two frequencies were intimately related, leading to the relationship  $f \approx \Gamma = 0.4 \sqrt{g/d}$  [2, 10].

Douady et al. performed two separate experiments [10], one in the laboratory and the other in the desert. The laboratory experiment consisted of a blade on a rotating arm, which could push sand in a circle (Figure 1.1). The depth  $H$

of the blade below the sand surface, and the angular velocity of rotation were varied as indications of how the mass of sheared sand and shearing velocity affected the 'booming' frequency. 'Constant and well-defined' frequencies ranging from 100-350 Hz were obtained as the blade depth and angular velocity were varied, supporting their theory that the sand dune itself is not required as a resonator. Because the same 'booming' frequency could be obtained for various combinations of velocity and depth, Douady et al. concluded that the frequency is dependent on the mean applied shear rate (the ratio of shearing velocity to depth of blade in sand).

In contrast to Bagnold's [4] and Humphries' [11] estimates of surface velocity, Douady et al. [10] detected no audible 'booming' below a surface velocity of 47 cm/s. They claimed that at this surface velocity threshold, various 'booming' frequencies and depths were possible, as long as their product (mean shear velocity) was constant. A channel 0.45m wide by 3m long was constructed in the desert to observe whether a surface velocity threshold was also present. Sand was accumulated behind a gate to a particular height above the dune surface and the gate was then removed suddenly to release the sand in a controlled avalanche. For this experimental setup, the surface velocity threshold was 23 cm/s in the middle of the channel. Douady et al. explained that the different velocity thresholds were due to the different boundary conditions in the two experiments: the channel in the desert had a free surface; while, in the blade experiment, the sheared layer was between a pushed mass and the static sand below.

Douady et al. theorised that some mechanism exists which synchronises adjacent layers of grains, and propagates through the depth of the avalanching

layer at a velocity  $c$ , dependent on the characteristics of the sand and external factors. The different periods of the mechanism and characteristic grain motion result in a threshold surface velocity, below which the mechanism cannot propagate through the avalanching layer.

This synchronising mechanism theory implies that all sand has the capability to 'boom', as long as it is dust-free, sufficiently dry, and possess a particular surface state. This criterion appears to be supported by the fact that after lengthy or intensive use, previously 'booming' sand can no longer produce sound.

On the other hand, Andreotti[2] asserted that the synchronisation of the grains in the avalanche was associated with elastic waves at its base. This theory was based on accelerometer measurements obtained from avalanches in the desert. Comparing the measurements from accelerometers at different depths, Andreotti noticed that the amplitude of vibration decreased rapidly, over a typical length scale of 10cm. This suggested elastic waves localised at the surface of the avalanche, like Rayleigh waves. Next, comparing two accelerometers on floaters, cross-correlation of their measurements showed a nearly constant phase difference which changed sign after the avalanche. Andreotti thus concluded that the surface waves were produced by a source within the avalanche itself.

Assuming that Rayleigh waves of frequency  $f$  were present, Andreotti theorised that a feedback loop exists in which the waves in the avalanching layer are excited by the collisions within a shear band located between the avalanching layer and the static part of the sand dune. The oscillation of the avalanching layer at a frequency  $f$  close to the sand grain collisional frequency  $\Gamma$  induces a force driven at frequency  $f$  in the sheared layer which then synchronises the

collision of the sand grains.

Andreotti also proposed a slightly different, alternative explanation, in which the avalanching layer is considered a rigid body sliding on top of the static dune, with a very thin, frictional shear band between them [3]. Andreotti then set up a resonance system by applying displacements to the flow in both the normal and tangential directions to the flow. The elastic waves induced by these perturbations travel through both the rigid sliding layer and the static dune, coupling to each other across the shear band. Based on [25], maximum constructive interference will occur for reflected waves incident upon the shear band at a particular angle and hence amplifying a specific frequency. This theory treats the system from a solid mechanics point of view, with the stiffness derived from elastic coefficients of granular material stiffness under shear and compression. The resulting selected frequency is hence dependent on these material stiffnesses, and the frictional coefficient  $\mu$ .

### **1.1.3 2007 - Waveguide model for 'Booming'**

Vriend et al.[37] triggered 'booming' in deserts using human sliders, and were able to record clear dominant 'booming' frequencies (70-105 Hz) with several harmonics. They compared their measured 'booming' frequencies at various deserts with the respective mean grain diameters (ranging from 0.18-0.31mm), and found that the frequency  $f$  did not vary inversely with  $\sqrt{d}$ , contrary to the two Paris groups above.

Vriend et al. discovered that 'booming' was only possible during certain times of the year - in September 2006 at Dumont Dunes, the dominant frequency

was 82 Hz, but in December 2006 no sound could be obtained. Using an array of 96 geophones to conduct a seismic refraction survey (see Appendix), they found that the dunes' internal velocity structure varied over the year - in September the dunes had a distinct layered structure while in December the layering was continuous. They believe that moisture affects the density layering. Measurements using ground penetrating radar confirm the presence of internal layering.

Because Vriend et al.'s measurements indicated that 'booming' was possible when the dunes had distinct layered structures, they proposed a waveguide model with the layer beneath the top surface acting as the waveguide, and the avalanching sand as the energy source. Looking at a cross-section of a sand dune, the top-most layer of thickness  $H$  (sound velocity  $c_1$  and density  $\rho_1$ ) is sandwiched between the atmosphere (sound velocity  $c_0$  and density  $\rho_0$ ), and the substrate half-space (sound velocity  $c_2$  and density  $\rho_2$ ) below it. Figure 1.2 shows a sketch of this model. Point A represents a point on the descending wave just before reflection of the 1-2 boundary; point B is the point of reflection at the 0-1 boundary and point C is a point on the descending wave after two reflections, that lies on the same wave front that passes through point A.

With each reflection at a boundary, a phase loss is incurred which is related to the relative velocities in the two respective layers -  $\epsilon_{10}$  and  $\epsilon_{12}$  respectively [26]. Neglecting the aforementioned phase changes, the phase difference between points A and C would be  $2\pi(AB + BC)/\lambda_n$ , where  $\lambda_n$  is the wavelength corresponding to the  $n$ th mode and  $\phi$  the angle of incidence. Using geometry this simplifies to  $4\pi H \cos \phi f_n / c_1$ . For maximum sound amplification, i.e. constructive interference, the total phase difference has to be a multiple of  $2\pi$ :

$$\frac{4\pi H \cos \phi f_n}{c_1} - \epsilon_{10} - \epsilon_{12} = 2n\pi . \quad (1.1)$$

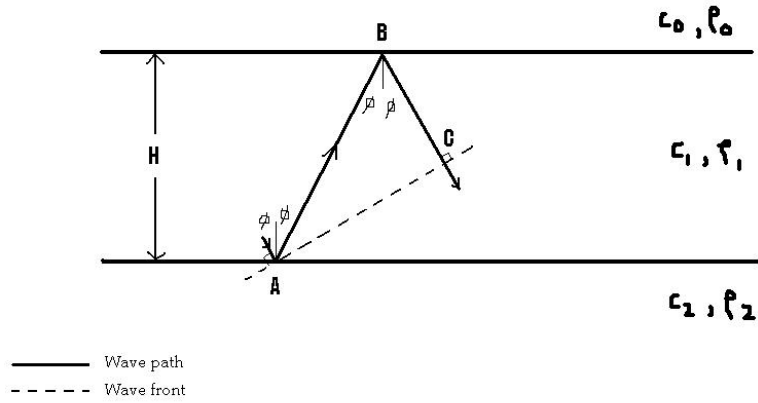


Figure 1.2: Waveguide Model used by Vriend et al.

When the angle of incidence is at critical value, the phase change upon reflection is zero. If the velocities of the atmosphere and substrate half-space are the same, both  $\epsilon_{10}$  and  $\epsilon_{12}$  are zero simultaneously, and  $\phi_{cr} = \arcsin(c_1/c_2)$ . The frequencies of the various modes are then computed as:

$$f_n = \frac{nc_1}{2H \sqrt{1 - c_1^2/c_2^2}}. \quad (1.2)$$

Vriend et al.'s measured sound velocities show that the assumption  $c_0 = c_2$  was satisfied at some locations and, indeed, the sound amplitudes were greatest there. Vriend et al. compared two different avalanching speeds and found no significant difference in frequency, which supports their theory that the 'booming' frequency is entirely a product of the waveguide.

Upon filtering the signals obtained from the geophones, they found that there were two different components in the sound. While both signals had longitudinal waves and Rayleigh waves, the lower frequency (50-60 Hz) component was dominated by Rayleigh waves, while the higher frequency (70-100

Hz) component was dominated by longitudinal waves. The higher frequency component was determined to be the one corresponding to 'booming', while the other (called 'burping' by them) was assumed to be the initial source of energy required for the waveguide.

## 1.2 Overall Picture

Vriend[37]'s work appears the most complete and is able to relate the other research currently presented. What Douady et al[10] and Andreotti[2] call 'singing' would correspond to 'burping' in Vriend's theory, and their mechanism of production would involve Rayleigh waves.

The perturbation theory we present later focuses on the avalanching layer being the source of 'burping', which could potentially provide the necessary frequency input for Vriend et al.'s [37] waveguide to produce 'booming'. It is also a more detailed explanation of the mechanism mentioned in Douady's [10] theory resulting in vibration of the avalanching layer, but taken from a continuum point of view.

We consider the avalanching layer as a shear flow, the instability of which causes a perturbation from the steady state. The avalanching layer consists of colliding grains; associated with the momentum transferred in these collisions is a particle pressure. This pressure resists changes in the solid volume fraction and sustains the perturbation of the steady, uniform distribution of the particle volume fraction in the form of a breathing mode. Expressions for the velocity, granular temperature and packing fraction which describe the steady state shear flow are obtained from kinetic theory; parameters like coefficient of resti-

tution and sidewall frictional coefficient are determined by fitting experimental data to the theory.

In physical experiments, we obtained audible low frequency sound (150-500 Hz) through various other means not involving avalanches, and so believe that although these sounds are in a similar range to ‘booming’, they are more closely related to ‘burping’ and are produced through a different mechanism which is unclear at this time.

Finally, we explore a model inspired by Silbert’s observations of oscillations in inclined flows near the stopping angle [33]. We theorise that the oscillations arise from an interrupted phase change at some depth in the flow. Decreasing inclination angle corresponds to increasing equilibrium packing fraction. Beyond a certain value of packing fraction, force chains are formed which interrupt the phase change between ordered and random packing, resulting in oscillations of significant amplitude. It is unclear, however, whether the oscillations produced with this model result directly in ‘burping’.

## CHAPTER 2

### GRANULAR MATERIALS USED

According to the literature [8, 17, 32, 37], high smoothness and well-sortedness (diameters of 0.18-0.31mm) are characteristics of ‘booming’ sand. Leach [17] describes it as being ‘non-spherical, but moderately rounded’. Ottawa sand (Figure 2.1), a known ‘silent’ sand, has high sphericity and smoothness, which matches the characteristics of ‘burping’ and ‘booming’ sand, so it was used to become familiarised with the experimental setup, and to identify any frequencies or phenomena due to the setup and surroundings.

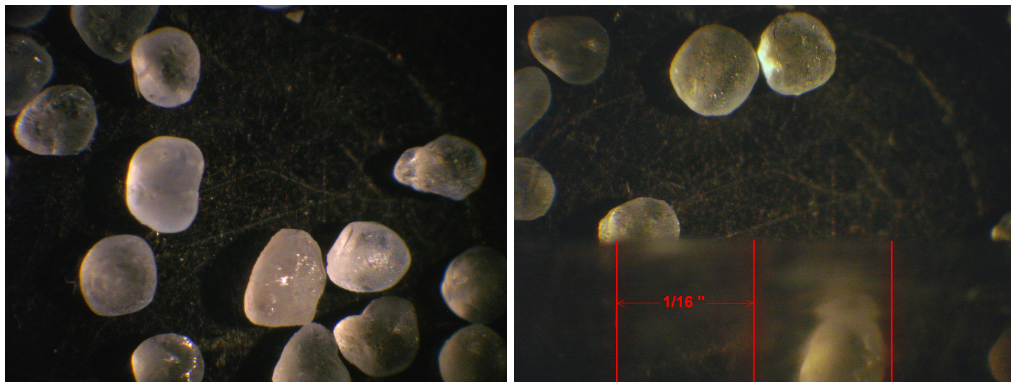


Figure 2.1: Ottawa Sand - diameter 0.9mm; as seen under light microscope

A sample of ‘booming’ sand originating from Eureka Dunes, California (Figure 2.2) was obtained from Vriend [37]. Contrary to expectations it was found to be rather angular, and not as well-sorted as expected from literature.

Another sample of ‘booming’ sand was later acquired from Dumont Dunes, California (Figure 2.3) for use in larger experimental setups, as the quantity of Eureka sand on hand was insufficient. The Dumont dune sand had a similar average diameter (0.4mm) to Eureka dune sand, and photographs showed it to

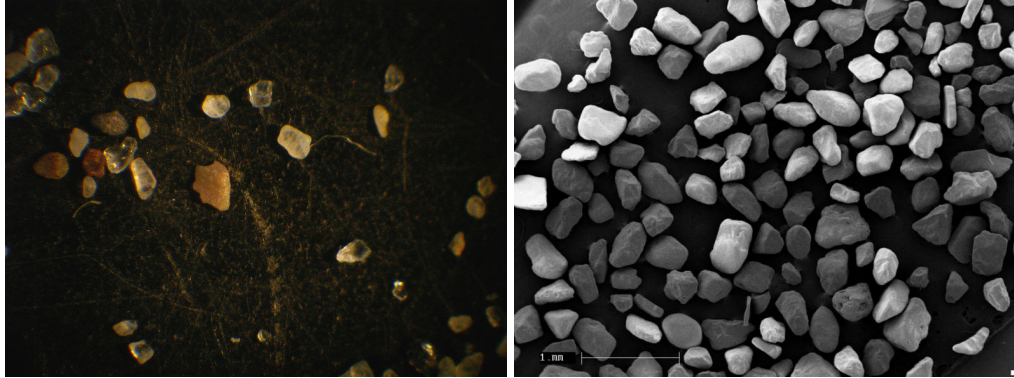


Figure 2.2: Eureka Dune Sand - average diameter 0.4mm; mean major to minor axis ratio 1.5, standard deviation 0.2; as seen under light microscope & LEICA 440 Scanning Electron Microscope respectively

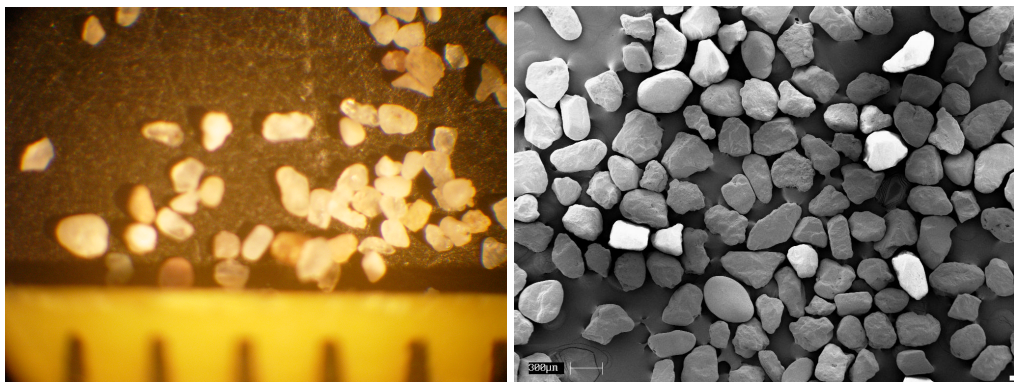


Figure 2.3: Dumont Dune Sand - average diameter 0.4mm; mean major to minor axis ratio 1.5, standard deviation 0.3; as seen under light microscope & LEICA 440 Scanning Electron Microscope respectively

be more uniform in size and roundness, but still not as round as Ottawa sand.

Due to the size difference between Ottawa sand and the two 'sounding' sands, glass beads of average diameter 0.4mm were acquired to be a better 'silent' comparison. Their spherical shape also provides an idea of the effect of particle angularity, reflected in the coefficient of friction.

## 2.1 Drying

Because of the observation that sound-producing sand has to have very low water content to 'boom' [17, 19, 32], all the sand samples were dried at 120°C for at least 24 hours (during summer when humidity is higher, 3 days' of drying produced better results). Written communication with Vriend [37] states her belief that a 'booming' sand can only 'boom' if it can 'burp', so the production of 'burping' was used as a check that the sand had been sufficiently dried.

One check was to have glass jars half full of the dried sand shaken in the jar's axial direction. Both Eureka and Dumont dunes sands would produce a loud 'burp' with every periodic cycle of the shaking motion if sufficiently dried.

Another method of checking was to stroke a thin metal paddle shallowly through the trays of dried sand. Audible 'burps' would be produced, lasting as long as each stroke.

Dried Dumont and Eureka sand, if stored in sealed glass jars, remained dry and produced audible 'burps' upon shaking for at least a month.

## CHAPTER 3

### SMALL-SCALE INCLINED CHUTE FLOW

Here and in previous literature, ‘booming’ and ‘burping’ are used somewhat interchangeably with respect to the sand, as sand that ‘booms’ must be able to ‘burp’. According to Vriend et al [37], the mechanisms by which both sounds are produced are different - ‘booming’ involves the body of the dune, while ‘burping’ involves the avalanching layer and not the dune. Hence, in our laboratory experiments, ‘booming’ could not be produced, and what we produced during our avalanching experiments was ‘burping’.

To obtain a better understanding of the ‘burping’ sand phenomenon, different sand samples flowing down an inclined slope in laboratory setups were studied. The sound generated when material was flowing was recorded via a microphone; the frequency spectra of the recorded microphone output were then divided by the frequency spectra obtained when there was no flow, to eliminate background noise. The literature indicates that the sound emitted during spontaneous or artificial avalanches is in the vicinity of 80-250 Hz [8, 10, 17, 19, 32, 37] hence the frequency range of interest is below 300 Hz.

In this setup, measurements of flow depth, surface inclination angle and approximate surface flow velocity were obtained.

### 3.1 Experimental Setup

Figure 3.1 shows the setup of the small-scale inclined chute flow. It is similar to the experiment conducted by Douady et al [10] in the desert, in that sand is

flowing over an inclined slope. However for our small setup instead of a build-up of sand behind a gate, sand flows from a hopper situated directly above, into an inclined cell (setup base is inclined at  $26^\circ$  to the horizontal) with glass walls and a bumpy base. A valve and nozzle constrain the flow rate into the cell. The cell-width is adjustable from approximately 12 to 50 grain diameters and a microphone is fixed above the cell to capture the sound produced.

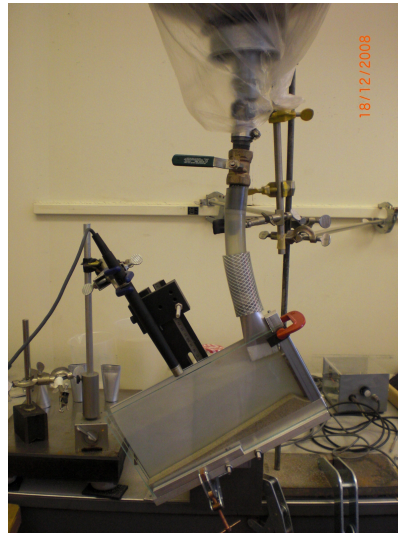


Figure 3.1: Small Inclined Slope Setup

A majority of the experiments with this small setup were conducted with a  $3/8$  inch cell-width (approximately 25 particle diameters), as the effect of the walls in the narrowest cell-width ( $3/16$  inch; 12 diameters) was considered to be too large. Using the largest cell-width ( $3/4$  inch; 50 diameters) and the maximum possible flow rate (valve fully opened) the depth of the avalanching layer was at most 10 diameters, which was considered to be too shallow a flow to produce 'burping'.

### 3.2 'Burping' over Time

Sound recordings of flowing sand were taken at intervals after the sand was initially dried, to see how its ability to produce sound was affected. With time, the water content of the sand would increase, and hence it was expected that the 'burping' would diminish and eventually disappear, only to reappear upon re-drying the sand.

Here and in the following sections describing experimental results, the frequency spectra are usually represented as ratios to the frequency spectra of the background noise.

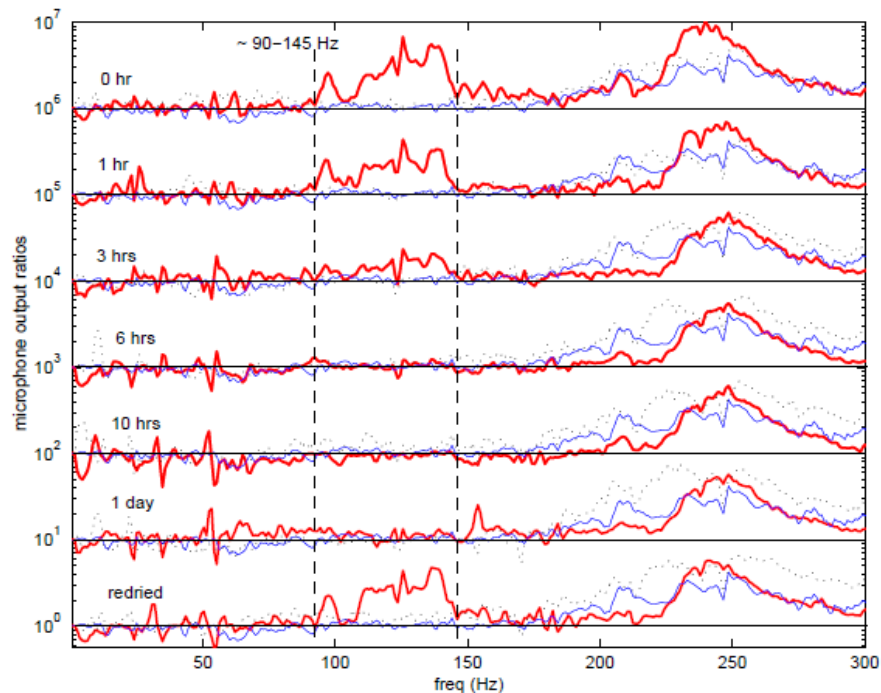


Figure 3.2: Frequency spectrum ratios of Eureka Dune sand (thick red line), glass beads (thin blue line) and Ottawa sand (dotted black line) over time

Figure 3.2 shows the frequency spectra ratios of material in the smaller setup,

as time after drying increasing. For clarity, the spectrum ratios are each displaced downwards by a decade at each time interval, with the top of the figure being the results obtained immediately after drying. The ratios corresponding to Eureka dune sand, Ottawa sand, and glass beads are overlaid at each time interval to examine the differences between the sands after they were all subjected to the same heating treatment.

From the frequency spectra, it was found that the sound produced by dried Eureka dune sand flowing down the incline had a broadband peak in the 90-145 Hz range, which neither Ottawa sand nor glass beads exhibited. It was concluded that this was 'burping', even though it was not audible.

Over time, the broadband peak seen in the frequency spectra of the Eureka dune sand diminished, but reappeared after re-drying the sand. This is further confirmation that the low amplitude sound was 'burping', and that low water content is a necessary requirement.

It was also found that this broad peak was present only at high flow rates, which appears to support Douady's idea of a surface velocity threshold (0.23m/s for avalanching in chute) [10]. All three materials shared a broadband peak in the region of 250 Hz, which was presumed to be a characteristic of the system when some material is flowing.

For Eureka dune sand flowing at the maximum flow rate, the flow depth was measured to be 20-25 diameters, surface inclination 40-48°, and surface velocity approximately 0.63-0.69m/s. Electrostatic effects are the most likely reason for having different values at each time interval - the newly-dried sand was significantly charged, and stuck to the glass walls and hopper pipe outlet, thus

affecting the granular flow.

### **3.3 Next Step**

The low amplitude of the detected sound was thought to be because the mass of avalanching sand was insufficient. Hence, flow in a similar, larger inclined-flow setup was studied next. A larger quantity of sound-producing sand was also obtained from Dumont Dunes, California, to supply the large chute's higher flow rate.

## CHAPTER 4

### LARGE-SCALE INCLINED CHUTE FLOW

With the small inclined flow setup, a low amplitude signal in the 100-150 Hz range was detected, which diminished over time and reappeared upon drying. It was hoped that a larger chute setup would increase the surface area of the avalanching layer and, consequently, achieve a louder amplitude of the signal. This would also provide an opportunity to reproduce Dagois-Bohy's and Douady's field and laboratory experiments ([9, 10]), which both involved a similar inclined chute.

Douady's field experiments utilised a chute 3m long, consisting of a pair of walls 45cm apart, set directly on the face of a dune, with a gate behind which sand was built up and then released. It was in this experiment that the threshold surface velocity of 0.23 m/s was found. Dagois-Bohy's laboratory setup was the main basis for our inclined chute, except that their gate was vertical and not normal to the chute as ours was. Upon releasing the gate, Dagois-Bohy et al were able to obtain sound in the 110-140 Hz range from their flows lasting around 2 seconds.

#### 4.1 Experimental Setup

Our larger experimental setup consisted of an open aluminium channel with cross-section 15 cm by 15 cm (375 grain diameters), and 1.2 m long. 30 cm of the chute was partitioned off by a gate, which could be pulled up normal to the chute to release the sand accumulated behind it. The closed end was then raised



Figure 4.1: The large inclined-flow setup

to form an inclined chute, the angle of which could be adjusted by changing the height of the raised end. A microphone was then positioned over the centre of the chute, somewhat closer to the gate than the open end, as it was thought that greater shearing would result in louder sound production.

Compared to our smaller setup, the current setup's smooth aluminium walls set at a greater distance apart meant that any frictional wall effects were reduced, and the region that could most closely approximate a natural avalanche (i.e. without walls) was significantly larger than in our small set-up. One drawback was that, due to the different volumes and length scales involved, the flowrate in the larger setup was not constant throughout the flow duration, as it approximately was in the smaller setup. The material sources - an overhead hopper and a build-up behind a gate - were also intrinsically different.

Fully removing the gate resulted in a huge rush of material initially, but also a very short flow duration, especially with the small volumes of Ottawa sand and Eureka dune sand available. The dimensions of the chute behind the gate also limited the maximum volume of material that could be used without

spillage, so a cardboard cylinder, normal to the base, was added to artificially 'extend' the reservoir, and simultaneously increase the pressure on the sand at the base. The larger force on the gate made it difficult to remove entirely with a single rapid movement, and there were also concerns that such a motion caused unwanted vibration in the chute walls. Hence, instead of being removed, the gate was only raised 5cm (125 diameters), which had the added advantage of having the sand at the base under pressure for a longer time. Flows using Ottawa sand or Eureka dune sand lasted approximately 20s, while those involving Dumont dune sand lasted around 40s.

After a visit from Vriend, a small barrier was added at the base of the chute to trap a thin layer of sand in the chute prior to flow, as it was thought that a rough base may not be sufficient for sound production, and that a layer of relatively stationary sand under the flow was necessary. However it was difficult to maintain a uniformly thick layer as the sand tended to flow down and pile up near the lower end of the chute.

## 4.2 'Burping' over Time

As was the case in the smaller inclined chute, sound recordings of flowing sand were taken at intervals after the sand was initially dried and its sound production over time was tracked.

As before, the resulting frequency spectrum ratios in figure 4.2 are each displaced downwards by a decade at each time interval for clarity and the spectra at the top of the figure is the result obtained immediately after drying. The ratios corresponding to Dumont dune sand and glass beads are superimposed to

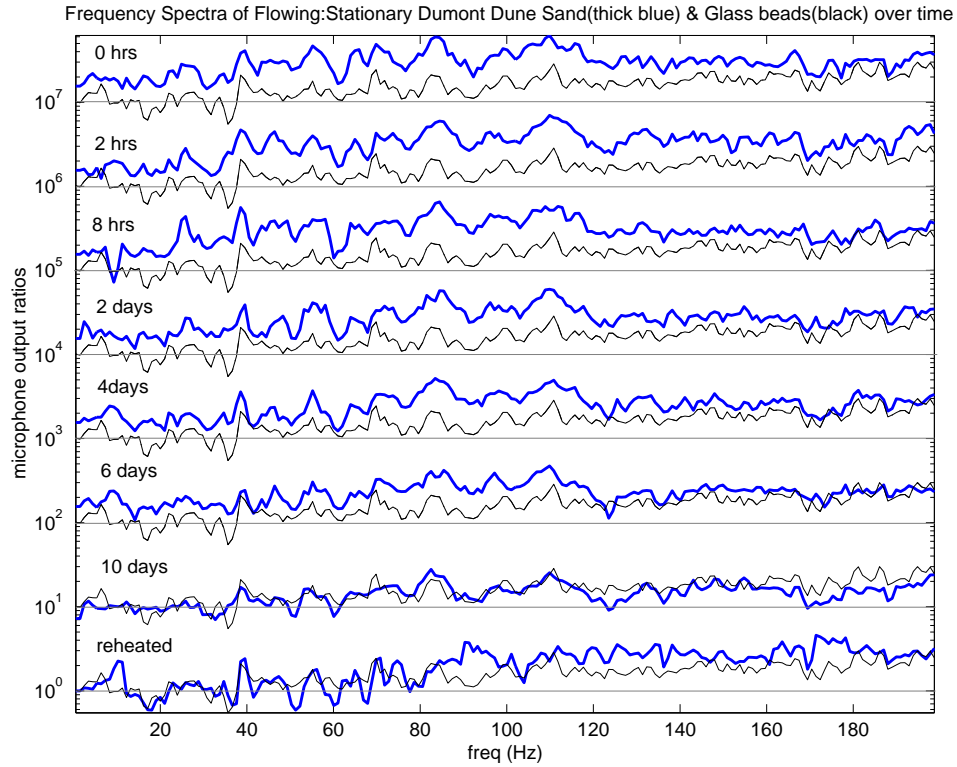


Figure 4.2: Frequency spectrum ratios of Dumont dune sand and glass beads over time

exhibit their differences after they were subjected to the same heating treatment.

Contrary to expectations, no audible sound was produced. In the frequency spectra, Dumont dune sand produced a broadband peak in the 40-140 Hz, which decreased over a duration of 10 days. However, upon drying again, it did not fully 'recover', except for a small region in the 80-100 Hz range. Even so, the difference in amplitude between the Dumont dune sand and glass beads was much smaller in the large chute than between Eureka dune sand and glass beads in the small chute. This was disappointing, as dried Dumont dune sand produced louder 'burps' when shaken in a jar than did Eureka dune sand. It was supposed that the threshold surface velocity had not been consistently exceeded in the large setup, as the varying depth and volumetric flow rate of the

flowing sand layer along the chute made it difficult to obtain a reasonable approximation of the surface velocity.

### **4.3 Conclusion**

While conducting the inclined flow experiments, it was noted that no audible sound was produced upon raising the gate. However audible low frequency sound was obtained if the chute was first filled with a layer of sand, then rotated from horizontal to inclined, resulting in an avalanche. It was not clear, however, whether the sound originated from the flow of the sand, or from compaction in the bucket placed below the chute to catch the outflow.

## CHAPTER 5

### ROTATING FLASK

The main motivation in using a rotating flask was to set up a continuous avalanche. With an appropriate volume of material and constant rotational speed, a layer of granular material would constantly avalanche down an inclined face, for as long as the flask was rotating. Neglecting the 'starting' and 'ending' edges of the avalanche, the rotating flask would provide a close facsimile of an avalanche. It was hoped that with the longer avalanche duration, loud sound would be produced.

#### 5.1 Motor-Rotated Flask

A 4-litre capacity glass flask with a circular neck had small 3mm glass beads glued to its inner walls to provide a rough surface. The flask was mounted horizontally on two pairs of wheels, the rotation of which was controlled by a motor.

The microphone was inserted a short distance into the open flask, just past the flask neck. No more than a little under half the flask was filled with material during experiments, such that the material would not spill out through the neck. Figure 5.1 shows the rotating flask setup with the maximum allowable volume of material, and the inclined profile of the avalanching material when the flask is rotating.

The rotation speed could be adjusted using a dial (labelled 1-10, corresponding speeds shown in table 5.1). At low speeds (below speed '2') the material



Figure 5.1: Rotating flask setup (max. sand volume)

Table 5.1: Angular velocities corresponding to speed dial

Dial No.	Rotational speed (rpm)
1	4
2	6
3	8
4	10
5	12
6	14
7	16
8	18
9	20
10	22

behaved like a rigid body, sliding at the base of the flask; at high speeds (above speed '8') the material moved so fast that very little time was spent traversing the avalanching face.

### 5.1.1 Setup Sound Contribution

Figure 5.2 shows spectrograms obtained from an initial experiment in which the rotational speed was first increased incrementally and then decreased. A prominent frequency peak just below 100 Hz is present in all three spectrograms, even the one corresponding to the empty flask. When Dumont dune sand was used this peak generally became more significant with increasing speed, except for the region corresponding to speeds '3'-'5'.

We were concerned that the setup itself was contributing significant noise because the frequency peak was present when the flask was 'empty'. Even without the flask, the motor generated noise, particularly when it was turned on or off as shown in figure 5.3. The flask's large volume and relatively small opening mean its resonant frequency could also be influencing the measured sound.

Figure 5.4 shows the frequency spectra obtained when air is blown across the mouth of the flask. There is a clear peak at 90 Hz, which is also present in figure 5.5 when the microphone is positioned inside the empty rotating flask rather than outside. This corresponds to the Helmholtz frequency (88.9 Hz, calculated using end-corrections from [7]) of the flask which was excited during rotation.

Figure 5.6 shows the frequency spectra of the empty rotating flask at speeds '2', '5' and '8'. The spectra are rather similar, but increase in amplitude with increasing speed. They all show a broadband peak in the 100-250 Hz region - where we expect 'burping' to occur - which means that any 'burping' produced would have to be significantly louder to be detected.

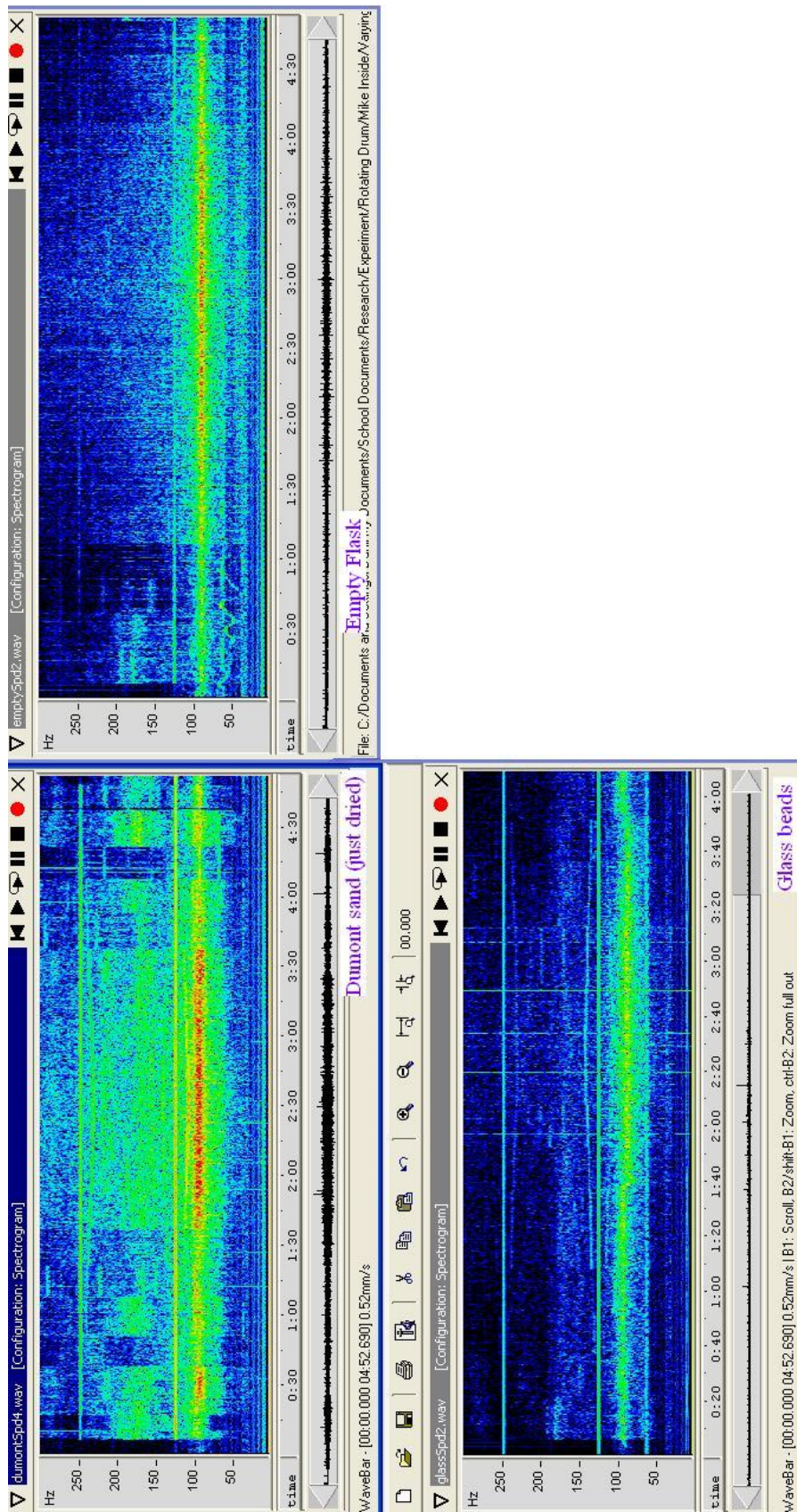


Figure 5.2: Frequency spectra of rotating flask containing different materials as rotation speed is increased and then decreased in steps every 15s. Counterclockwise from top right: empty flask, Dune sand, glass beads

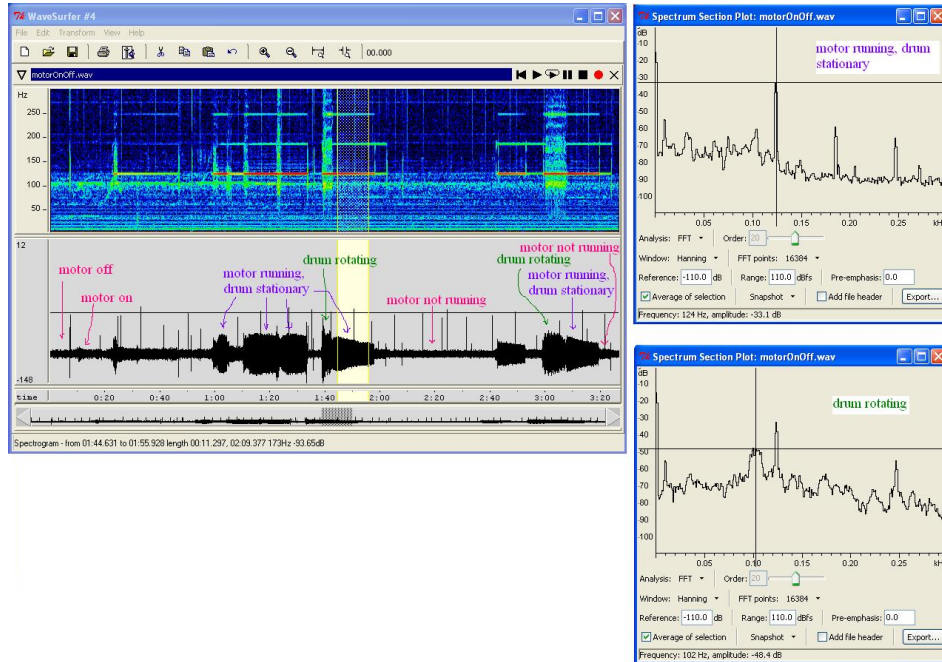


Figure 5.3: Spectrogram and time-trace of rotating flask when motor is turned on and off. Spectra on the right are: (top) when the motor is running but the flask is not included in the setup; (bottom) when the motor is on and the flask is rotating.

## 5.1.2 Results

In Figure 5.2, it appears that there are three distinct regions in the spectrogram of Dumont dune sand. From '0' to speed '2' the amplitude of the 90 Hz peak increased with speed, from speed '3' to '5' it was diminished (possibly due to the sand motion being in transition from rigid body to fluid behaviour) and between speeds '6' and '10' it reappeared and increased in amplitude with speed again. Hence it was decided to take sound recordings at speeds '2', '5' and '8' to cover all three regions.

Figure 5.7 shows the frequency spectrum ratios of Dumont dune sand, Ottawa sand and glass beads to that of the empty rotating flask at the 3 speed

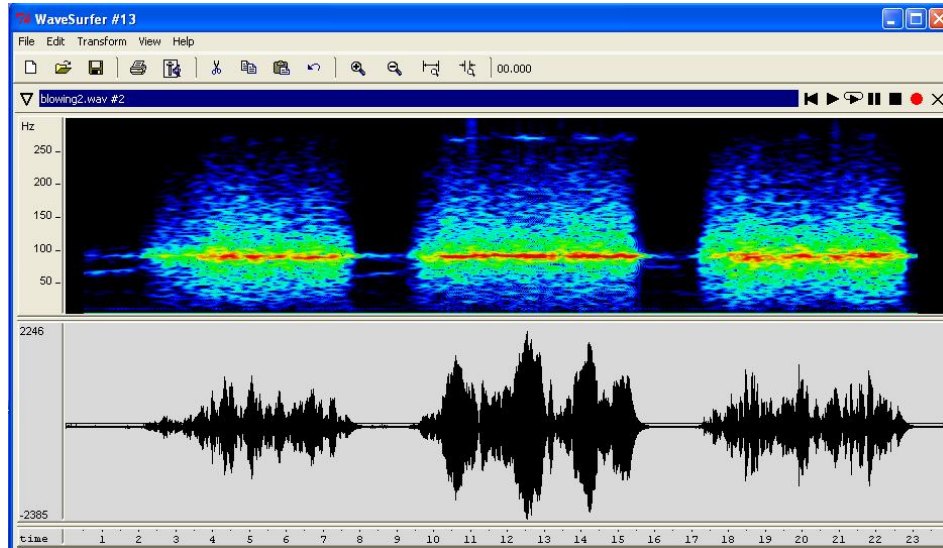


Figure 5.4: Frequency spectra when air is blown across flask mouth

settings. Dumont dune sand has a significant broadband peak in the 100-250 Hz region, compared to the other two materials. While it is encouraging that there is a difference between the ‘burping’ sand and ‘silent’ sand, it still requires further verification that it is indeed ‘burping’.

As with the inclined flow setups, a series of recordings at time intervals after drying the sand was taken to see if the broadband 100-250 Hz peak diminished over time. Figures 5.8, 5.9 and 5.10 show the time progression of Eureka dune sand at the three speed settings.

At speed ‘2’ there were no peaks that diminished over time and reappeared upon heating. This may have been due to not quite exceeding the threshold surface velocity; at this speed the surface velocity was estimated to be 0.23 m/s. At speed ‘5’ (estimated surface velocity 0.38 m/s) the region around 150 Hz appeared to diminish very slightly and reappear after drying. Finally at speed ‘8’ (estimated surface velocity 0.45 m/s), the 140 Hz spike as well as the frequen-

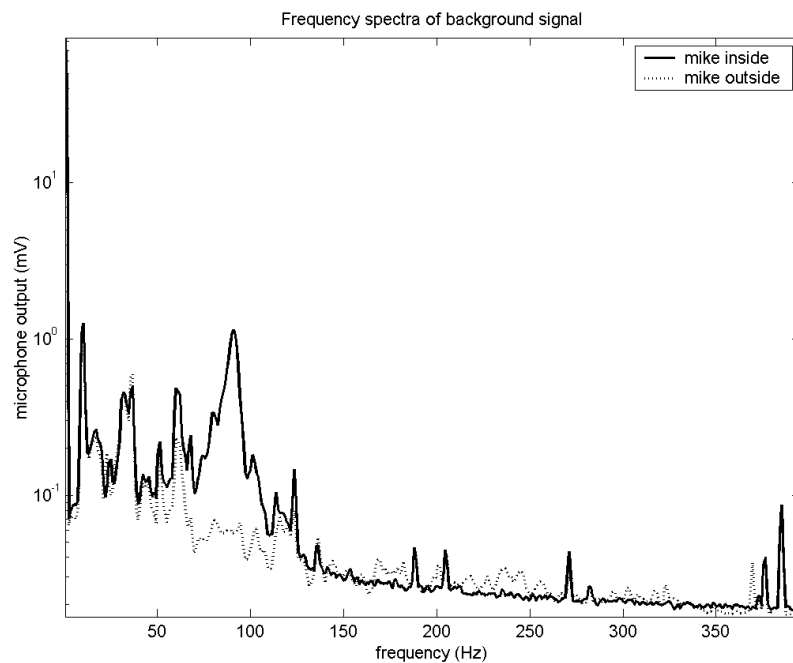


Figure 5.5: Frequency spectra when microphone is inside or outside rotating flask

cies from 150-180 Hz decreased in amplitude over time and reappeared with drying.

Overall during the experiments, some low frequency sound was heard which became louder with increasing speed. This sound however, was attributed to the flask's natural frequency being excited as it could be heard even when the flask was empty.

## 5.2 Drill-Rotated Flask

Lewis [18] reported producing a loud, continuous sound when rotating a jar of 4-inches diameter at 120-150 rpm, a speed much higher than our motor was

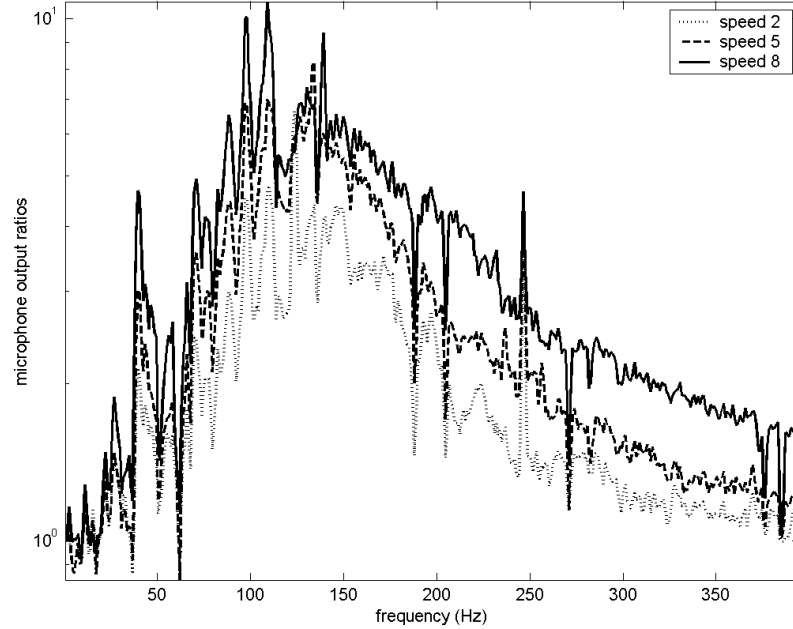


Figure 5.6: Frequency spectra of empty rotating flask, at different speeds

capable of. Hence a drill and flexible shaft was acquired to replace the motor so that the flask could be driven at higher speeds. Assuming that the necessary rotational speed scales inversely with the flask diameter, we estimated that 100 rpm would be appropriate for our 16cm-diameter flask.

Figure 5.11 shows one end of the flexible shaft clamped onto an aluminium chuck which drove the pulley-wheel system connecting to the flask, while the other end of the flexible shaft was connected to the drill. Upon adjusting the drill speed to an approximate speed range it was 'locked' so that the trigger need not be continuously depressed.

Using the drill eliminated the noise produced by the motor, but the drill itself produced high frequency noise. However this noise decreased greatly

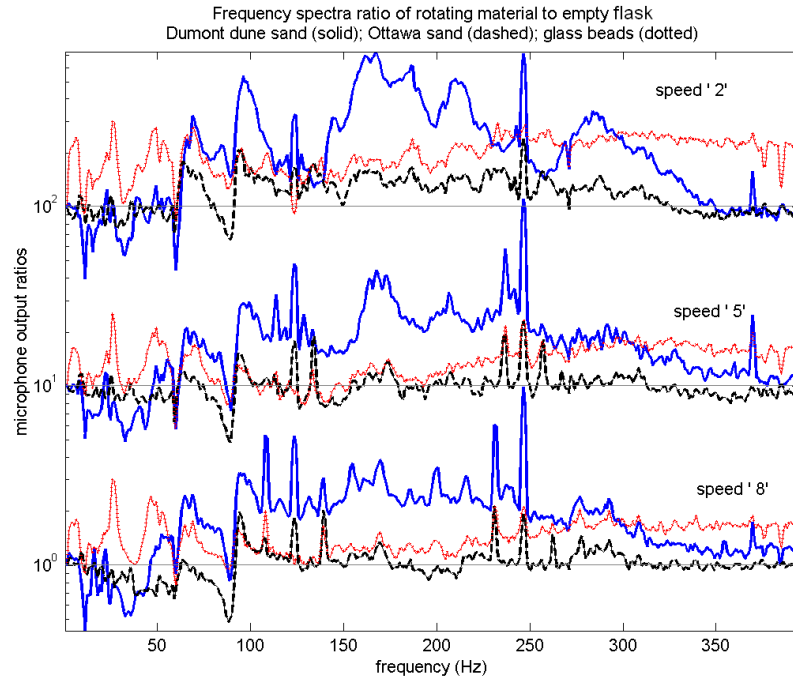


Figure 5.7: Frequency spectra of different materials in rotating flask, at different speeds

with distance, hence the use of the flexible shaft so that the drill could be placed some distance away from the flask. In addition the drill was shrouded with a thick sweater.

### 5.2.1 Results

Disappointingly no loud ‘burping’ sound was heard. However the frequency spectra of dried Dumont dune sand compared to that of humid Dumont dune sand showed a clear broadband peak at the tail-end of the flask’s Helmholtz resonance frequency, in the 100-150 Hz range. Figure 5.12 shows the frequency spectra of Dumont dune sand at various times after removal from the oven.

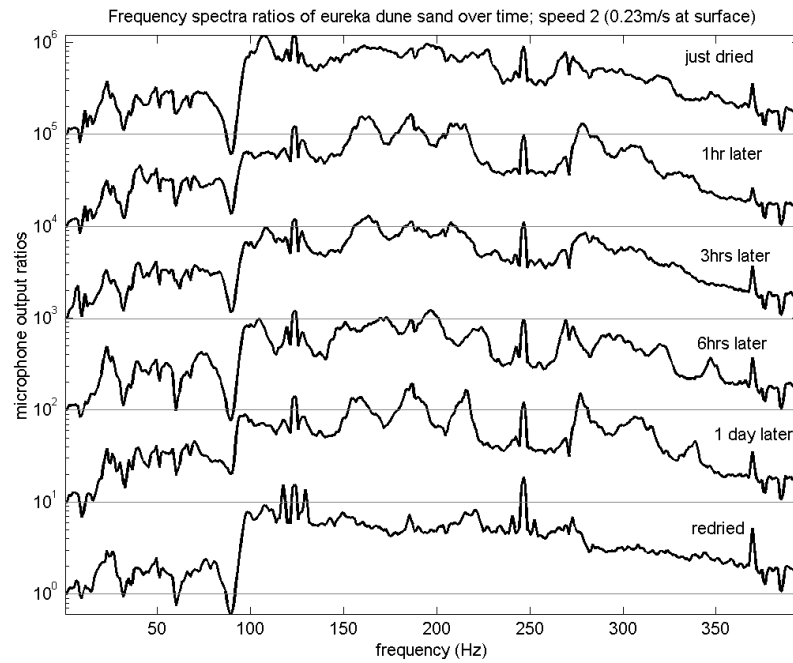


Figure 5.8: Eureka dune sand at speed '2' in rotating flask

For clarity, the 'power' (microphone output in mV squared) in the 105-150 Hz range at each time is plotted in figure 5.13. As time increases and the sand becomes more humid, the power decreases; upon re-drying the power returns to its initial magnitude. This indicates that this sound is likely to be 'burping'.

### 5.3 Conclusion

When the flask of Dumont dune sand was rotated at 100 rpm, an low amplitude peak that diminished over time and reappeared with drying, was produced. It was felt that perhaps the cycling motion of the sand meant that the avalanching layer was too thin, and the amount of avalanching surface truly approximating a natural avalanche was limited to only the centre of the motion and hence too

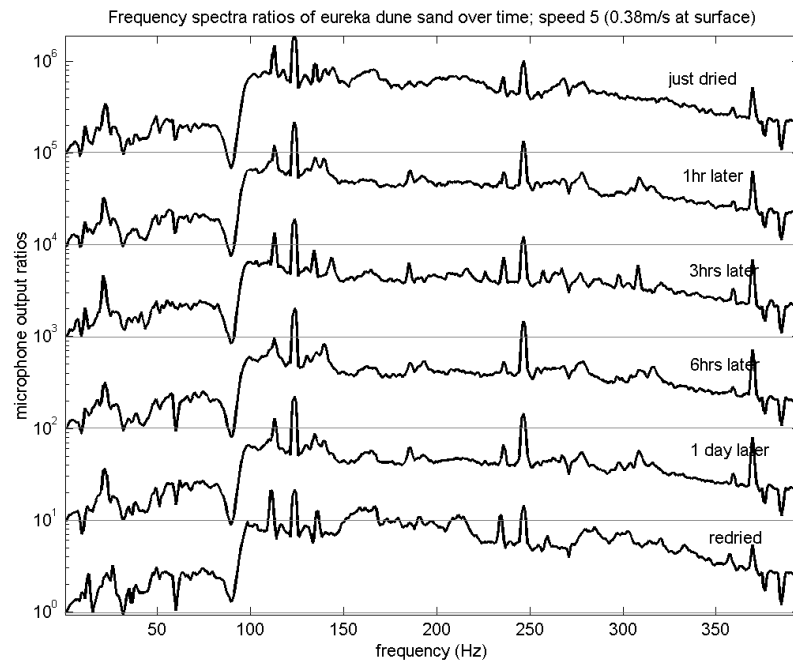


Figure 5.9: Eureka dune sand at speed '5' in rotating flask

small. As a result any 'burping' produced was too small in magnitude to be heard over the flask's Helmholtz frequency.

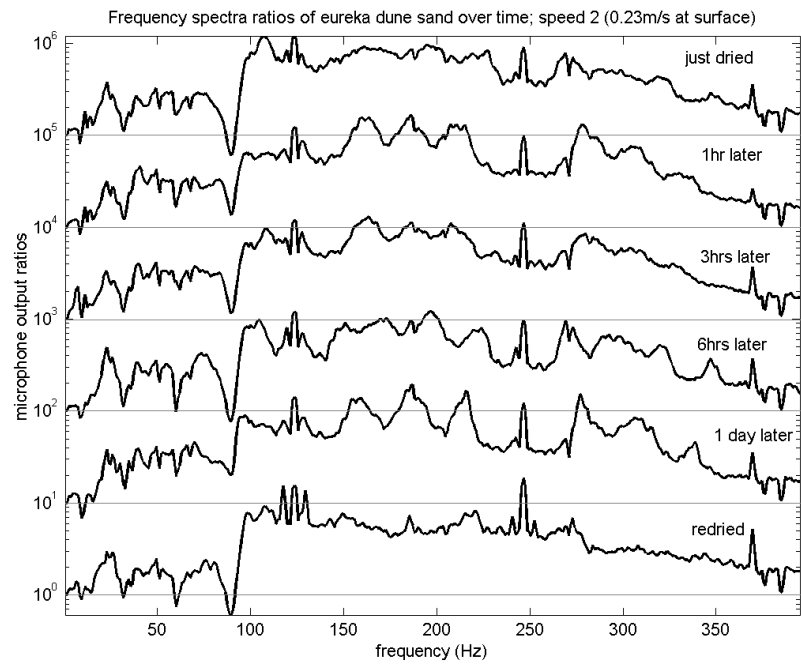


Figure 5.10: Eureka dune sand at speed '8' in rotating flask

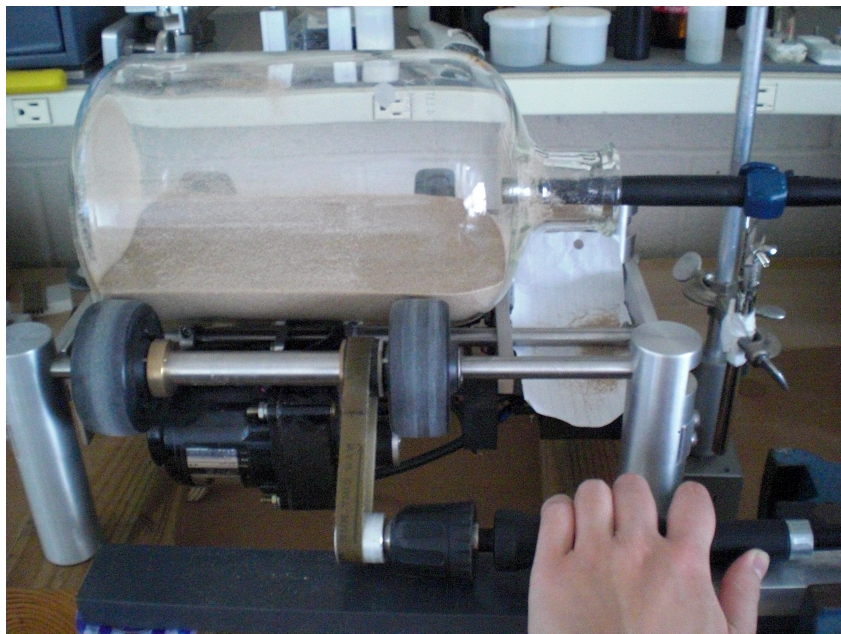


Figure 5.11: Drill-rotated flask setup

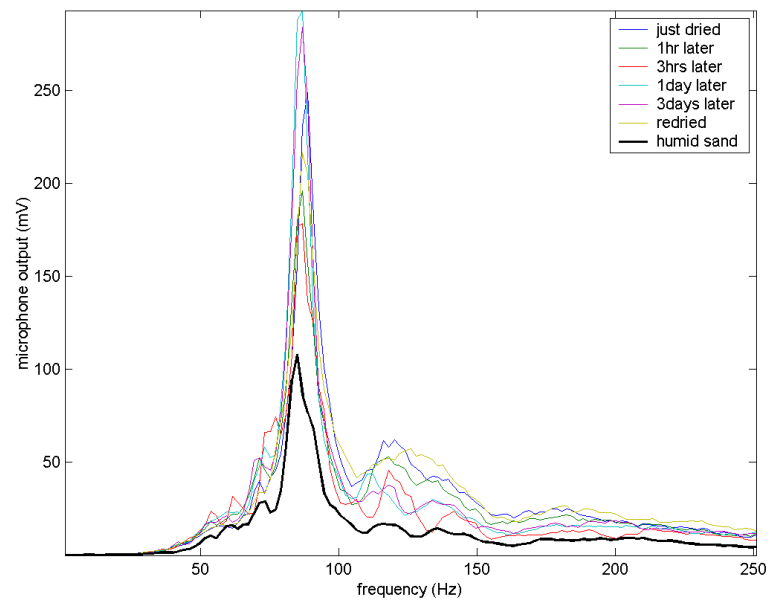


Figure 5.12: Frequency spectra over time of Dumont dune sand in flask rotating at  $\approx 100$ rpm

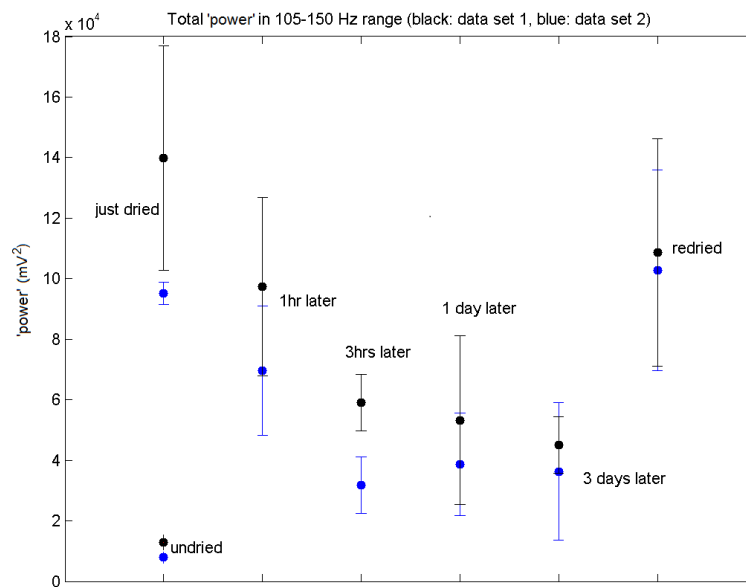


Figure 5.13: 'Power' in 105-150 Hz range over time of Dumont dune sand in flask rotating at  $\approx 100$ rpm, for 2 experiment runs

## CHAPTER 6

### PERTURBATION THEORY

This preliminary mathematical model (Figure 6.1) is based on Jenkins' extended kinetic theory for dense, slow granular flows [13]. If the flow is dense and slow, then it can be approximated by a steady, uniform density shear flow. From kinetic theory, the flow would have constant volume fraction  $v_0$  through its depth, and the granular temperature  $T_0$  would increase with depth. These terms, and the velocity profile  $u_0$  are dependent on the angle of inclination  $\phi$ . We then apply a small velocity perturbation  $v_1$  in the direction normal to the slope, and solve the continuity and momentum equations to determine if an oscillatory motion can be sustained by this flow.

The only material properties entering into this model are the material density  $\rho_s$  and the coefficient of restitution  $e$  through the granular temperature  $T$  and volume fraction  $v$ .

#### **6.1 Preliminary Model - Fully Dense Flow**

A two-dimensional analysis can be conducted if variations along the chute width are neglected. The sand motion is split into two parts - the fully-developed shear flow parallel to the slope and, superimposed on this, the hypothesised uniform oscillatory component, moving perpendicular to the slope. All variables involved in the model are then also split accordingly - the subscript 0 denoting those associated with the shear flow, which are constant or vary only with depth, and the subscript 1 denoting the oscillatory parts, which

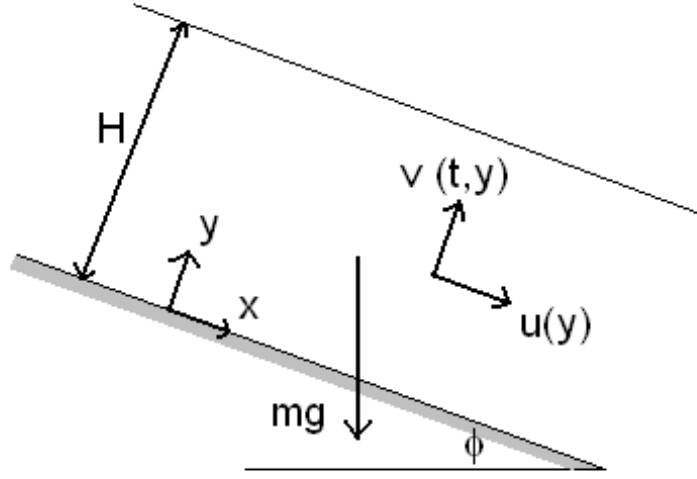


Figure 6.1: Schematic for fully-dense inclined shear flow perturbation model

are functions of both depth and time. The oscillatory parts are assumed to be small compared to those of the steady shear flow, so that products of terms with more than one subscript 1 can be considered negligible.

The velocities parallel to and normal to the flow are  $u_0(y)$  and  $v_1(t, y)$  respectively; the pressure  $p(t, y) = FT$ , where  $F(\rho) \equiv 4\rho G$ , with the mass density  $\rho(t, y) = \rho_s \nu$  of the flow given in terms of the material density  $\rho_s$  and the solid volume fraction  $\nu(t, y) = \nu_0 + \nu_1(t, y)$ ,  $G(\nu) = 0.63\nu / (0.60 - \nu) = G_0 + G_1(t, y)$  for dense flows [14], and  $T_0(y)$  is the strength of the velocity fluctuations (granular temperature).

From the kinetic theory of gases, the balance of fluctuation energy is

$$\frac{3}{2}\rho\dot{T} = \text{tr}(\mathbf{t}\nabla\mathbf{u}) - \nabla \cdot \mathbf{q} - \Gamma, \quad (6.1)$$

where  $T$  is the granular temperature,  $\mathbf{t}$  is the stress tensor,  $\mathbf{u}$  the velocity vector,  $\mathbf{q}$  the flux of fluctuation energy, and  $\Gamma$  the rate of energy dissipation due to

collisions of the granular material. Dense flows adjust themselves so the flux term is negligible; hence, for a steady homogeneous shear flow down an inclined slope, the left hand term and the flux term on the right are both zero and the stress term is reduced to  $S\dot{\gamma}$ , where  $\dot{\gamma}$  is the shear rate and the shear stress  $S \equiv \mu\dot{\gamma}$ , with  $\mu$  a function of the volume fraction  $\nu$ , particle diameter  $d$ , and  $T$ . The energy balance can then be written as

$$\frac{S^2}{\mu} = \Gamma. \quad (6.2)$$

Jenkins & Berzi [14] give the following expressions for  $\mu$  and  $\Gamma$ :

$$\mu = \frac{2Jpd}{5F\sqrt{\pi T}} \quad (6.3)$$

and

$$\Gamma = \frac{12}{\sqrt{\pi}} \frac{\rho G}{L} (1 - e_{eff}^2) T^{3/2}, \quad (6.4)$$

where  $F = (1 + e_{eff})/2$  for dense flows; the effective coefficient of restitution  $e_{eff}$  is defined in terms of  $e$  and  $\beta_0$ , the coefficient of tangential restitution in a sticking collision:

$$\frac{1 - e_{eff}^2}{4} \equiv \frac{1 - e^2}{4} + \frac{1 + \beta_0}{7} - \left(\frac{1 + \beta_0}{7}\right)^2 \left[1 + \frac{5(1 + \beta_0)}{14 - 5(1 + \beta_0)}\right], \quad (6.5)$$

where  $L$  is the length of a typical chain of particles in contact [13, 14] in a dense granular flow:

$$\frac{L}{d} = \frac{1}{2} \left[ \frac{15}{J} (1 - e_{eff}^2) \hat{c}^2 \right]^{1/3} G^{2/9}; \quad (6.6)$$

$\hat{c} = 0.50$  is a fitted parameter; and

$$J = \frac{1 + e_{eff}}{2} + \frac{\pi}{4} \left[ \frac{(3e_{eff} - 1)(1 + e_{eff})^2}{24 - (1 - e_{eff})(11 - e_{eff})} \right]. \quad (6.7)$$

Equation 6.2 determines the expressions for  $T$ ,  $\nu$  and  $\dot{\gamma}$ , which describe the steady state of the shear flow (subscript 0); all are dependent on the inclination

angle  $\phi$ . They are given by Jenkins and Berzi[14]:

$$T_0 = \left[ \frac{25\pi^{3/2} \hat{c}}{192 J^2} \right]^3 \frac{(1 + e_{eff})^5}{(1 - e_{eff})^3} \tan^9 \phi \frac{g \cos \phi (H - y)}{2}, \quad (6.8)$$

$$\nu_0 = 0.60 \left[ 1 + 0.63 \left( \frac{25\pi^{3/2} \hat{c} (1 + e_{eff})^2}{192 J^2 (1 - e_{eff})} \right)^3 \tan^9 \phi \right]^{-1}, \quad (6.9)$$

and

$$\dot{\gamma}_0 = \frac{5 \pi^{11/4}}{4 J^4 d} \left[ \left( \frac{25\hat{c}}{192} \right)^3 \frac{(1 + e_{eff})^7}{(1 - e_{eff})^3} \frac{(H - y)}{2} g \cos \phi \tan^{11} \phi \right]^{1/2}. \quad (6.10)$$

Integration of the shear rate then gives the velocity profile through the depth  $y$ :

$$u_0 = \frac{625 \pi^{11/4}}{9216 J^4 d} \left[ \frac{(1 + e_{eff})^7}{(1 - e_{eff})^3} \frac{(\hat{c}H)^3}{6} g \cos \phi \tan^{11} \phi \right]^{1/2} \left[ 1 - \left( 1 - \frac{y}{H} \right)^{3/2} \right], \quad (6.11)$$

where the velocity is assumed to be zero at depth  $H$  of the flow. Notably, in the steady state,  $T$  increases towards the base of the flow,  $\nu$  remains constant through depth, and the velocity profile  $u(y)$  is concave. This theory is only valid when the flow is dense enough for short chains of particles [13] to form, ie  $L/d \geq 1$ , which occurs only for:

$$\tan \phi \leq \sqrt{\frac{24 J}{5 \pi} \frac{(1 - e_{eff})}{(1 + e_{eff})}}. \quad (6.12)$$

For  $e_{eff} = 0.60$ , which corresponds to  $e = 0.92$  and  $\beta_0 = 0.25$ , this results in  $J \approx 0.88$  and a maximum inclination angle  $\phi_{max} = 30^\circ$ .

## 6.2 Equation Derivation

Using primes and overhead dots to denote differentiation with respect to  $y$  and  $t$  respectively, the equations of mass and flow momentum are:

$$\dot{\rho} + (\rho v)' = 0 \quad (6.13)$$

and

$$\rho (\dot{v} + vv') = t'_{yy} - \rho g \cos \phi. \quad (6.14)$$

Substituting  $\rho = \rho_s (v_0 + v_1)$  and  $t_{yy} = -p \approx -4\rho GT$ , and ignoring the small products, the equations then become:

$$\dot{v}_1 + v_0 v'_1 = 0 \quad (6.15)$$

and

$$\begin{aligned} v_0 \dot{v}_1 &= -4T'_0 (v_0 G_0 + v_0 G_1 + v_1 G_0) - 4v'_1 T_0 (v_0 \dot{G}_0 + G_0) \\ &\quad - (v_0 + v_1) g \cos \phi, \end{aligned} \quad (6.16)$$

where  $\dot{G}_0 \equiv \frac{dG}{dv}|_0$ . Further differentiating and elimination of  $v_1$  derivatives then results in the hyperbolic partial differential equation

$$\ddot{v}_1 = v''_1 (4v_0 \dot{G}_0 T_0 + 4G_0 T_0) + v'_1 \left[ (4v_0 \dot{G}_0 T'_0 + 4G_0 T'_0) + g \cos \phi \right]. \quad (6.17)$$

Replacing  $v_0 \dot{G}_0$  with  $0.60G_0 / (0.60 - v_0)$ , Equation 6.17 becomes

$$\ddot{v}_1 = v''_1 \left[ 4G_0 T_0 \left( \frac{1.20 - v_0}{0.60 - v_0} \right) \right] + v'_1 \left[ 4G_0 T'_0 \left( \frac{1.20 - v_0}{0.60 - v_0} \right) + g \cos \phi \right]. \quad (6.18)$$

Because the derivative of pressure with respect to  $y$  is  $-\rho_s v g \cos \phi$  and  $v_0$  is constant with depth in this dense shear flow,  $p \approx \rho g \cos \phi (H - y)$ . Thus, with the original definition of pressure, we obtain:

$$4(G_0 + G_1) T_0 = g \cos \phi (H - y) \quad (6.19)$$

and

$$4(G_0 T'_0 + G_1 T'_0 + \dot{G}_0 v'_1 T_0) = -g \cos \phi. \quad (6.20)$$

Using equations 6.19 and 6.20 with equation 6.18 gives a hyperbolic PDE that describes the variation of normal velocity with time and depth in terms of gravity, surface inclination angle, and flow thickness:

$$\ddot{v}_1 = v''_1 [Ag \cos \phi (H - y)] - v'_1 Bg \cos \phi, \quad (6.21)$$

where

$$A = \frac{1.20 - \nu_0}{0.60 - \nu_0} = 1 + \left[ 0.63 \left( \frac{25\pi^{3/2}}{192} \frac{\hat{c}}{J^2} \frac{(1 + e_{eff})^2}{1 - e_{eff}} \right)^3 \tan^9 \phi \right]^{-1} \quad (6.22)$$

and

$$B = \frac{0.60}{0.60 - \nu_0} = \left[ 0.63 \left( \frac{25\pi^{3/2}}{192} \frac{\hat{c}}{J^2} \frac{(1 + e_{eff})^2}{1 - e_{eff}} \right)^3 \tan^9 \phi \right]^{-1}. \quad (6.23)$$

This equation is made dimensionless using  $\tilde{t} = t \sqrt{g \cos \phi / H}$ ,  $\tilde{y} = y/H$ , and  $\tilde{v}_1 = v_1 / \sqrt{Hg \cos \phi}$ :

$$\ddot{\tilde{v}}_1 = \tilde{v}''_1 [A(1 - \tilde{y})] - B\tilde{v}'_1 \quad (6.24)$$

## 6.2.1 Approximate Solution

We can obtain an approximate solution by taking the depth-averaged value of the coefficient  $A(1 - \tilde{y})$ , i.e. assuming uniform properties:

$$\ddot{\tilde{v}}_1 = \frac{A}{2} \tilde{v}''_1 - B\tilde{v}'_1. \quad (6.25)$$

A solution is then obtained using separation of variables:

$$\tilde{v}_1(\tilde{t}, \tilde{y}) = \tilde{y} \exp\left(\frac{B}{A}\tilde{y}\right) \left[ c_1 \sin\left(\frac{B}{\sqrt{2A}}\tilde{t}\right) + c_2 \cos\left(\frac{B}{\sqrt{2A}}\tilde{t}\right) \right], \quad (6.26)$$

which can be easily verified by direct substitution into Equation 6.25. Converting the time portion back to a dimensional form, we find an expression for the approximate frequency  $f$ :

$$\begin{aligned} f_{dense,/,approx} &= \frac{1}{2\pi} \left( \frac{B}{\sqrt{2A}} \right) \left( \frac{1}{\sqrt{H/g \cos \phi}} \right) \\ &= \frac{B}{2\pi} \sqrt{\frac{g \cos \phi}{2HA}}. \end{aligned} \quad (6.27)$$

For an inclination angle  $\phi = 20^\circ$ , grain diameter  $d = 0.4\text{mm}$ , gravitational constant  $g = 9.8\text{ms}^{-2}$ , coefficient of restitution  $e_{eff} = 0.60$ , and a flow depth  $H = 25d$ , we obtain a frequency  $f_{dense,approx} = 78 \text{ Hz}$ .

## 6.2.2 Matlab Solution Comparison

For us to solve our original non-dimensional PDE Equation 6.24 in Matlab using its hyperbolic PDE solver, the equation has to be written in the form  $\ddot{\tilde{v}}_1 = [F(\tilde{y}, \tilde{t}) \tilde{v}_1']'$ . Hence we use the same assumption as before, that the volume fraction  $\nu_0$  is very near 0.60 due to the slow and dense flow, so that we can use equation 6.24.

Matlab's PDE toolbox solves Equation 6.29 at every point in a user-defined mesh, exporting these solutions at each time-step. An FFT of the solution for different values of  $\tilde{y}$  determines the non-dimensional frequency  $f_{nondim}$  of the solution. Using the non-dimensional scaling, the frequency in dimensional time is then found to be:

$$f_{dense,matlab} = f_{nondim} \sqrt{\frac{g \cos \phi}{H}}. \quad (6.28)$$

It was found that  $f_{nondim}$  was not constant for all  $0 < \tilde{y} \leq 1$ . In fact, for an

inclination angle  $\phi = 20^\circ$  and coefficient of restitution  $e_e f f = 0.60$ ,  $f_{nondim} = 4.38$  for the top half of the flow and 10 for the bottom half. So with grain diameter  $d = 0.4\text{mm}$ , gravitational constant  $g = 9.8\text{ms}^{-2}$ , and a flow depth  $H = 25d$ , this results in  $f_{dense,matlab} = 133\text{ Hz}$  in the top half of the flow and 304 Hz in the bottom half.

### 6.2.3 Exact Solution

For a slow, dense granular flow we know that the volume fraction  $\nu_0$  is very near 0.60, so  $A \approx B$ , and hence:

$$\ddot{v}_1 = [\tilde{v}_1' A (1 - \tilde{y})]' . \quad (6.29)$$

This equation has the same form as that which governs the transverse oscillations of a hanging chain [5, 30].

A solution is again obtained via separation of variables:

$$\tilde{v}_1(\tilde{t}, \tilde{y}) = J_0 \left( 2\lambda \sqrt{\frac{1 - \tilde{y}}{A}} \right) [c_1 \sin(\lambda \tilde{t}) + c_2 \cos(\lambda \tilde{t})] , \quad (6.30)$$

where  $2\lambda/\sqrt{A}$  are the zeroes of the zeroth-order Bessel function of the first kind. The boundary conditions employed are that normal velocity is zero at the base of the flow and finite at the surface. Equation 6.30 can be easily verified by direct substitution into equation 6.29. Converting the time portion back to a dimensional form, we find an expression for the lowest frequency  $f$  (corresponding to the first zero of the Bessel function):

$$\begin{aligned} f_{dense\ exact} &= \frac{\lambda}{2\pi} \left( \frac{1}{\sqrt{H/g \cos \phi}} \right) \\ &= \frac{0.6012}{\pi} \sqrt{\frac{Ag \cos \phi}{H}} . \end{aligned} \quad (6.31)$$

For an inclination angle  $\phi = 20^\circ$ , grain diameter  $d = 0.4\text{mm}$ , gravitational constant  $g = 9.8\text{ms}^{-2}$ , coefficient of restitution  $e_{eff} = 0.60$ , and a flow depth  $H = 25d$ , the two lowest frequencies for  $f_{dense,exact}$  are 133 and 305 Hz. Comparing these to the frequencies obtained using Matlab, we see that the bottom half of the flow excited a higher mode while the top half excited the lowest mode of oscillation.

#### 6.2.4 Comparing Exact Solution to Experiment

In the small inclined chute flow experiment, a low amplitude sound in the 90-145 Hz range was detected. The predicted frequency of 133 Hz from theory falls in this range, however this was using an inclination angle of  $\phi = 20^\circ$ . The actual inclination measured during the experiment exceeds  $\phi_{max} = 30^\circ$  for this theory to be valid. Hence the model has to be modified to accommodate the larger inclination angle sustained by the sidewalls of the narrow chute [22].

In the rotating flask experiment, the sidewalls are far away enough that the effect of the sidewalls would be negligible in the centre of the flask. Unfortunately the ‘depth’ of the part of the flow approximating an avalanche in the center of the flask is not visible, and thus cannot be measured.

### 6.3 Second Model - Dense and Dilute Layers

In order to match the theory to experimental results, we now consider the presence of frictional sidewalls, which enables us to predict the depth of the dense shear flow for a given cell-width  $W$  and sidewall frictional coefficient  $\mu_w$ . The

presence of sidewalls does not change the expressions used previously, except to provide an expression for  $H$  [14]:

$$0 = \alpha - \tan \phi + \mu_w \frac{H}{W}, \quad (6.32)$$

where  $\alpha$  is the ratio of shear to pressure at the base of the flow, assumed to be at yield.

It must be noted that the expressions used by Berzi & Jenkins [6, 14] were based on a work that is most appropriate for a dense regime, and hence would not model the dilute layer exactly.

In our experimental setup the inclination during flow of ‘burping’ sand was found to be between  $40^\circ$  and  $48^\circ$ , which exceeds the maximum inclination angle given by equation 6.12 ( $30^\circ$ , for  $e_{eff} = 0.60$ ). Hence, there must be a dilute layer of thickness of  $h - H$  above the dense layer [6] as shown in figure 6.2, which provides a finite pressure boundary condition at the top of the dense flow.

Here we are interested in the effect of the dilute layer on the dense layer, which is still sustaining the breathing motion as in the first model.

An expression for the pressure at the dense-dilute interface is obtained by assuming that the volume fraction varies linearly through the dilute layer, with  $\nu_H$  the volume fraction in the dense layer:

$$p(t, y) = 4\rho g T \approx p_H + \rho g \cos \phi (H - y), \quad (6.33)$$

where the pressure exerted on the dense layer by the dilute layer is

$$p_H = \frac{1}{2} \rho_s g \nu_H (h - H) \cos \phi. \quad (6.34)$$

Momentum balances normal and tangential to the flow lead to a relationship between shear stress and pressure that is dependent on the angle of inclination,

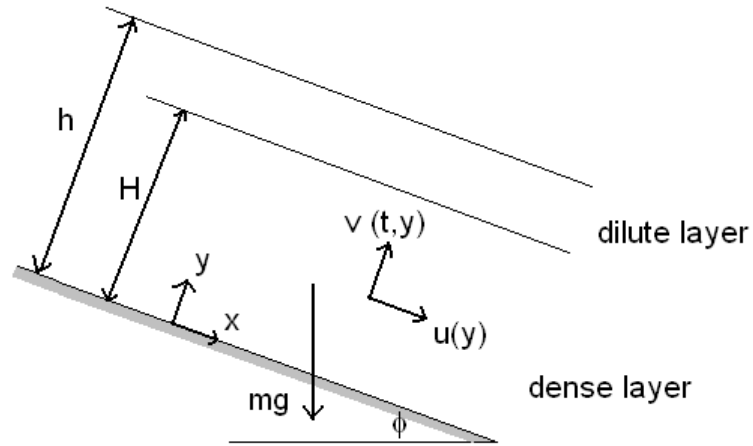


Figure 6.2: Schematic of inclined shear flow with both dilute and dense layers

sidewall friction coefficient, and volume fraction. Considering the limiting angle of inclination above which a dilute layer is present, and the pressure at the interface of the dilute and dense layers, Berzi and Jenkins [6] determine an expression for the thickness of the dilute and dense layers:

$$h - H = 2 \frac{\tan \phi - k}{\mu_w} W \quad (6.35)$$

and

$$H = \frac{k - \alpha}{\mu_w} W, \quad (6.36)$$

where  $k$  is tangent of the maximum angle at which the dilute layer is not present, determined by equation 6.12. As mentioned previously, this is found by setting the length of clusters at the top of the dense layer to be one particle diameter.

The volume fraction in the dense layer  $\nu_H$  is found by substituting  $\tan \phi$  in equation 6.9 with the average stress ratio  $\bar{s}/p$  given by Berzi and Jenkins [6]:

$$\frac{\bar{s}}{p} = k - \frac{\mu_w H}{2 W} \quad (6.37)$$

Using the same procedure as in the previous simpler model, equations 6.19, 6.21 and 6.24 then become

$$4(G_0 + G_1)T_0 = g \cos \phi \left( \frac{1}{2}h + \frac{1}{2}H - y \right), \quad (6.38)$$

$$\ddot{v}_1 = v_1'' \left[ Ag \cos \phi \left( \frac{1}{2}h + \frac{1}{2}H - y \right) \right] + v_1' (-Bg \cos \phi), \quad (6.39)$$

and

$$\ddot{\tilde{v}}_1 = \tilde{v}_1'' \left[ A \left( \frac{h}{2H} + \frac{1}{2} - \tilde{y} \right) \right] - B\tilde{v}_1', \quad (6.40)$$

where substitution of  $h = H$  recovers the previous equations. Once again, the assumption that volume fraction is very near 0.60, leads to  $A \approx B$ . While the temporal component of the solution to the PDE is unaffected, the spatial component is modified:

$$Y(\tilde{y}) = \left[ b_3 J_0 \left( 2\lambda \sqrt{\frac{h/(2H) + 1/2 - \tilde{y}}{A}} \right) + Y_0 \left( 2\lambda \sqrt{\frac{h/(2H) + 1/2 - \tilde{y}}{A}} \right) \right]. \quad (6.41)$$

If we consider our normal velocity  $v_1$  to be similar to the deflection of a hanging chain, then equation 6.40 has two different analogies to a hanging chain that lead to two different solutions. One is a hanging chain with uniform density, the end of which is connected to another chain of with density varying linearly to zero. The second analogy, is of a hanging chain with a point mass at the end. Both of these result in non-zero tension at the end of the original chain.

### 6.3.1 Two Hanging Chains

As mentioned earlier, the volume fraction of the dilute layer is assumed to vary linearly through its depth, so the average volume fraction would be half that of the dense layer. We can then transform this into a layer of half the height of

the dilute layer, but now with the same average volume fraction of the dense layer. Hence  $(H + h)/2$  replaces  $H$  in equation 6.37, and we can take the normal velocity to be zero at the base of the flow ( $\tilde{y} = 0$ ) and finite at the new total depth ( $\tilde{y} = h/2H + 1/2$ ). The solution is

$$\tilde{v}_1(\tilde{t}, \tilde{y}) = J_0 \left( 2\lambda \sqrt{\frac{h/(2H) + 1/2 - \tilde{y}}{A}} \right) [c_1 \sin(\lambda\tilde{t}) + c_2 \cos(\lambda\tilde{t})], \quad (6.42)$$

where  $2\lambda \sqrt{(h/2H + 1/2)/A}$  are the zeroes of the zeroth-order Bessel function of the first kind. Upon converting the time portion back to a dimensional form as before, we find an expression for the lowest frequency  $f$  (corresponding to the first zero of the Bessel function):

$$\begin{aligned} f_{2chains} &= \frac{\lambda}{2\pi} \left( \frac{1}{\sqrt{H/g \cos \phi}} \right) \\ &= \frac{2.4048}{2\pi} \sqrt{\frac{AH}{2(h+H)}} \sqrt{\frac{g \cos \phi}{H}} \\ &= \frac{1.2024}{\pi} \sqrt{\frac{Ag \cos \phi}{2(h+H)}}. \end{aligned}$$

Because  $h > H$ , the frequency obtained by this model is higher than that of the fully-dense layer by a factor of  $\sqrt{2h/(h+H)}$ , for the same total flow depth.

### 6.3.2 Hanging Chain with Point Mass

Separation of variables in equation 6.40 results in a spatial component of the form

$$b_3 J_0 \left( 2\lambda \sqrt{\frac{h/(2H) + 1/2 - \tilde{y}}{A}} \right) + b_4 Y_0 \left( 2\lambda \sqrt{\frac{h/(2H) + 1/2 - \tilde{y}}{A}} \right). \quad (6.43)$$

Zero normal velocity at the base of the flow results in

$$b_3 J_0 \left( 2\lambda \sqrt{\frac{h/(2H) + 1/2}{A}} \right) + b_4 Y_0 \left( 2\lambda \sqrt{\frac{h/(2H) + 1/2}{A}} \right) = 0. \quad (6.44)$$

Requiring that the velocity at the top of the dense layer be finite is not sufficient to eliminate the second coefficient, instead having normal derivative of the velocity be zero is used as a boundary condition. In terms of the hanging chain, this is equivalent to having the chain be vertical at the end with the point mass. This results in the expression

$$b_3 J_1 \left( 2\lambda \sqrt{\frac{h/(2H) - 1/2}{A}} \right) + b_4 Y_1 \left( 2\lambda \sqrt{\frac{h/(2H) - 1/2}{A}} \right) = 0. \quad (6.45)$$

For ease of notation we define

$$a_0 \equiv 2\lambda \sqrt{\frac{h/(2H) + 1/2}{A}}$$

and

$$a_1 \equiv 2\lambda \sqrt{\frac{h/(2H) - 1/2}{A}} = a_0 \sqrt{\frac{h - H}{h + H}}.$$

The expressions arising from the boundary conditions then become

$$b_3 J_0(a_0) + b_4 Y_0(a_0) = 0 \quad (6.46)$$

and

$$b_3 J_1(a_1) + b_4 Y_1(a_1) = 0. \quad (6.47)$$

Upon solving equations 6.46 and 6.47 we obtain an expression that must be satisfied for a non-trivial solution:

$$J_1(a_1) Y_0(a_0) - J_0(a_0) Y_1(a_1) = 0. \quad (6.48)$$

Given values of  $h$  and  $H$ ,  $a_1$  can then be expressed as a multiple of  $a_0$ , and the roots of equation 6.48 can then be found numerically. Table 6.1 shows the four lowest values of  $a_0$  corresponding to some ratios of  $h/H$ . The non-dimensional frequency  $\lambda$  is then determined by inverting the definition of  $a_0$ , resulting in:

$$f_{ChainMass} = \frac{a_0}{2\pi} \sqrt{\frac{Ag \cos \phi}{2(h + H)}}. \quad (6.49)$$

Table 6.1: Lowest  $a_0$  values for flow with dense and dilute layers, using hanging chain with point mass analogy.

$h/H$	Lowest roots of equation 6.48			
1.5	3.31	8.72	14.33	19.98
2	4.14	11.31	18.68	26.09
2.5	4.94	13.79	22.83	31.90
3	5.74	16.23	26.90	37.60
3.5	6.54	18.64	30.92	43.24
4	7.33	21.03	34.92	48.84
4.5	8.12	23.42	38.90	54.41

If the  $h/H$  ratio were such that  $a_0$  were approximately equal the zeros of the Bessel function, then  $f_{ChainMass}$  would be approximately equal to  $f_{2chains}$  and, thus, also greater than the predicted frequency for fully-dense flow  $f_{dense\ exact}$  by a factor of  $\sqrt{2h/(h+H)}$  for the same total depth.

Of the two analogies, that corresponding to the point mass at the end of the hanging chain is the more appropriate, as the true variation of density in the dilute layer is unknown. Thus even though the non-zero pressure boundary condition is satisfied in both analogies, the two-chain analogy may not represent the actual system closely enough. Physically, the behaviour of both systems is also different at the end of the original chain, despite both having the same magnitude of tension there.

Table 6.2: Expressions for frequency;  $A = \frac{1.20-\nu_0}{0.60-\nu_0}$ ,  $J_0^*$  are roots of  $J_0(x)$ ,  $a_0$  determined numerically based on  $h$  and  $H$  values.

Model	Frequency
Two chains	$f_{2chains} = \frac{J_0^*}{2\pi} \sqrt{\frac{Ag \cos \phi}{2(h+H)}}$
Chain and point mass	$f_{ChainMass} = \frac{a_0}{2\pi} \sqrt{\frac{Ag \cos \phi}{2(h+H)}}$

Table 6.3: Lower mode frequencies for  $d = 0.4\text{mm}$ , fitted parameter  $\hat{c} = 0.50$ ,  $e_{eff} = 0.05$ ,  $\phi = 42^\circ$ ,  $\mu_w = 0.30$ ,  $\alpha = 0.70$ , and width =  $25d$ .  $h = 25.0d$  and  $H = 8.88d$  are determined numerically. These parameters give  $\nu_H=0.506$ ,  $A=7.38$  and  $\nu_H=0.448$ ,  $A=4.95$  for the two-chains and chain-and-point-mass models respectively.

Model	Frequencies/Hz			
Two chains	17.0	39.1	61.3	85.6
Chain and point mass	31.6	88.9	147.3	205.9

### 6.3.3 Comparing Theory to Experiment

For ease of comparison, Table 6.2 shows expressions for the frequency from the solutions considered in this section. The frequencies of the first few modes are then given in Table 6.3.

Comparing the frequencies in Table 6.3 with the broadband peak of 90-145 Hz detected during the small inclined-chute flow experiments, it is clear that all the frequencies calculated by the two-chain model are lower; only the higher modes (4th and above) would possibly be within range, but we do not believe the system to be exciting such high modes. Whereas with the chain-and-point-mass model, the second and third modes would be within range.

These low fundamental frequencies may be because, at a total flow depth  $h$  and inclination  $\phi$  matching the measured values in the small inclined chute, the required values of  $e_{eff} = 0.05$ ,  $\mu_w = 0.30$  and  $\alpha = 0.70$  resulted in a low value of  $v_0$  and hence low  $A$ . The flow is then not as dense as initially assumed.

These predicted frequencies are much lower than that measured in the experiments. This may be because the kinetic theory was based on spherical particles, and the low effective coefficient of restitution employed was not sufficient to account for energy dissipation of the aspherical sand particles, resulting in an underestimation of the height of the dense layer. It is also likely that the average stress ratio in the dense layer was overestimated, because the volume fractions obtained are a little low for the flow to be considered dense. A lower stress ratio of 0.500, for the two-chain model, would result in a volume fraction of 0.595 and predicted frequency of 69 Hz. This highlights the sensitivity of the calculation to the value of the volume fraction. This sensitivity could be explored in numerical simulations similar to those carried out by Silbert, et al. [34], Silbert [33], and Richard, et al. [29].

CHAPTER 7  
SHEARING WITH A STYLUS

Aside from shaking in a jar, another test for sufficient 'dryness' of sand was to stroke through it lightly with a stylus. As such, it was thought that the sound produced during stroking must also be that of 'burping', and the mechanism by which such sound is produced must also be similar to that by which it is produced by shaking in a glass jar or in artificial avalanches.

A stylus was stroked over the surface of the sand, with varying force applied (Figure 7.1). If the 'burping' sand was sufficiently dry, a loud sound was produced, depending on the force applied and the speed of the stroke. It was possible to produce sound with the stylus being pulled through the material like a plough, but was far easier if the angle between the stylus and stroking direction were acute.

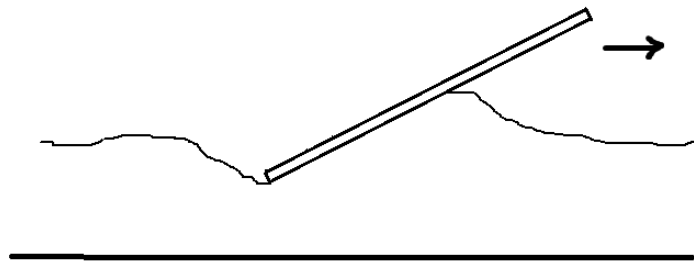


Figure 7.1: Stroking stylus through sand

Glass beads and Ottawa sand produced absolutely no 'burping' at all, while both Eureka dune sand and Dumont dune sand 'burped' readily (Figure 7.2).

Due to the large volume of Dumont dune sand available, it was used for all the stroking experiments.

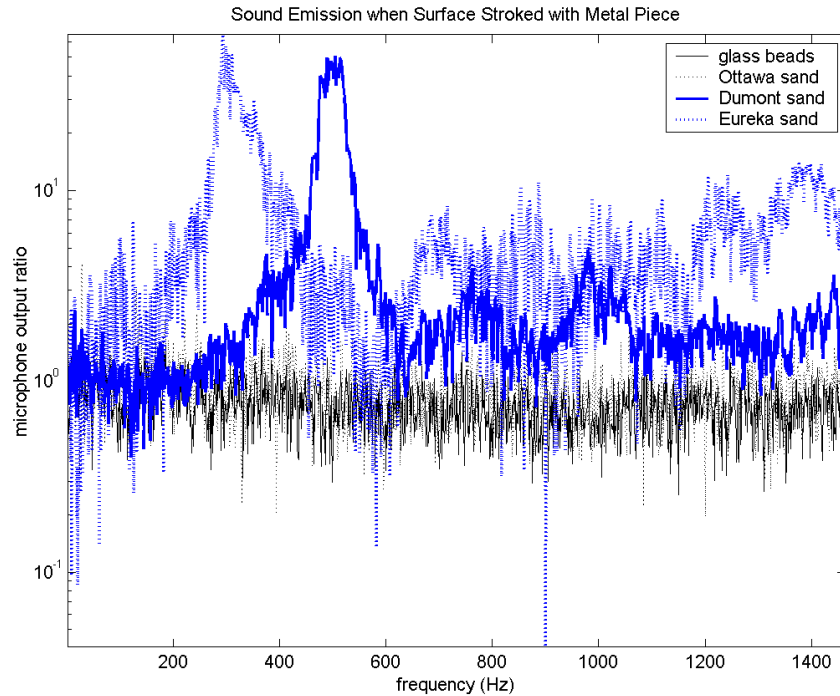


Figure 7.2: Frequency spectra ratios from stroking different styluses in baking tray

## 7.1 Experimental Setup 1 - Baking Tray

Stroking was first performed in trays, removed from the oven in which the sand samples were dried. The trays were regular baking trays, approximately 9 by 13 by 1.5 inches. Figure 7.3 shows such a tray of Dumont dune sand.

The frequency spectra ratios of sound produced during stroking to background noise was tracked over time, as shown in figure 7.4. The broadband



Figure 7.3: Baking tray for stroking experiment

peak from 400-550 Hz diminished visibly over a day and increased after re-drying the sand. Although the sound is of a higher frequency than the ‘burping’ obtained by Vriend [37] or Douady et al [10], it is very likely related because it involves shearing of a mass of sand above a stationary pile. Hence we refer to it as ‘burping’.

Figure 7.5 shows the frequency produced by stroking when the depth of sand in the tray is changed. ‘Depth’ here referring to the depth of the sand bed prior to stroking, as during stroking the stylus will penetrate the bed, leaving furrows behind. The frequency of the sound remains in the 500-550 Hz range, but its amplitude decreases with the depth of the bed.

## 7.2 Experimental Setup 2 - Large Chute

Because of the size of the baking trays, it was not possible to employ long strokes or to vary the depth of the sand bed very much. Hence the large chute was set

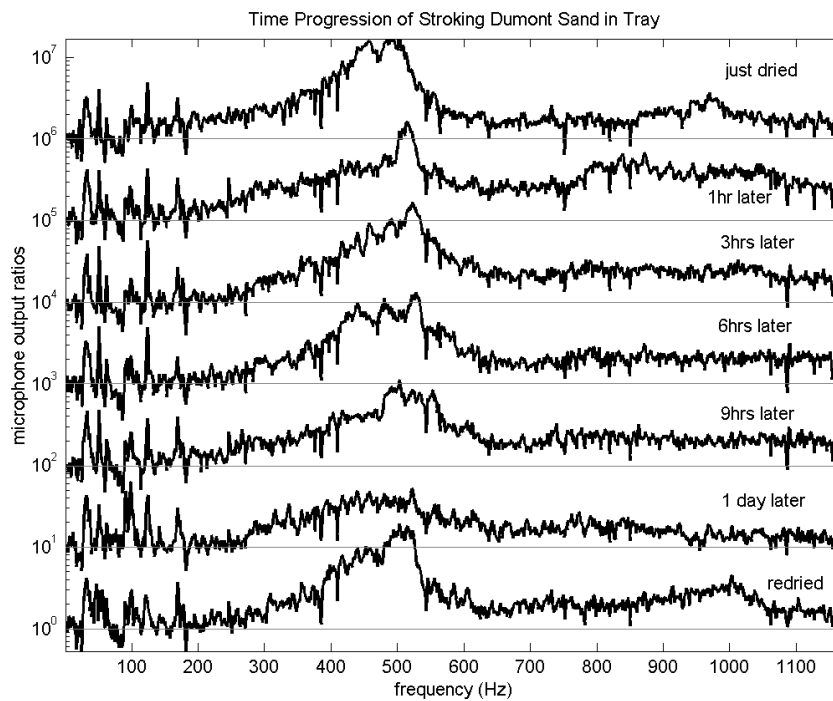


Figure 7.4: Time progression of stroking frequency spectra in baking tray

horizontally, to act as a longer, deeper ‘tray’ for stroking (Figure 7.6).

A small variety of styluses were also obtained for stroking - an aluminium stylus of 2.5cm width, a standard foot-long wooden rule, two wooden boards of 10cm and 13.5cm widths respectively, and a solid aluminium rod of diameter 2.5cm.

At this point we theorised that the ‘burping’ was due to compaction and shearing of some sort; hence, due to the presence of sidewalls, the behaviour of the sand in the centre of the chute and at the sides would be different, possibly leading to a different frequency. In Figure 7.7 the peak frequency obtained during stroking is plotted as a function of position across the width of the chute. As expected the frequency is lower near the chute walls.

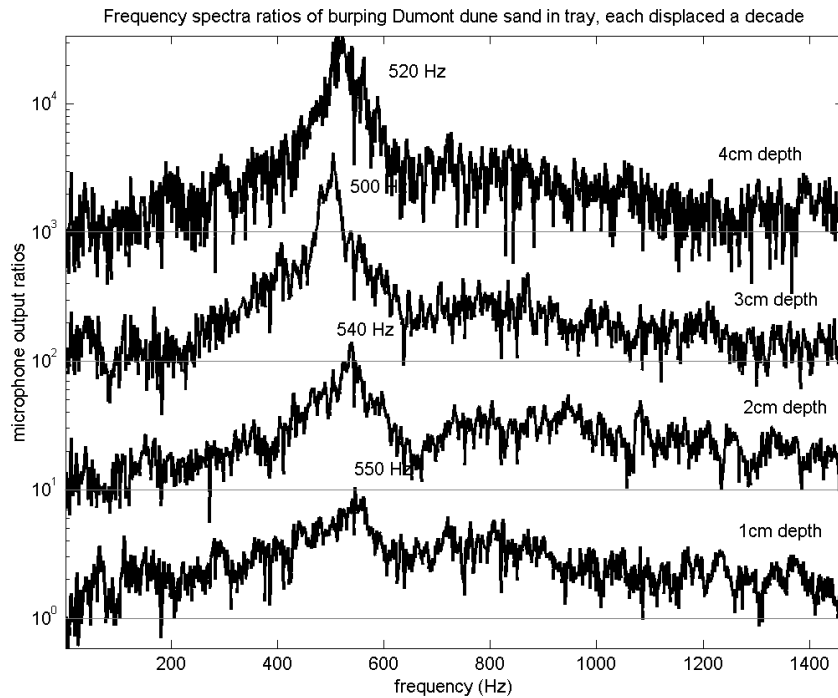


Figure 7.5: Frequency spectra with depth of sand bed in baking tray

With the baking trays, stroking had been limited to the surface. However with the larger chute the stylus could be pushed in to different depths before stroking. A deeper initial depth meant a larger mass of sand being displaced as the stylus moved. Figure 7.8 shows that there did not appear to be any clear correlation between frequency and stylus depth.

It must be noted, however, that the deeper the stylus was initially plunged, the more force had to be applied to move the stylus. It was difficult to quantify the amount of force applied, but the larger the force, the lower the frequency. Hence if we ‘remove’ the additional force applied during shearing from the data points on the right side of Figure 7.8 corresponding to deeper depth, by shifting those points upwards (i.e. higher frequency), it would then appear that the



Figure 7.6: Large chute with styluses for stroking experiment

deeper the stylus, the higher the frequency produced.

The velocity of the strokes were also varied for a fixed stylus depth. Figures 7.9 and 7.10 show the results for styluses of different width, all stroked in the middle of the chute to minimise the effect shown in figure 7.7. For any one stylus, both the frequency and amplitude increased with stroking velocity; the narrow styluses producing higher frequencies than the wider styluses. This may have been due to the wider styluses' edges being closer to the chute walls.

### 7.3 Experimental Setup 3 - Narrow Chute

In order to minimise the variance of frequency across the chute width, a narrow chute 1.5 inches wide and 4 inches deep was made (Figure 7.11). It was

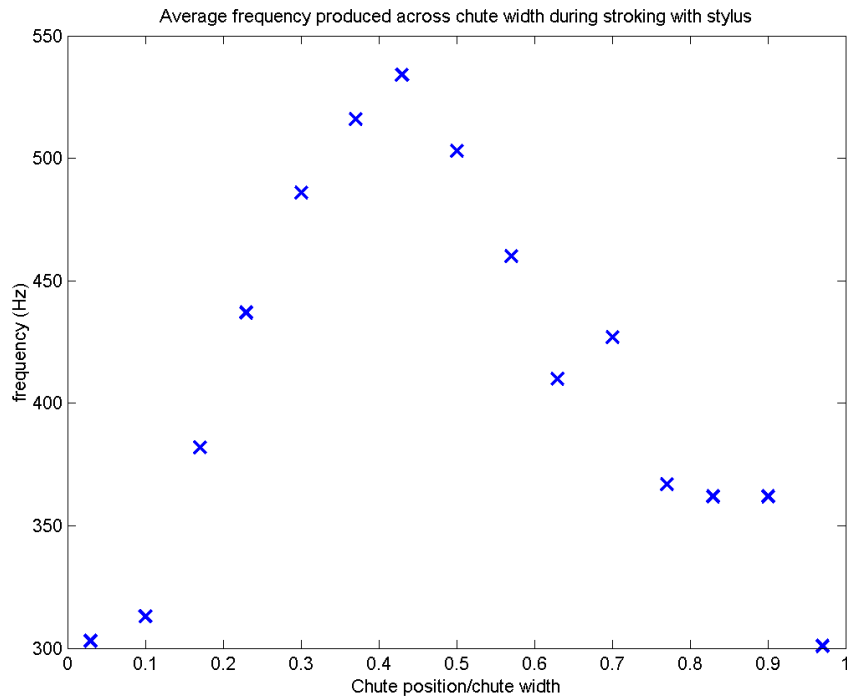


Figure 7.7: Frequency vs position in large chute

wide enough for the narrow styluses to fit with a small margin for sand to slip between the edges and the walls.

Figure 7.12 shows the frequency obtained using the two narrow styluses, and the thin edges of the wider styluses. It appears that narrower styluses result in higher frequencies, which supports the trend in figure 7.9. The aluminium rod produced different frequencies when stroking and plunging (pushing into the sand), but cannot be directly compared with the other styluses' frequencies as it is unclear whether the 'length' to be compared should be the wetted perimeter or the rod diameter.

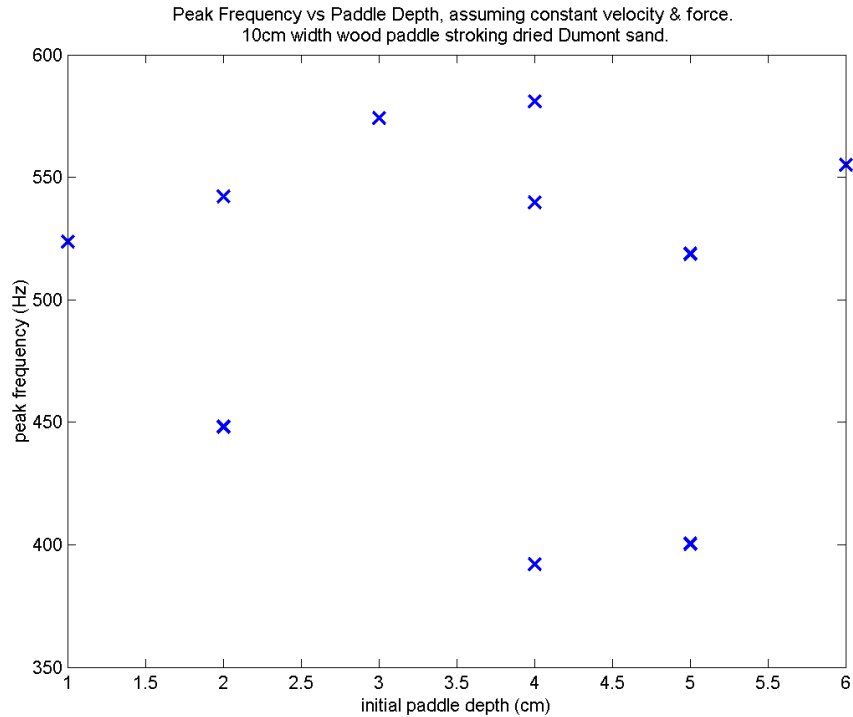


Figure 7.8: Frequency vs stylus depth in large chute

## 7.4 Conclusion

Overall, the frequency of sound produced during stroking varies with stroking velocity, force applied, the stylus width, the depth of the stylus, and position within the chute. Frequency increases with velocity and closeness to the centre-line of the chute, while it decreases with applied force and stylus width. The frequency is also likely to increase with increasing stylus depth. Sound amplitude increases with velocity, and depth of the sand bed.

However it must be noted that because these experiments were not automated, the various factors were not purely independent of each other. For instance to move the stylus at a higher velocity, larger force was also applied.

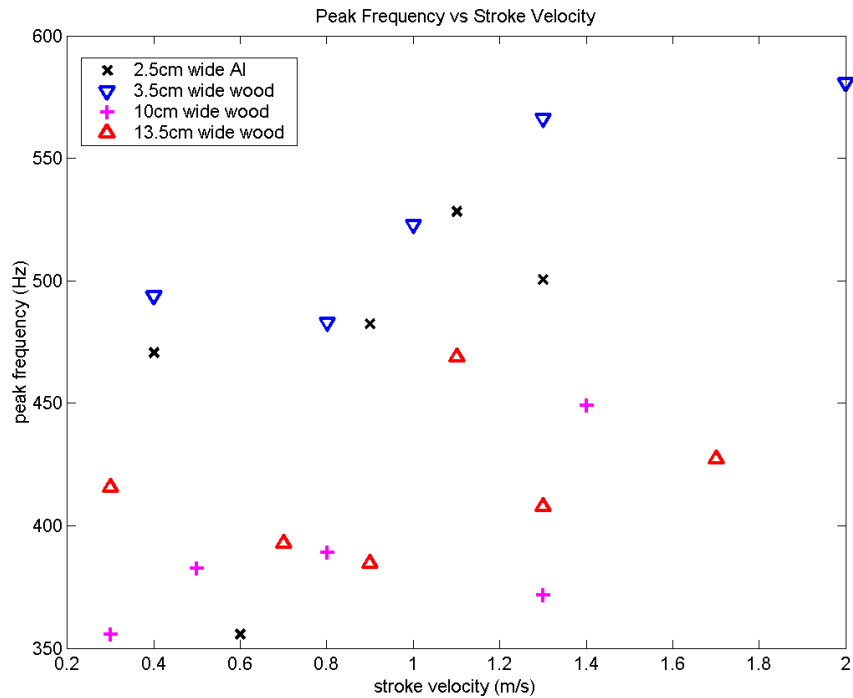


Figure 7.9: Frequency at different stroke velocities in large chute

Assuming that the depth of the sand being pushed before the stylus remained constant during the velocity experiments, then the trend of frequency increasing with velocity is consistent with the observation made by Douady et al [10] that frequency varies with the ratio of pushing velocity to the height of the pushed sand mass.

Comparing the low amplitude sound produced in the small inclined chute and rotating flasks to that produced by stroking, the sound from stroking was at a higher frequency and of louder amplitude. Following the observations noted above, the louder amplitude may be because the sand was displaced at higher velocities than in the chute; the frequency was also higher likely for that same reason. Another possibility is that the inclined chute was too short for the 'burp-

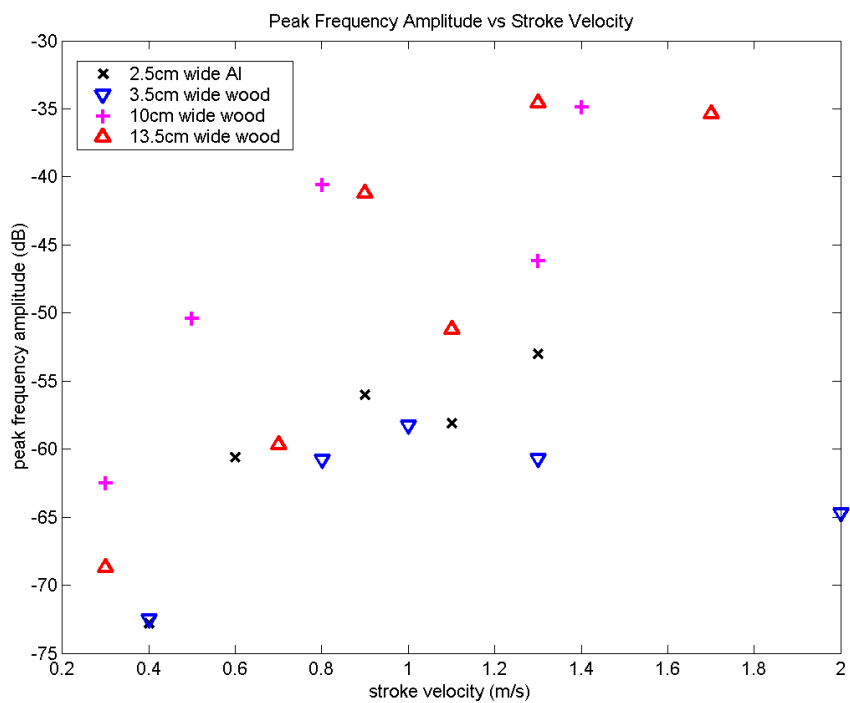


Figure 7.10: Frequency and amplitude at different stroke velocities in large chute



Figure 7.11: Narrow chute for stroking experiment

ing' to be sufficiently amplified.

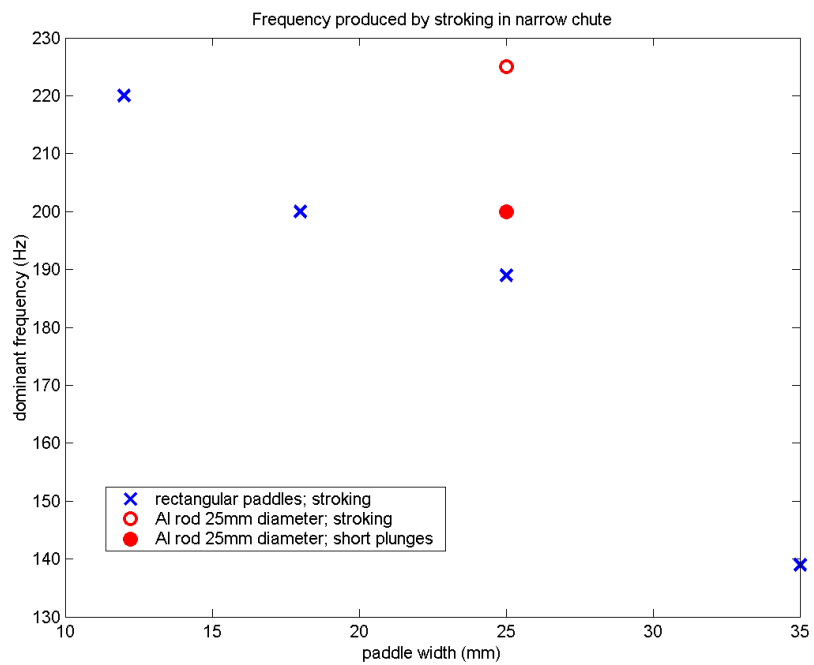


Figure 7.12: Frequency spectra of different styluses in narrow chute

## CHAPTER 8

### POURING & SHAKING

Shaking ‘sounding’ sand in a jar was the very first laboratory experiment to produce ‘burping’ and was the easiest to reproduce. Initially little attention was paid to the sound produced during shaking as it appeared to involve a different mechanism from ‘booming’. However when dried ‘sounding’ sand was poured from one bucket into another, loud low frequency was generated, similar to that produced by shaking a jar of similar sand.

#### 8.1 Pouring

It was found that when pouring ‘sounding’ sand from one bucket to another made of rigid material and placed on the ground, a loud low frequency sound was produced. Its frequency decreased if the sand was poured from a height just above the bucket mouth and aimed towards the side or corner of the bucket. Because it was difficult to maintain constant flowrate manually, all flowrates mentioned here pertaining to pouring are estimates.

Figure 8.1 shows the frequency spectrograms of the microphone recordings obtained when Dumont sand was poured into a bucket at eight increasing flowrates. A high frequency sound (around 900 Hz) was produced initially, which rapidly decreased and then remained steady. When the pouring flowrate was increased, this steady frequency dropped from 500 to 250 Hz, with harmonics showing the same decreasing behaviour present. This was consistent with the figure published in Vibrationdata’s March 2006 newsletter [1].

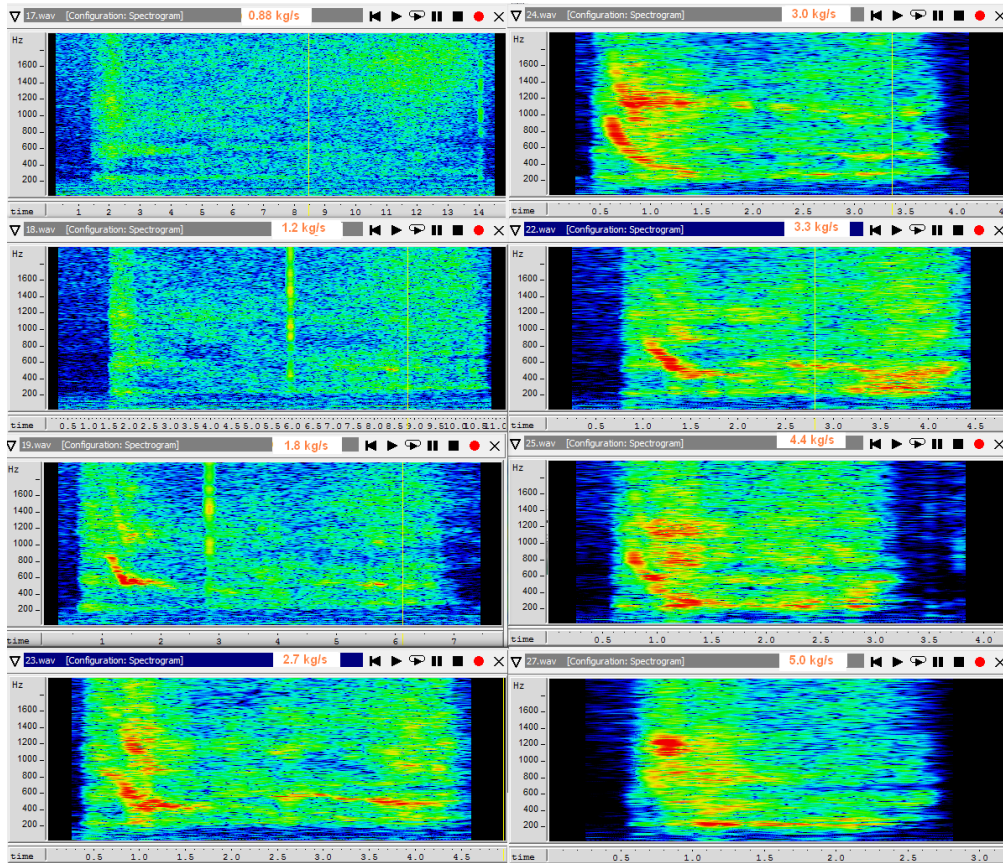


Figure 8.1: Spectrograms of poured Dumont dune sand at increasing flowrates (0.88kg/s in top left spectrogram, increasing down the column and the next to 5.0kg/s in the bottom right spectrogram.)

The frequency spectra of the steady portion of the microphone recordings are shown in figure 8.2, with each spectrum displaced for clarity. As mentioned previously, the peak frequency decreases with increasing flowrate. The peak frequencies and corresponding amplitudes are plotted in Figures 8.3 and 8.4, and show the decreasing peak frequency and increasing amplitude with increasing flowrate.

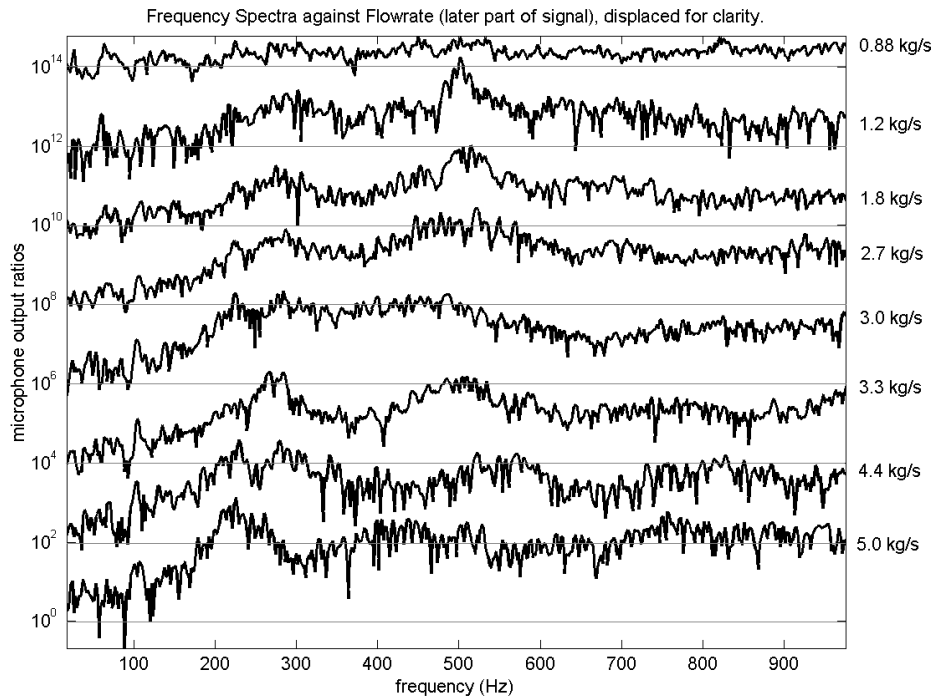


Figure 8.2: Frequency spectra of the portion of the signals where the frequency has decreased to a steady value. Each spectra corresponding to a different flowrate is displaced by a decade for clarity.

## 8.2 Jar Shaking

### 8.2.1 Manual Jar Shaking

A jam jar was filled to approximately one-third capacity with ‘sounding’ sand (see Figure 8.6). Holding the jar in one hand and moving it through a 90 degree rotation at the elbow at approximately 0.5 Hz produced low frequency sound. Alternatively, the jar can be shaken in the axial direction, at around 1-2 Hz with 10cm displacement amplitude to produce the same effect.

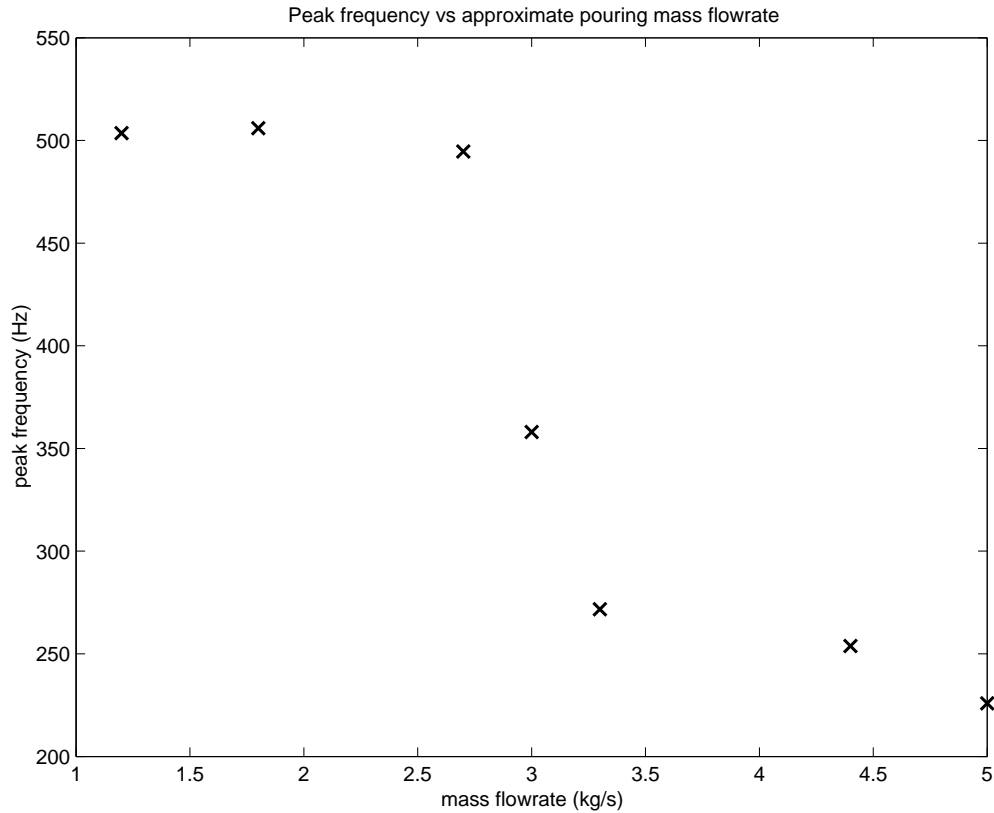


Figure 8.3: Peak frequency during pouring at different flowrates

As shown in figure 8.7, ‘sounding’ sand like Eureka dune sand produces a broadband frequency peak at 250 Hz which Ottawa sand, shaken in the same manner, does not. This difference is also shown in Figures 8.8 and 8.9, which show the spectrograms of a jar of dried Dumont dune sand and a similar jar of glass beads, both shaken in a similar manner.

## 8.2.2 Long Tube

A glass tube, 3 feet long and with a diameter of 1.62 inches (Figure 8.10) was also used as a longer ‘jar’, to increase the time spent in the middle section of the

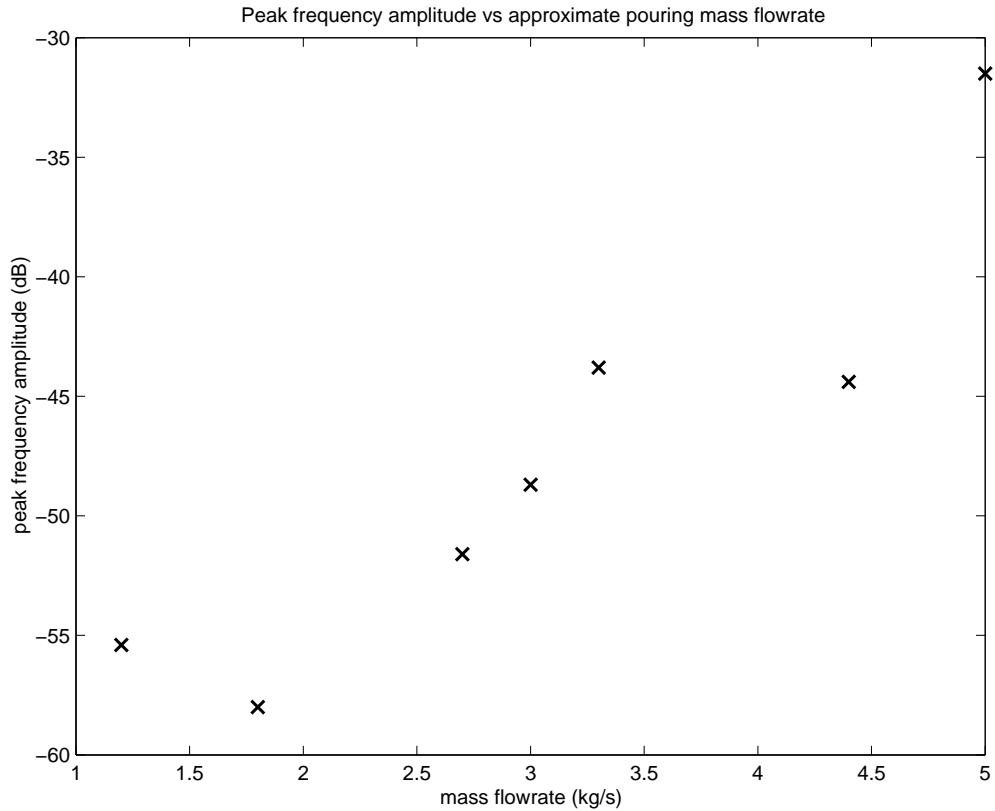


Figure 8.4: Peak frequency amplitude at different flowrates



Figure 8.5: Large displacement shaking sequence

container. This was to investigate whether the sand hitting the ends of the ‘jar’ was contributing to sound production.

It was found that sound could be produced even when ‘sounding’ sand was just slid from one side of the tube to another, without the sharp jerking motions employed with shaking the smaller jam jars. However the tube had to be at an



Figure 8.6: Jar of dried Dumont dune sand

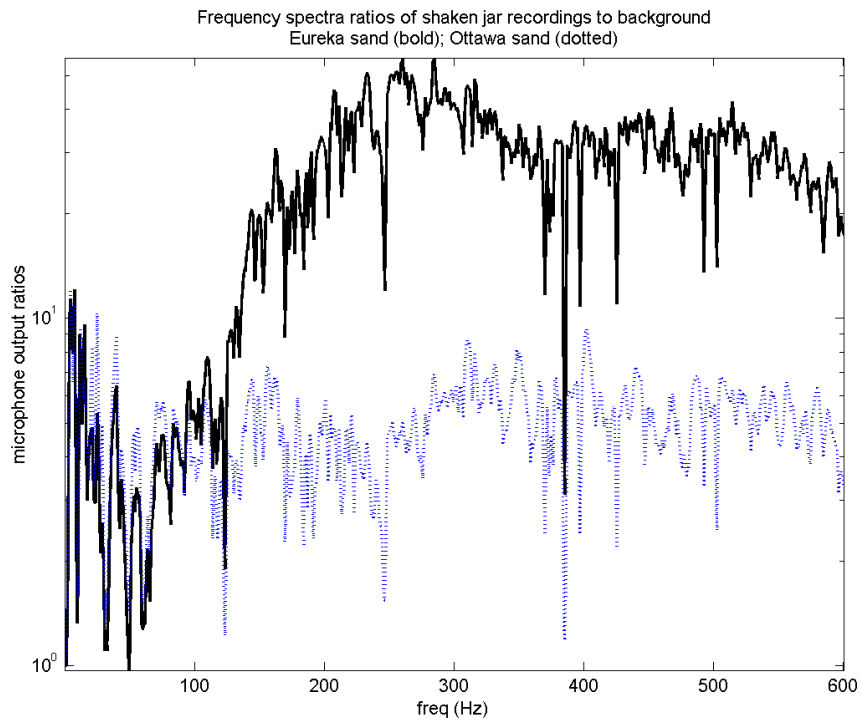


Figure 8.7: Frequency spectra ratios of shaken jars of Eureka dune and Ottawa sand

angle of more than  $60^\circ$  above the horizontal for sound production. Figure 8.11 shows the spectrogram obtained when the tube was tilted from horizontal to vertical slowly.

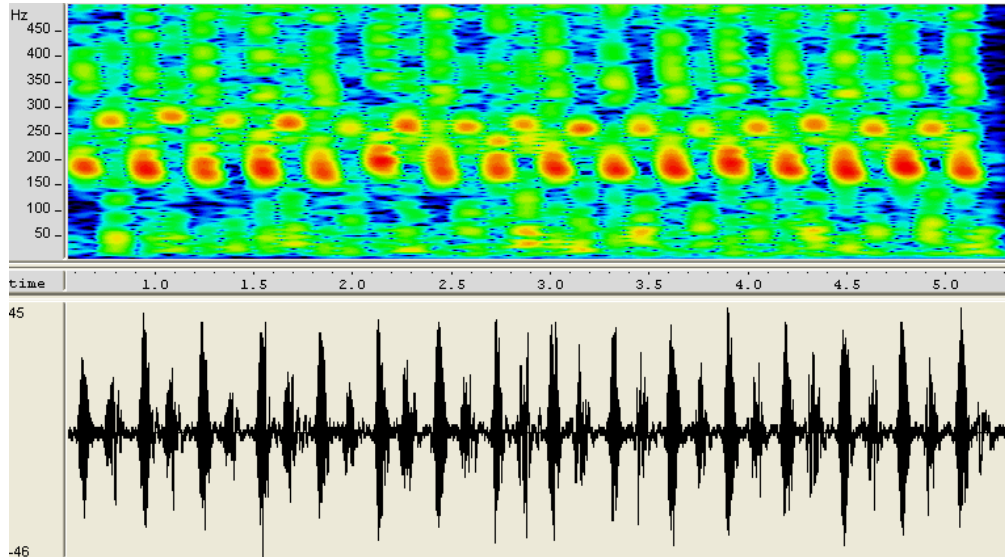


Figure 8.8: Spectrogram of shaken jar of Dumont dune sand

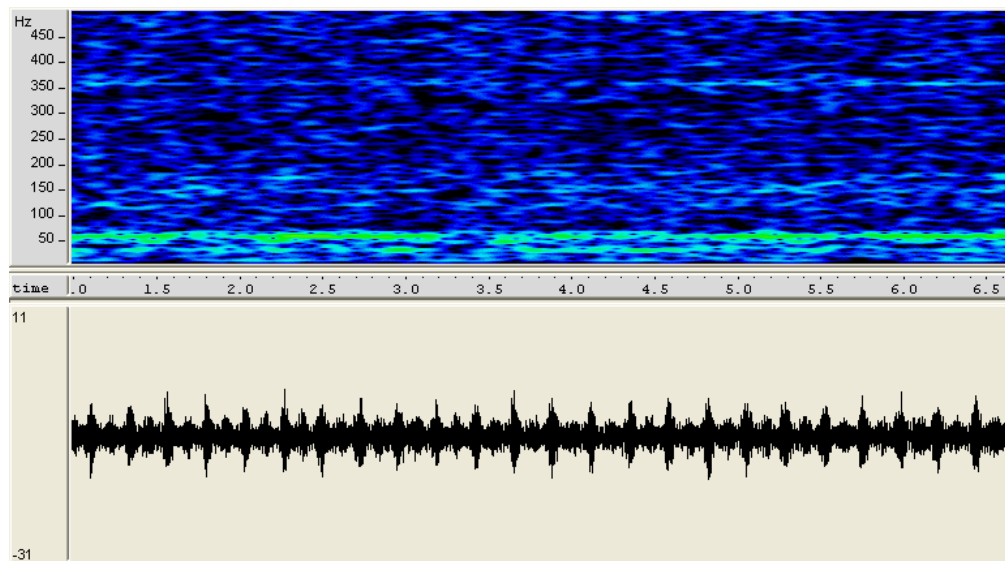


Figure 8.9: Spectrogram of shaken jar of glass beads

### 8.2.3 Controlled Shaking

In order to conduct the shaking experiments with a fixed frequency and amplitude, a shaker was used to shake the mounted jars axially.



Figure 8.10: Glass tube 3ft long, 1.62inch diameter

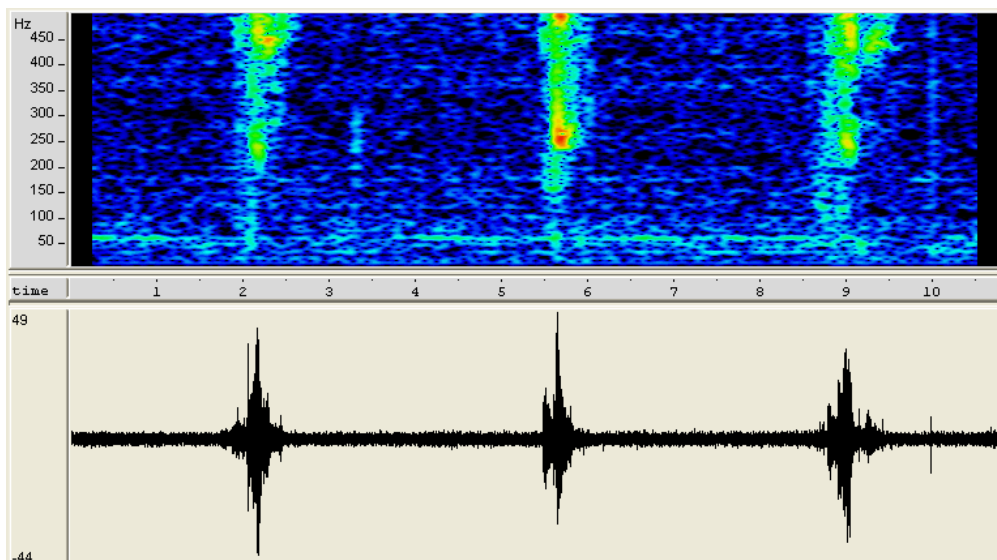


Figure 8.11: Spectrogram and time-trace when tube is tilted from horizontal to vertical

The shaker used was a VTS 600 with peak-to-peak displacement amplitude of 1 inch. A glass jar was glued to an aluminium frame which could then be mounted on the shaker, shown in figure 8.12. This setup was not really adequate to reproduce manual shaking as its stroke amplitude was small, and at the low frequencies required, its acceleration was insufficient to move the sand within the mounted jar. Nonetheless, we believed that the shaken sand would show some characteristics distinguishing ‘sounding’ sand from ‘silent’ sand.

Figures 8.13 and 8.14 show the microphone signals obtained from Dumont dune sand and glass beads respectively when shaken at different frequencies and different input gain. Both exhibit ‘bursts’ in the signals corresponding to

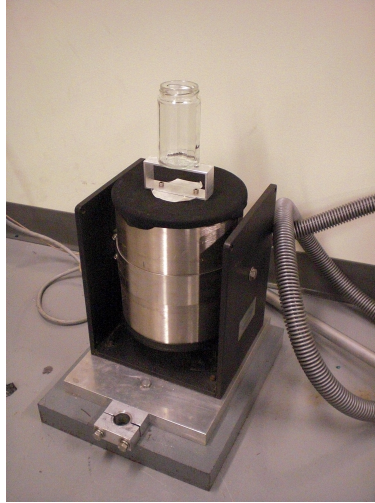


Figure 8.12: Shaker with mounted glass jar

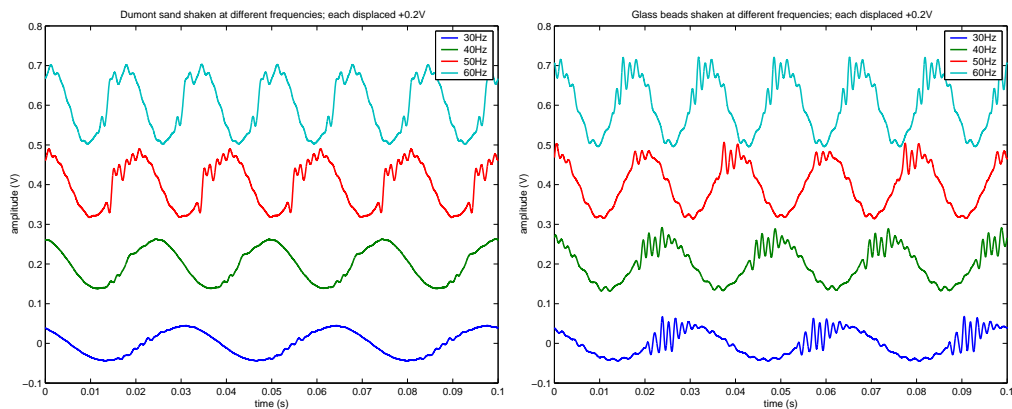


Figure 8.13: Microphone signals of Dumont dune sand and glass beads at different shaking frequencies

the upward motion of the jar. When the input gain is increased, the start of the 'bursts' shift closer to the top of the displacement cycle. Interestingly with glass, at some frequencies the 'bursts' repeat every other cycle.

To provide a comparison, the empty jar was filled with a rigid mass equal to the mass of Dumont dune sand or glass beads used. These signals for the 'empty' jar were then subtracted from those of Dumont dune sand and glass

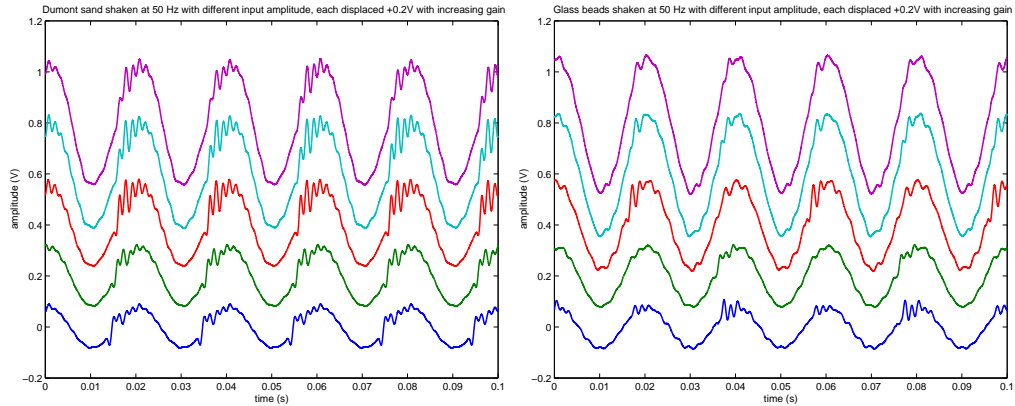


Figure 8.14: Microphone signals of Dumont dune sand and glass beads shaken at 50 Hz with increasing excitation amplitude (lowest at bottom)

beads, as shown in Figures 8.15 and 8.16, with the original signals for comparison.

Spectrograms were taken of these ‘difference’ signals, shown in Figures 8.17 and 8.18. Due to the poor resolution we can only conclude that the ‘bursts’ have a broadband frequency centred about 700 Hz, with an envelope of 250-300 Hz. Interestingly, the appearance of the ‘bursts’ coincide with a ‘roiling’ motion at the surface of the Dumont dune sand, but no such surface effects appear in the glass beads despite having ‘bursts’ too. This ‘roiling’ surface motion appears to be similar to Benard convection.

### 8.3 Summary

From the shaking experiments, it is clear that a large acceleration has to be applied for sound production; while with the tube, change of angle has to be relatively large. These both involve a large flowrate, which the pouring experi-

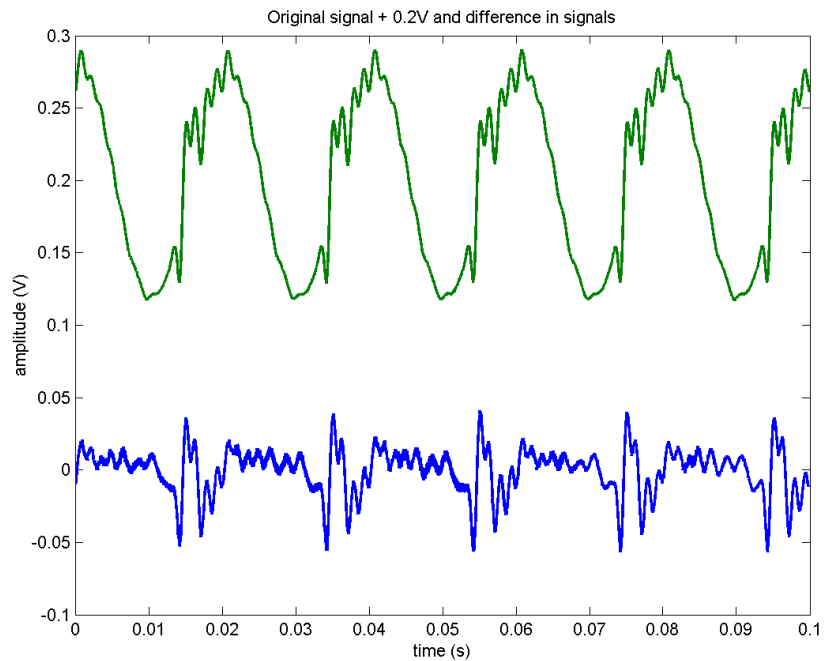


Figure 8.15: Original Dumont dune sand signal displaced +0.2V; below: difference in signal between Dumont dune sand and 'empty' jar, shaken at 50 Hz.

ments agree with. Pouring into buckets involve a rapid change of momentum and packing fraction when the sand hits the bucket floor, which also occurs when direction is reversed in jar-shaking. Hence a large flowrate and change of momentum or packing fraction could be crucial to low frequency sound production.

This trend of higher flowrates producing lower frequency appears to contradict the observations from the inclined chute, rotating flask and stroking experiments, where frequency increases with velocity. Coupled with the fact that the frequency of sound produced via pouring and shaking is generally higher than the 100-150 Hz obtained in the other experiments, it may be that even though the two sounds are closely related, they are not produced through the same

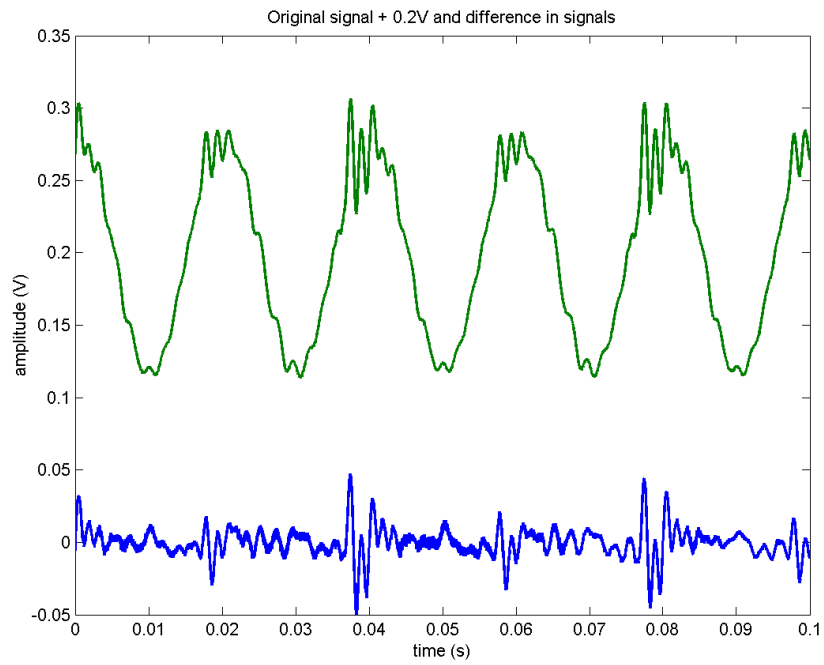


Figure 8.16: Original glass beads signal displaced +0.2V; below: difference in signal between glass beads and 'empty' jar, shaken at 50 Hz.

mechanism and it would not be appropriate to refer to them both as 'burping'.

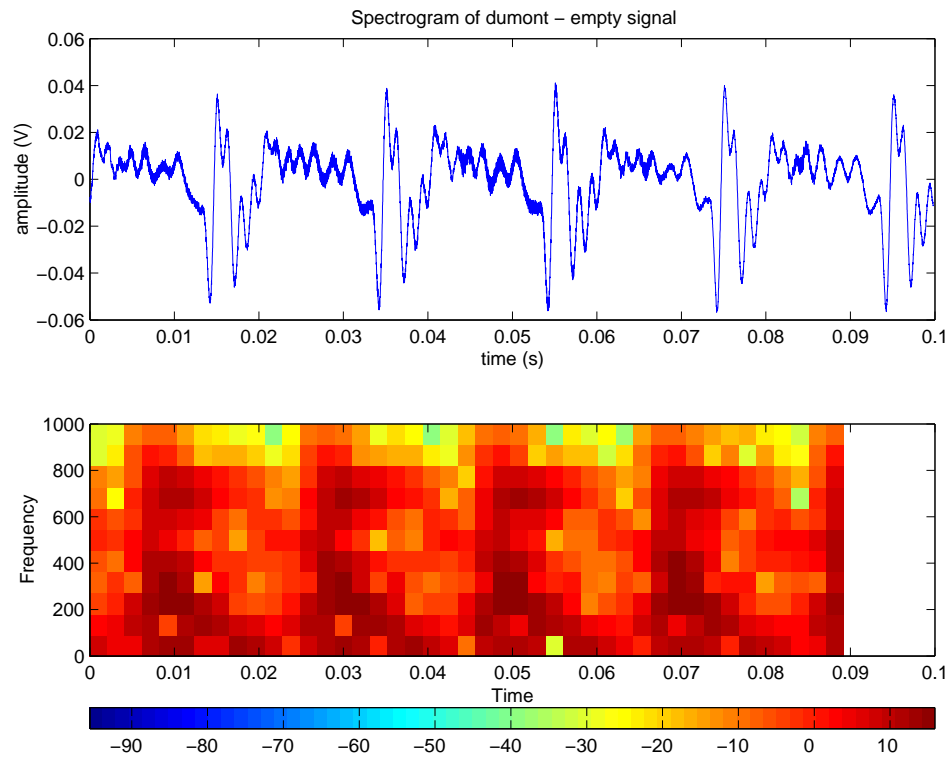


Figure 8.17: Spectrogram of signal difference between Dumont dune sand and 'empty' jar, shaken at 50 Hz

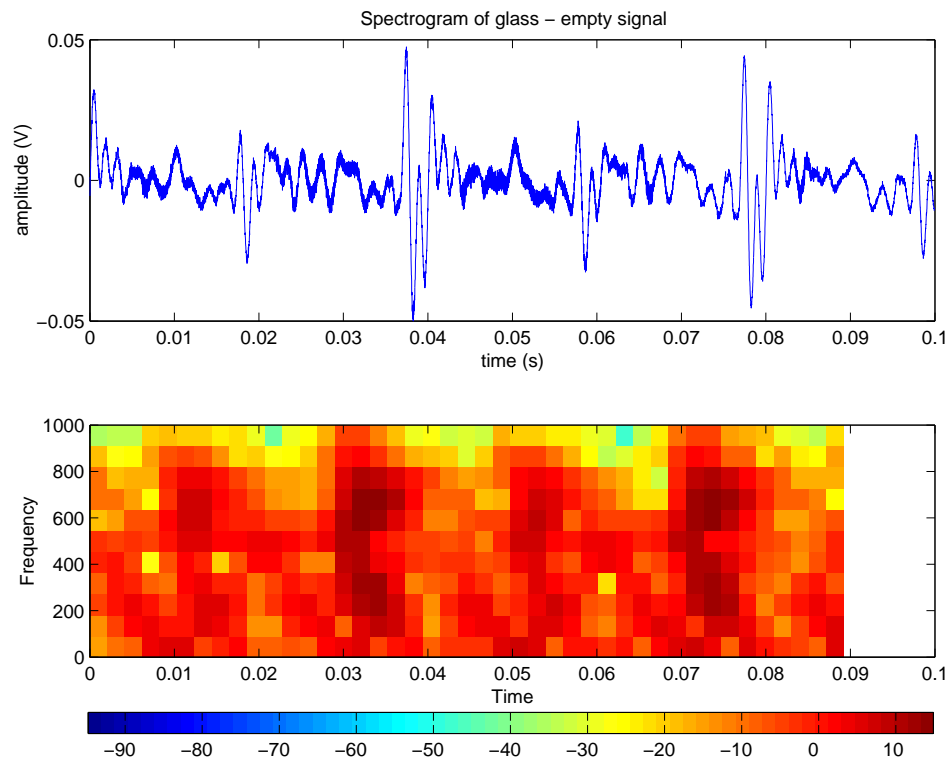


Figure 8.18: Spectrogram of signal difference between glass beads and 'empty' jar, shaken at 50 Hz

## CHAPTER 9

### PHASE TRANSITION

A periodic three-dimensional numerical simulation by Silbert [33] of a dense, inclined granular flow exhibited significant oscillations in kinetic energy as the inclination was decreased to within two degrees of the stopping angle. These oscillations were also present in both the normal velocity autocorrelation and inter-particle contact force time-correlation functions. Finally, the coordination number was seen to vary periodically between one and four, which indicates the formation of particle chains. Indeed, Silbert's Fig. 5 showed the cyclic appearance of 'force chains' in the lower part of the numerical simulation. Similar simulations by Silbert et al. [34] that involved a less bumpy base exhibited oscillations between the random and ordered states without the formation of chains.

Mills and Chevoir [23] attributed Silbert's oscillations [33] to a decrease in stress ratio with inertia parameter near the jamming transition, where enduring contact forces dominate instantaneous collisions. Instead, we interpret the oscillations' appearance as being related to the volume fraction. Decreasing the inclination angle in Silbert's simulations is equivalent to increasing the steady state solid volume fraction in a dense sheared flow and, beyond a certain value, oscillations of significant amplitude, associated with a phase change interrupted by the formation of force chains, are initiated. This phase change takes place between a random collisional state in which the steady state volume fraction is relatively low, and an ordered collisional state in which the steady state volume fraction is higher.

Richard has commented (private communication) that in Silbert's oscillations the particle stiffness employed probably has a large influence on observed

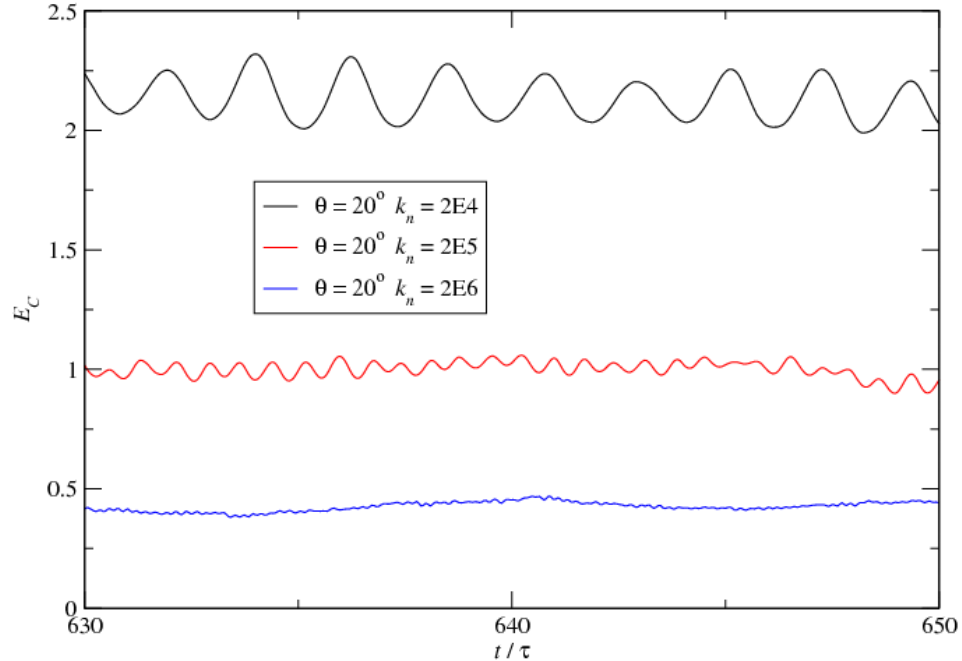


Figure 9.1: Oscillations in kinetic energy at different particle stiffnesses; reproduced with permission from Richard et al.[29].

phenomena [21]. He then conducted numerical simulations under conditions similar to Silbert's, and showed that with increasing particle stiffness, the oscillation frequency increased, while its amplitude decreased (Figure 9.1). Consequently, any model should take into account the sensitivity of the restoring force to particle stiffness, and the possibility that it changes the collisional pressure.

Kinetic theory provides a monotonic increasing relationship between dimensionless pressure  $p/\rho_s T$  and solid volume fraction  $\nu$ , in the collisional random or 'glassy' region. In this section, we explore some models that go beyond this relationship and attempt to incorporate the behaviours observed by Silbert and Richard.

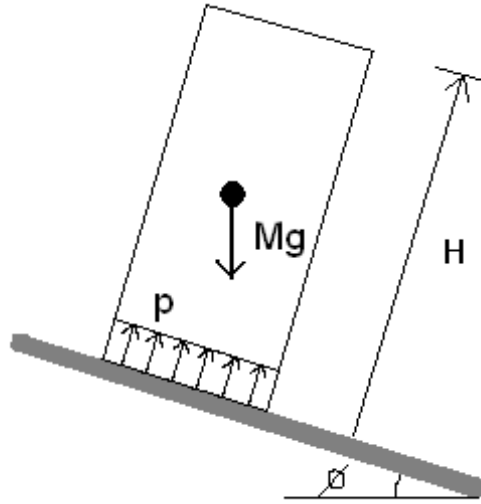


Figure 9.2: Homogeneous phase transition model

## 9.1 Homogeneous Phase Transition

Here, we consider a block of granular material of height  $H = H_0 + H_1(t)$ , base cross-sectional area  $A$ , and uniform solid volume fraction  $\nu = \nu_0 + \nu_1(t)$ , shown in figure 9.2, as a spring, with mass  $M$  that of the block of granular material. The restoring force is pressure  $p = p_0 + p_1(\nu_1)$ . Again, terms with subscript 0 are associated with steady state conditions, while those with subscript 1 are perturbations so small that their products can be neglected.

The mass of the block  $\rho_s \nu A H$  remains constant, which gives

$$\dot{\nu}_1 H_0 + \nu_0 \dot{H}_1 = 0, \quad (9.1)$$

and

$$\ddot{\nu}_1 H_0 + \nu_0 \ddot{H}_1 = 0. \quad (9.2)$$

At equilibrium, the gravitational force is balanced by  $p_0$ , so resolving forces

in the vertical direction reduces to

$$p_1 A = M \ddot{H}.$$

Substituting  $M = \rho_s v A H$  and Equation 9.2 gives

$$\ddot{v}_1 = -\frac{1}{\rho_s H_0^2} p_1(v_1). \quad (9.3)$$

### 9.1.1 Cubic Curve

As mentioned previously, kinetic theory for colliding grains provides a relationship that links the normalised pressure and solid volume fraction in the dense, random regime of a granular flow. It is difficult for such a random, collisional flow to transform into a more ordered collisional crystalline regime at an increased solid volume fraction in which it typically has a higher stiffness. Our first attempt to describe the transition between the two regimes is to join them with a cubic curve, with the downward curve between the local extrema representing a transition region that corresponds to unstable force-equilibria. In this transition region the system is a mixture of both the random and ordered collisional regimes.

The idea of using a cubic curve to represent a transition is not new. For molecules of a Van der Waals gas, the change from short range repulsion to long range attraction is represented by a cubic curve. Vainchtein et al [36] also use a cubic curve to describe the elastic energy density in solid-solid phase transitions. Mark Shattuck (private communication) also utilises a cubic curve to relate random collisions and ordered collisions in granular material.

An alternative relationship considered was the piecewise linear oscillator

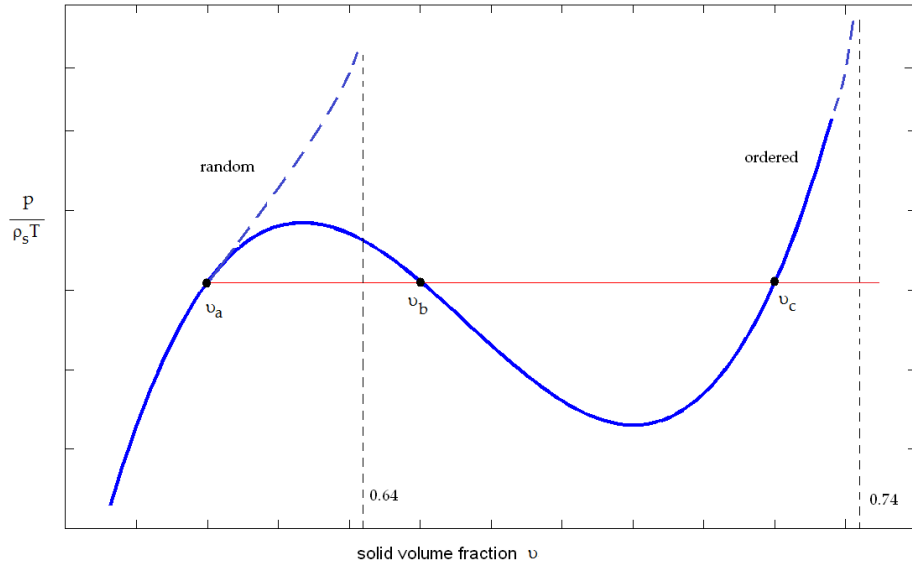


Figure 9.3: Cubic relationship between  $p/\rho_s T$  and solid volume fraction  $\nu = \nu_0 + \nu_1$ , going from a random collisional regime to an ordered collisional regime as  $\nu$  increases. The horizontal line indicates the current force-equilibrium value  $p_0/\rho_s T_0$ , and the corresponding three force-equilibrium points. Placing the origin at one of these points gives  $p_1/\rho_s T_0$  against  $\nu_1$ .

used by Shaw and Holmes [31], but with the two straight lines separated by a horizontal line. However this meant the pressure expression is conditional on the value of  $\nu$  at any time, and there were discontinuities in the slope, which could possibly have presented difficulty in the non-homogeneous system. Also while solutions were easily obtainable for each linear 'piece', they could not be combined to form a single analytical solution as the time at which the system crossed over into each new 'piece' was unknown. Hence we chose to use the smooth cubic curve mentioned above.

The steady state pressure  $p_0 \approx (H - y)\rho_s \nu_0 g \cos \phi$ , and the isothermal granular temperature  $T_0$  is given by the same expression used in the perturbation model (equation 6.8). The mathematical expression for the cubic curve

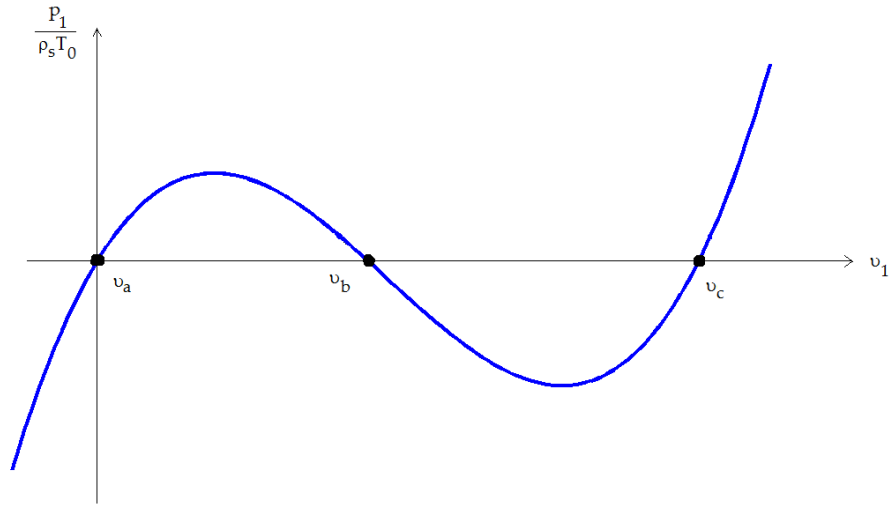


Figure 9.4: Relationship between pressure fluctuation and volume fraction fluctuation when steady state corresponds to a stable force-equilibrium point.

$p_1(\nu_1)/\rho_s T_0$  is determined from the values of the outermost force-equilibrium points ( $\nu_a$  and  $\nu_c$ ) and their respective slopes, and then translating horizontally with respect to steady state volume fraction  $\nu_0$ .

For  $p_1/\rho_s T_0 = C_1 (\nu_1 - \nu_a)(\nu_1 - \nu_b)(\nu_1 - \nu_c)$ , equation 9.3 becomes:

$$\ddot{\nu}_1 = -\frac{T_0 C_1}{H_0^2} (\nu_1 - \nu_a)(\nu_1 - \nu_b)(\nu_1 - \nu_c) . \quad (9.4)$$

The steady state volume fraction  $\nu_0$  increases as the inclination angle  $\phi$  decreases. Figure 9.4 shows the cubic curve when  $\nu_0$  (and hence the origin) corresponds to  $\nu_a$ . As  $\nu_0$  increases, the origin moves upwards along the curve. Correspondingly  $\nu_b$  decreases and  $\nu_c$  increases. Small perturbations from the origin  $\nu_a$  result in small amplitude oscillations.

When  $\nu_0$  increases to the extent that the origin moves past the local maxima, the origin then corresponds to the unstable (repulsive) force-equilibrium point

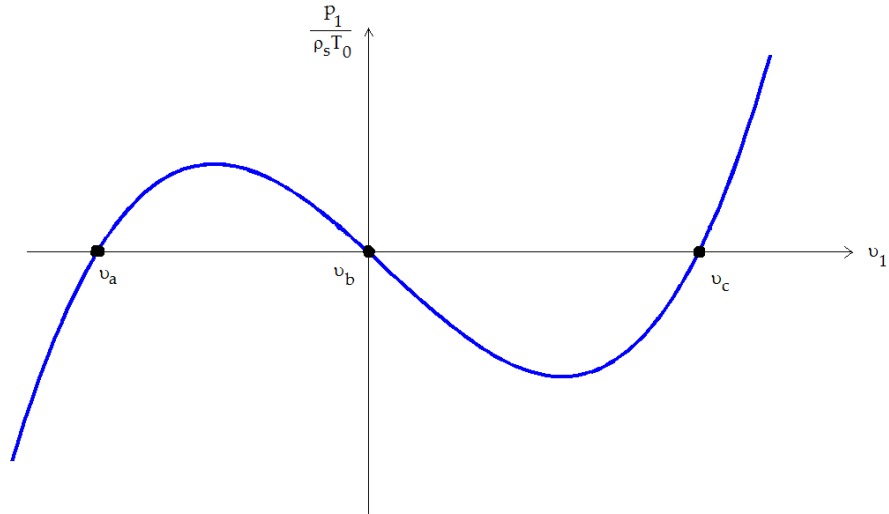


Figure 9.5: Relationship between pressure fluctuation and volume fraction fluctuation when steady state corresponds to an unstable force-equilibrium point.

$\nu_b$  (Figure 9.5). Now small decreases from the origin result in large amplitude oscillation, because the excursions of the solid volume fraction then extend to the stable force-equilibrium point  $\nu_a$ . This trend is shown in figure 9.6. Note that positive perturbations from  $\nu_b$  are not considered, because they would be attracted to  $\nu_c$  in the ordered regime.

This behaviour is similar to what Silbert [33] sees - large amplitude oscillations are present past a certain value of  $\nu$ ; while, below it, oscillations are small. Such oscillations take place provided that the base is not too bumpy. Very bumpy bases appear to facilitate the formation of force chains. However this simple model does not explicitly depend on particle stiffness and, hence, does not reflect Richard et al.'s [29] findings.

Note that the shape of the excursions are not exactly the same as Silbert's, be-

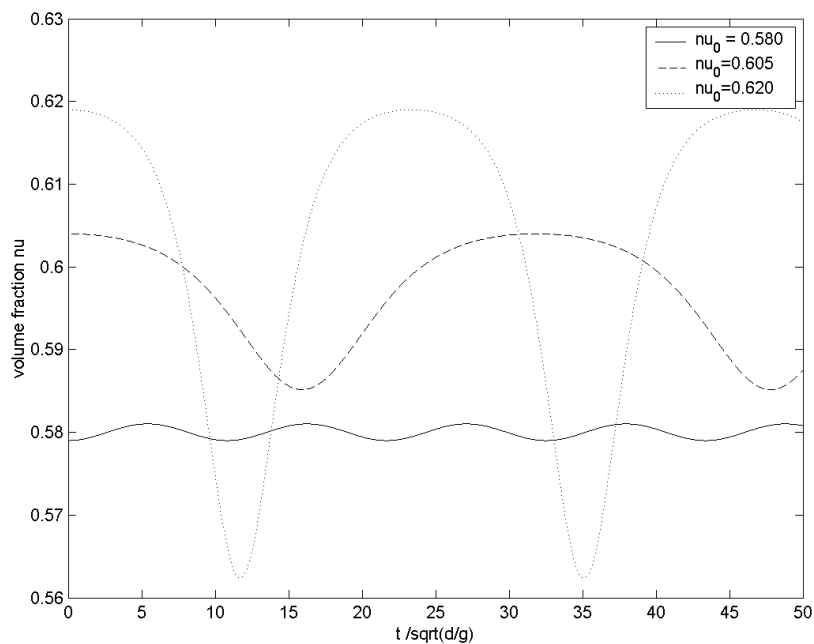


Figure 9.6: Excursions in  $\nu$  for steady states  $\nu_0=0.580$  (solid line), 0.605 (dashed line) and 0.620 (dotted line). Local maxima is at 0.598.

cause we plotted volume fraction against time instead of kinetic energy, which would be inverted. Silbert also saw a small kink at the bottom of each of his cycles, which we believe is due to the motion of the particles moving over the layer below them.

Here we have used  $\nu = 0.64$  as the rightmost force-equilibrium point. This is not strictly appropriate as 0.64 is the largest possible value in a collisional regime with random packing, and not a typical solid volume fraction in a collisional regime with ordered packing.

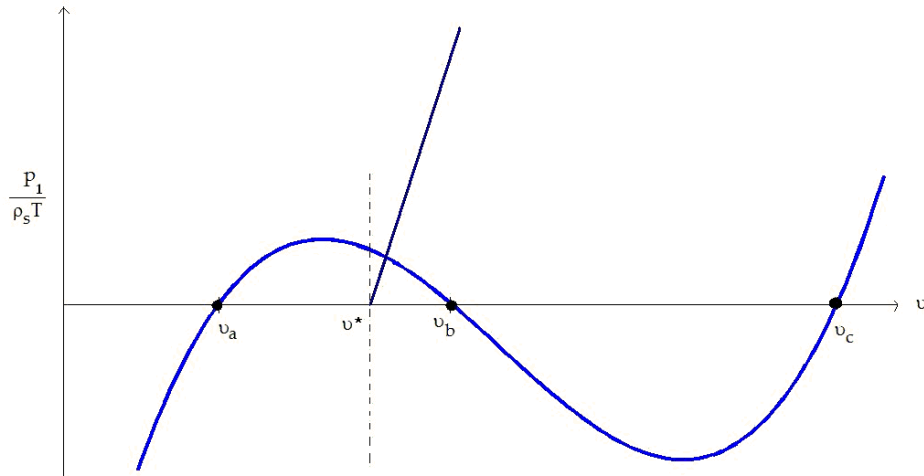


Figure 9.7: Relationship between  $p/\rho_s T$  and  $\nu$ , with cubic curve representing collisional regime and monotonic curve representing contact regime. The horizontal line corresponds to the steady state ratio  $p_0/\rho_s T_0$  for inclination  $\phi$ , at which  $p_1=0$ .

### 9.1.2 Two Branches

An improved model includes both the cubic curve and a straight line of larger slope, shown in figure 9.7. The cubic curve still represents the collisional regime, but now attention is focused on the two lower force-equilibrium points. The formation of particle chains reduces the mobility of the system, mobility that is necessary to reach the ordered regime. The added straight line describes the variation of normalized pressure with the compression and extension of the chains; hence, particle stiffness can be incorporated here.

Similar to the previous model, small perturbations in  $\nu$  to the left of the unstable force-equilibrium point result in large excursions. However when  $\nu \geq \nu^*$  particle chains start forming, so the system follows the sum of the straight line and the cubic curve, shown in figure 9.8.

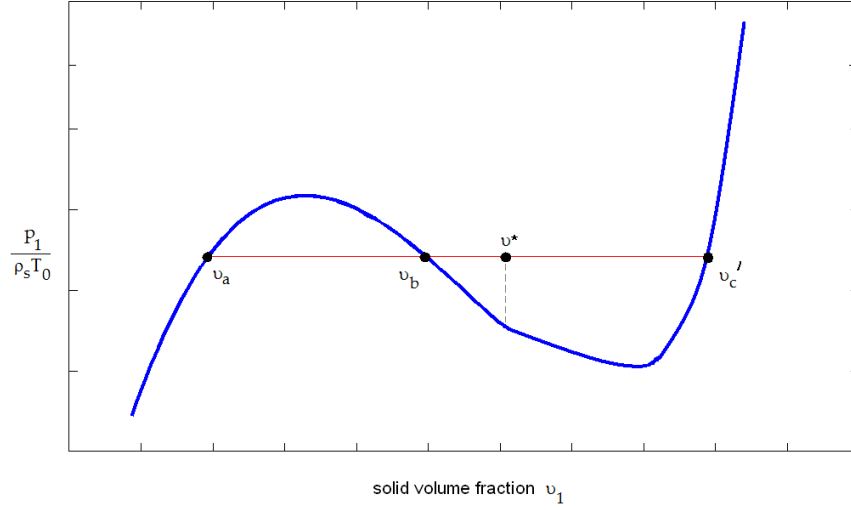


Figure 9.8: Relationship between  $p/\rho_s T$  and  $\nu$ . For  $\nu \geq \nu^*$  the curve is the sum of the cubic curve representing collisions and the straight line representing particles in contact. The horizontal line shows the steady state ratio  $p_0/\rho_s T_0$  at inclination  $\phi$ , and the corresponding three force-equilibrium points.

The pressure expression for the contact branch can be derived using the methods of Jenkins and Strack [16]:

$$d\sigma_{ij} = B_{ijkl} dE_{lk} , \quad (9.5)$$

where

$$B_{ijkl} = \psi_3 (\delta_{ik}\delta_{jl} + \delta_{il}\delta_{jk}) + \psi_5 (\delta_{ik}h_j h_l + \delta_{jl}h_i h_k + \delta_{il}h_j h_k + \delta_{jk}h_i h_l) , \quad (9.6)$$

assuming that the normal stiffness  $K_N$  and tangential stiffness  $K_T$  are approximately equal, and  $\vec{h}$  is the direction of anisotropy. The coefficients  $\psi_3$  and  $\psi_5$  are defined as

$$\psi_3 = (1 - \epsilon) \frac{nd^2 k}{8} \frac{k}{3} K + 3\epsilon \frac{nd^2 k}{8} \frac{k}{15} K$$

and

$$\psi_5 = \frac{\epsilon nd^2}{5} \frac{k}{8} k K ,$$

where  $\epsilon = 0.5$  is the strength of contact anisotropy,  $n$  is the number of particles per unit volume,  $d$  is the average particle diameter,  $k = 3$  is the coordination number and  $K$  is the particle stiffness.

Rewriting the stress-strain relationship as spatial derivatives with  $\vec{h} = \vec{k}$ ,

$$\frac{\partial \sigma_{33}}{\partial Y} = (2\psi_3 + 4\psi_5) \frac{\partial E_{33}}{\partial Y}. \quad (9.7)$$

Finally, if we assume that there is no strain in the two orthogonal directions,  $E_{33} = \Delta = -(\nu_1 - \nu^*)$ , where  $\nu^*$  is where particle chains start forming. Then, employing  $n = 6\nu_0/(\pi d^3)$ ,

$$\frac{\partial \sigma_{33}}{\partial Y} = -\frac{\nu_0 k}{4\pi d} K \left(2 + \frac{8}{5}\epsilon\right) \frac{\partial \nu_1}{\partial Y}, \quad (9.8)$$

and, for constant  $K$ ,

$$\sigma_{33} = -\frac{\nu_0 k}{4\pi d} K \left(2 + \frac{8}{5}\epsilon\right) (\nu_1 - \nu^*). \quad (9.9)$$

Because the particles forming a chain continue to experience collisions, the total pressure is given by

$$\begin{aligned} p_{1,contact} &= p_{1,collisions} - \sigma_{33} \\ &= \rho_S T_0 C_1 (\nu_1 - \nu_a) (\nu_1 - \nu_b) (\nu_1 - \nu_c) + \frac{\nu_0 k K}{4\pi d} \left(2 + \frac{8}{5}\epsilon\right) (\nu_1 - \nu^*). \end{aligned} \quad (9.10)$$

It must be noted that particle stiffness affects the system even if it is purely collisional. For a system with higher stiffness, the amount of particle overlap in a collision is less and hence the effective solid volume fraction is reduced. We incorporate this effect by contracting both the collision and contact branches relative to the leftmost equilibrium point when the particle stiffness is increased. Here, we take the effect of particle stiffness to be equal on both branches - i.e.

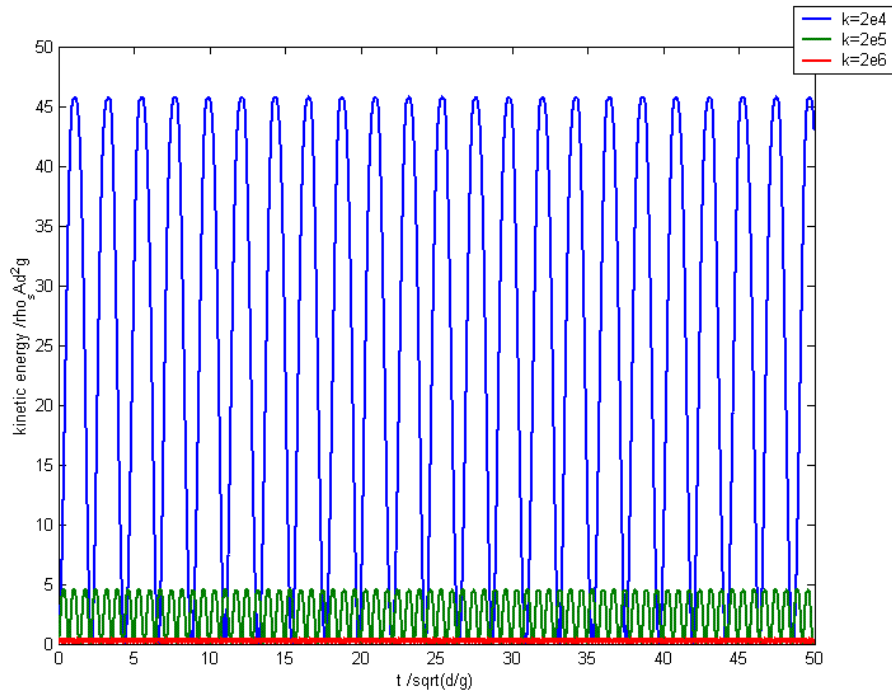


Figure 9.9: Fluctuations in kinetic energy corresponding to small perturbations about the unstable force-equilibrium point  $v_b=0.621$ . The other equilibria are at  $v=0.581$  and  $0.700$ , and  $v^{ast}=0.603$ . Particle stiffnesses  $K = 2 \times 10^4$ ,  $2 \times 10^5$  and  $2 \times 10^6$  mg/d (blue, green and red lines).

an increase in  $K$  results in a similar contraction factor - as it is unclear whether particle stiffness has greater effect during collisions or during contact.

Figure 9.9 shows that increasing particle stiffness results in a higher oscillation frequency and a smaller oscillation amplitude. The frequencies and decreasing trend in amplitude are similar to Richard et al.'s [29].

Richard et al. [29] also observed that oscillation frequency varied inversely with the total flow depth. Fig. 9.10 shows the kinetic energy fluctuations obtained for different values of  $H$ . The decrease in frequency with the increase in flow height is almost proportional.

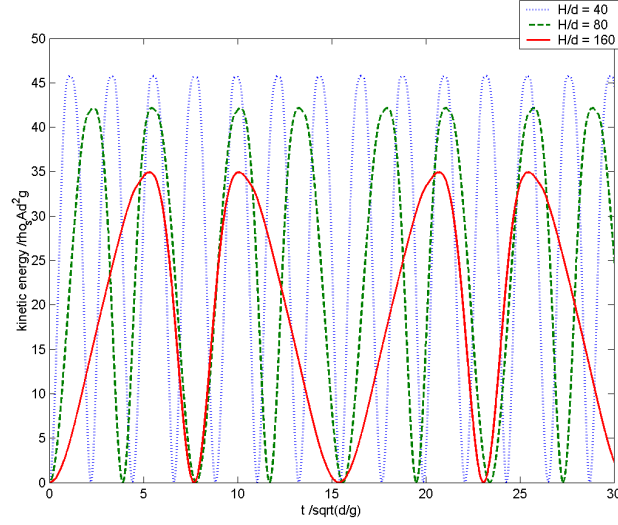


Figure 9.10: Oscillations in kinetic energy corresponding to small perturbations about the unstable force-equilibrium point  $v_b$ . Here  $v^*$  is taken to be 0.05 of the distance from the local maxima to  $v_b$ . Stiffness is  $K=2 \times 10^4$  mg/d; equilibrium points are  $v=0.581$ , 0.621 and 0.700; and the initial conditions are  $v_1 = 3(v_b - v^*)$ , and  $\dot{v}_1 = 0$ . Total flow depth  $H = 40d$  (dotted line),  $80d$  (dashed line) and  $160d$  (solid line) respectively.

## 9.2 Non-homogeneous Phase Transition

For the non-homogeneous system we use the model shown in figure 9.11. Here,  $y = Y + y_1(t, Y)$  is the displacement in the direction normal to flow,  $V \equiv \frac{\partial y}{\partial t} = V_1(t, Y)$  is the normal component of the velocity,  $v = v_0 + v_1(t, Y)$  is the solid volume fraction and  $p = p_0(Y) + p_1(t, Y)$  is the pressure of the dense inclined shear flow of average depth  $H$ . In the steady state  $0 \leq Y \leq H$ ,  $v_0$  is a constant and  $p_0 = (H - Y)\rho_s v_0 g \cos \phi + p_H$ , where  $p_H$  is some pressure overload, and, assuming an isothermal system,  $p_0(Y)$  gives rise to a granular temperature of  $T = T_0(Y)$ . The rate-dependent collisional shear stress is  $\mu (\partial V_1 / \partial y)$ , where  $\mu = (8/5) \sqrt{T_0} / \pi \rho_s v_0 d G_0$ , as given by Jenkins and Savage [15]. Because the particles are not spherical,  $0.05\mu$  is used. Terms with subscript 1 are assumed to be small

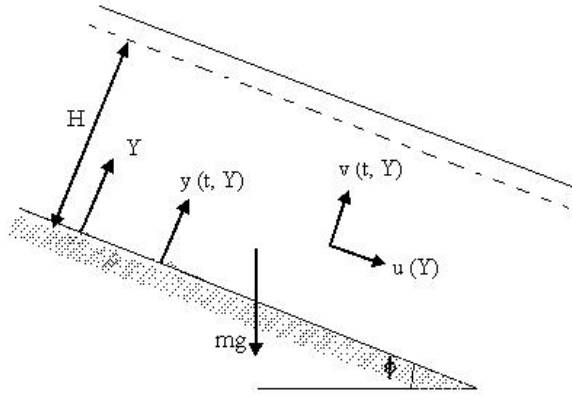


Figure 9.11: Non-homogeneous phase transition model

such that their products are negligible.

Using primes and overhead dots to denote differentiation with respect to  $Y$  and  $t$  respectively, the equations of mass and flow momentum are

$$\rho y' = \rho_0 \quad (9.11)$$

and

$$\rho (\dot{V} + VV') = \sigma_{YY}' - \rho g \cos \phi . \quad (9.12)$$

Using  $\rho = \rho_s (v_0 + v_1)$  in the mass balance yields

$$v_1 + v_0 y_1' = 0 , \quad (9.13)$$

and differentiating this with respect to time gives

$$\dot{v}_1 = -v_0 V_1' . \quad (9.14)$$

Substituting  $\sigma_{YY} = -(p_0 + p_1) + \mu \frac{\partial v_1}{\partial y}$  into the momentum balance results in

$$\begin{aligned} \dot{V}_1 = & -\frac{1}{\rho_s v_0} p_1' + \frac{\mu}{v_0} \left( V_1'' (y_1')^{-1} - V_1' (y_1')^{-2} y_1'' \right) \\ & + \frac{1}{v_0} \mu' V_1' - \frac{v_1}{v_0} g \cos \phi , \end{aligned} \quad (9.15)$$

where  $\mu' = (8/5)\rho_s v_0 d G_0 T_0' / \sqrt{T_0} \pi$ .

The pressure fluctuation due to collisions is described by the cubic function

$$p_{1,collisions} = \rho_s T_0 C_1 (v_1 - v_a)(v_1 - v_b)(v_1 - v_c) , \quad (9.16)$$

where  $v_a, v_b,$  and  $v_c$  are now all relative to  $v_0$ .

The spatial derivative of pressure fluctuation due to contact and collisions is described by

$$\begin{aligned} p_{1,contact}' &= p_{1,collisions}' - \sigma_{33}' \\ &= \rho_s T_0 C_1 [(v_1 - v_a)(v_1 - v_b) + (v_1 - v_a)(v_1 - v_c) + (v_1 - v_b)(v_1 - v_c)] v_1' \\ &\quad + \rho_s T_0' C_1 (v_1 - v_a)(v_1 - v_b)(v_1 - v_c) \\ &\quad + \frac{v_0 k}{4\pi d} K \left( 2 + \frac{8}{5} \epsilon \right) v_1' . \end{aligned} \quad (9.17)$$

After non-dimensionalising lengths with  $d$ , time with  $\sqrt{d/g}$ ,  $p_0$  and  $p_1$  with  $\rho_s g d$ , and  $T_0$  with  $g d$ , the system of ordinary differential equations for the non-dimensional variables  $y_1, v_1$  and  $v_1$  becomes

$$\dot{y}_1 = V_1 , \quad (9.18)$$

$$\dot{V}_1 = -\frac{1}{v_0} p_1' + \frac{8}{5} \sqrt{\frac{T_0}{\pi}} G_0 (V_1'' (y_1')^{-1} - V_1' (y_1')^{-2} y_1'') \quad (9.19)$$

$$+ \frac{4}{5} \frac{G_0}{\sqrt{T_0} \pi} T_0' V_1' - \frac{v_1}{v_0} \cos \phi , \quad (9.20)$$

and

$$\dot{v}_1 = -v_0 V_1' , \quad (9.21)$$

with the non-dimensional  $p_1$ :

$$\begin{aligned} p_{1,collisions}' &= T_0 C_1 [(v_1 - v_a)(v_1 - v_b) + (v_1 - v_a)(v_1 - v_c) + (v_1 - v_b)(v_1 - v_c)] v_1' \\ &\quad + T_0' C_1 (v_1 - v_a)(v_1 - v_b)(v_1 - v_c) , \end{aligned} \quad (9.22)$$

and

$$p_{1,contact}' = p_{1,collisions}' + \frac{1}{\rho_s g d} \frac{\nu_0 k}{4\pi d} K \left( 2 + \frac{8}{5} \epsilon \right) \nu_1'. \quad (9.23)$$

Boundary conditions are  $y_1 = 0$  and  $V_1 = 0$  at the base of the flow and  $-p_1 + \mu (\partial V_1 / \partial y) = 0$  at the top of the flow.

## 9.2.1 Discretised system

### Crude approximation

The system described above contains all the physics we believe to be relevant, however we prefer to start with as simple a computation as possible. Initial computations found  $y_1 \approx O(10^{-3})$ , so  $y \approx Y$ , leaving us with two dependent variables  $V_1$  and  $\nu_1$ . In a first computation, we assume no overload and employ a uniform granular temperature  $T_0$ . This is not strictly appropriate, however we believe that such a computation still captures the essence of the problem. Lastly, instead of the composite pressure-volume fraction relationship, we consider only the collisional cubic curve  $p_1/T_0 = C_1 (\nu_1 - \nu_a)(\nu_1 - \nu_b)(\nu_1 - \nu_c)$ . The system of ordinary differential equations is then simplified to

$$\dot{V}_1 = -\frac{1}{\nu_0} \left( \frac{\partial p_1}{\partial \nu_1} \nu_1' \right) + \frac{8}{5} \sqrt{\frac{T_0}{\pi}} G_0 V_1'' - \frac{\nu_1}{\nu_0} \cos \phi, \quad (9.24)$$

and

$$\dot{\nu}_1 = -\nu_0 V_1'. \quad (9.25)$$

In what follows, terms with subscript 0 still refer to the equilibrium state, but other subscripts correspond to the integration points ( $1 \leq j \leq n$ ). The discretised

form of the simplified system is then

$$\begin{aligned}
j = 1 \ (Y = 0) & : \begin{cases} \dot{V}_1 = 0 \\ \dot{v}_1 = -v_0 \left( \frac{V_2}{H/(n-1)} \right) \end{cases} \\
2 \leq j \leq n-1 & : \begin{cases} \dot{V}_j = -\frac{1}{v_0} p'_{1,j} + \frac{8}{5} \sqrt{\frac{T_0}{\pi}} G_0 \frac{V_{j+1} - 2V_j + V_{j-1}}{(H/(n-1))^2} - \frac{v_j}{v_0} \cos \phi \\ \dot{v}_j = -v_0 \left( \frac{V_{j+1} - V_{j-1}}{2H/(n-1)} \right) \end{cases} \\
j = n \ (Y = H/d) & : \begin{cases} \dot{V}_n = -\frac{1}{v_0} p'_{1,n} + \frac{1}{v_0} p_{1,n} \frac{(n-1)}{H} - \frac{8}{5} \sqrt{\frac{T_0}{\pi}} G_0 \frac{V_{n-1} - V_{n-2}}{(H/(n-1))^2} - \frac{v_n}{v_0} \cos \phi \\ \dot{v}_n = -\frac{5}{8G_0} \sqrt{\frac{\pi}{T_0}} p_{1,n} \end{cases}
\end{aligned} \tag{9.26}$$

where

$$\begin{aligned}
p'_{1,j} & = T_0 C_1 \left[ (v_j - v_a)(v_j - v_b) + (v_j - v_a)(v_j - v_c) + (v_j - v_b)(v_j - v_c) \right] \\
& \quad \times \frac{v_{j+1} - v_{j-1}}{2H/(n-1)}
\end{aligned} \tag{9.27}$$

for  $2 \leq j \leq n-1$ , and

$$p'_{1,n} = T_0 C_1 (v_a v_b + v_a v_c + v_b v_c) \frac{-v_{n-1}}{H/(n-1)}. \tag{9.28}$$

Two stability criteria were used as a check on the size of the time-step in the computations:  $\Delta t \leq \Delta Y/c$  and  $\Delta t \leq (\Delta Y)^2/2\beta$ , where  $c \approx \sqrt{\partial p_1/\partial v_1}$  is an approximate dimensionless wave speed and  $\beta \approx \mu/v_0$  is an approximate dimensionless diffusion coefficient.

For the following results, the initial conditions used were  $V_1(Y) = 0$  and  $v_1(Y) = -10^{-4}(1 - Y/H)$ , as if the system were compressed and then released.

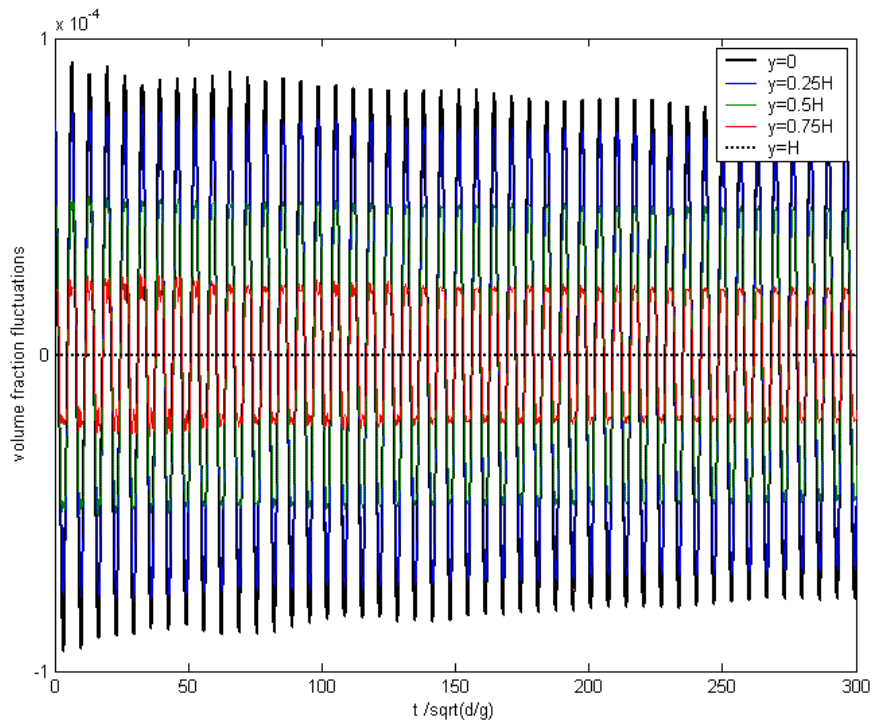


Figure 9.12: Volume fraction fluctuations against time.  $\nu_a = 0$ ,  $\nu_b = 0.04$ ,  $\nu_c = 0.119$ .

Figure 9.12 shows the volume fraction fluctuations when the steady state  $\nu_0 = 0.581$ , i.e. on the far left of the cubic curve. Small oscillations of frequency  $0.15 \sqrt{g/d}$  about the origin are obtained, which decay to values very close to zero. This is similar to what is obtained with the perturbation model based on kinetic theory, which only sees the random collisional regime of the cubic curve.

Near the local maxima, because of the close proximity of  $\nu_a$  and  $\nu_b$ , it is easy for the system to perform excursions in  $\nu_1$  that traverse the distance between both equilibrium points and, because of inertia, travel past the stable equilibrium point  $\nu_c$  on the right, as shown in figure 9.13). Here, the system settles into a steady state with an inhomogeneous volume fraction. Figure 9.14 shows the obtained steady state results and predicted steady state solution, which is

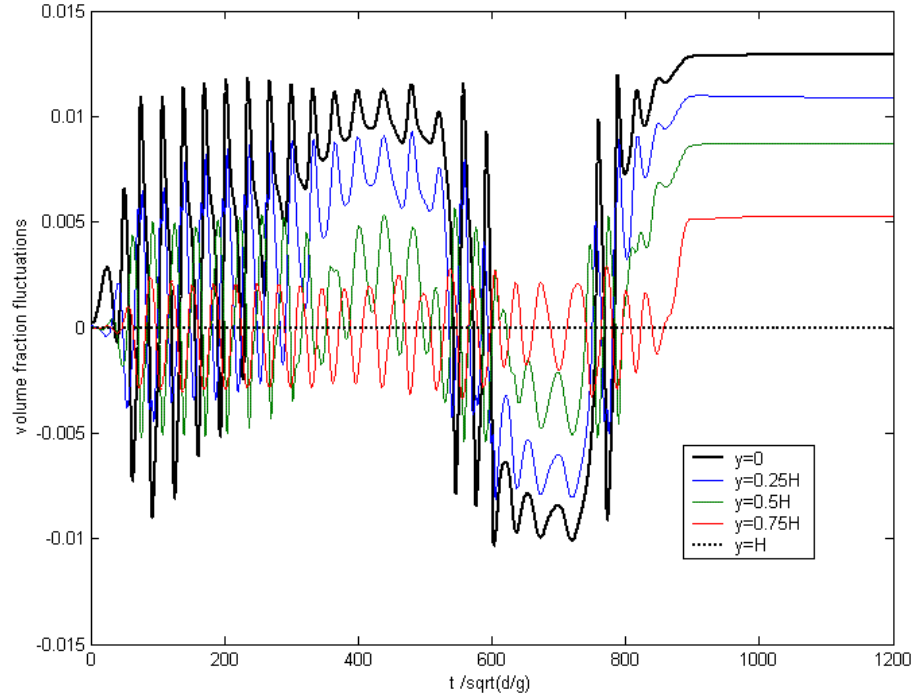


Figure 9.13: Volume fraction fluctuations against time.  $\nu_a = 0$ ,  $\nu_b = 0.0002$ ,  $\nu_c = 0.0012$ .

obtained by solving equation 9.24 when  $V_1$  and its derivatives are zero:

$$\frac{Y}{H} = C_3 - \frac{T_0 C_1}{H \cos \phi} \left[ \frac{3}{2} \nu_1^2 - 2\nu_1 (\nu_a + \nu_b + \nu_c) + (\nu_a \nu_b + \nu_a \nu_c + \nu_b \nu_c) \ln |\nu_1| \right]. \quad (9.29)$$

Past the local maxima,  $\nu_0$  corresponds to the unstable force-equilibrium point  $\nu_b$ . The initial perturbation from the origin results in volume fraction fluctuations similar to that observed previously, i.e.  $\nu_1$  traverses all three force-equilibrium points, shown in figure 9.15. Again, the system reaches a steady state corresponding to the predicted steady state solution (Figure 9.16). Note that this steady state solution is different from that obtained when  $\nu_0$  corresponded to the leftmost stable force-equilibrium point; in fact, a different steady state solution is obtained for each  $\nu_0$  because of the changing values of  $\nu_a$ ,  $\nu_b$  and  $\nu_c$ .

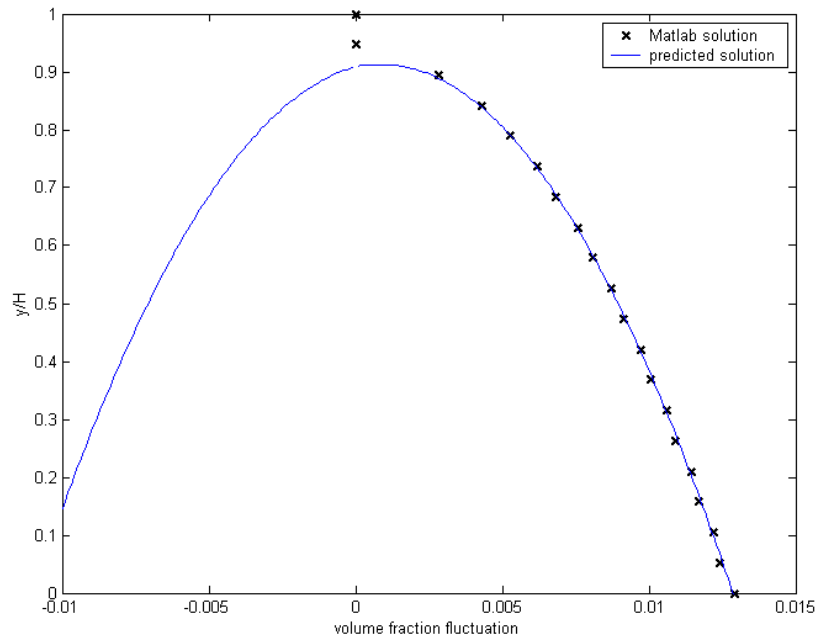


Figure 9.14: Steady state results and predicted solution for  $\nu_a = 0$ ,  $\nu_b = 0.0002$ ,  $\nu_c = 0.0012$ .

The large volume fraction excursions in figure 9.15 have a frequency of  $0.025 \sqrt{g/d}$ . In order to compare this to Richard's results that employ a linear stiffness, we compute the normal particle stiffness  $K$  corresponding to our current system by equating the stiffness  $\partial P_1/\partial Y$  at  $\nu_c$  to the stiffness expression in equation 9.8. This gives us  $K \approx 0.15 \text{ mg/d}$ . From figure 9.1, a frequency of  $4.5 \sqrt{g/d}$  is obtained for  $K = 2e6 \text{ mg/d}$ ; scaling our results up to  $K = 1.5 \times 10^6 \text{ mg/d}$  gives us a frequency of  $79 \sqrt{g/d}$  which is 20 times larger than Richard et al.'s frequency.

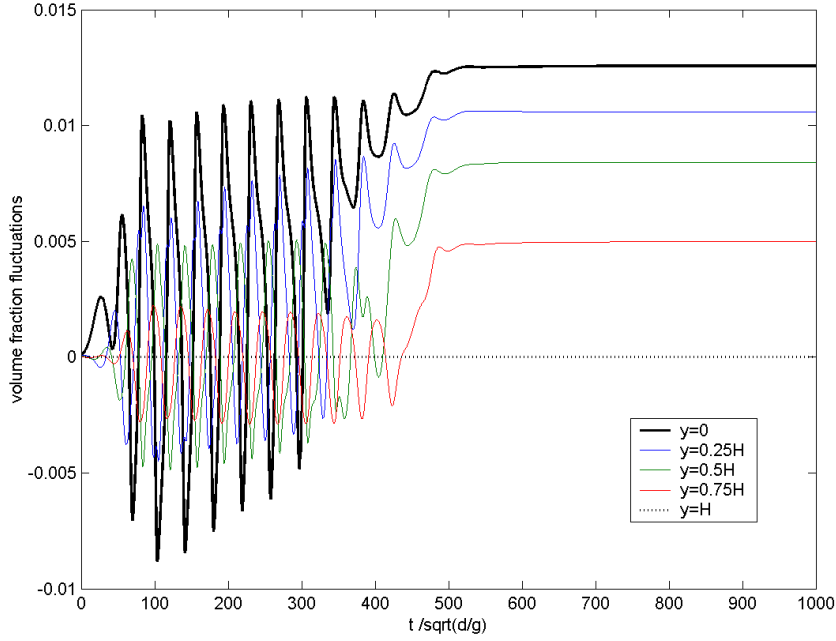


Figure 9.15: Volume fraction fluctuations against time.  $\nu_0 = 0.5993, \nu_a = -0.0002, \nu_b = 0, \nu_c = 0.001$ . Initial perturbation in  $\nu_1$  varies linearly from 0.0001 at base to 0 at surface.

### Non-homogeneous $T_0$

When the temperature  $T_0$  varies with depth, the system of coupled equations is

$$\dot{V}_1 = -\frac{1}{\nu_0} p_1' + \frac{8}{5} \sqrt{\frac{T_0}{\pi}} G_0 V_1'' + \frac{4}{5} \frac{G_0}{\sqrt{T_0} \pi} T_0' V_1' - \frac{\nu_1}{\nu_0} \cos \phi, \quad (9.30)$$

and

$$\dot{\nu}_1 = -\nu_0 V_1', \quad (9.31)$$

with the non-dimensional  $p_1$

$$\begin{aligned} p_{1,collisions}' &= T_0 C_1 [(v_1 - \nu_a)(v_1 - \nu_b) + (v_1 - \nu_a)(v_1 - \nu_c) + (v_1 - \nu_b)(v_1 - \nu_c)] \nu_1' \\ &\quad + T_0' C_1 (v_1 - \nu_a)(v_1 - \nu_b)(v_1 - \nu_c). \end{aligned} \quad (9.32)$$

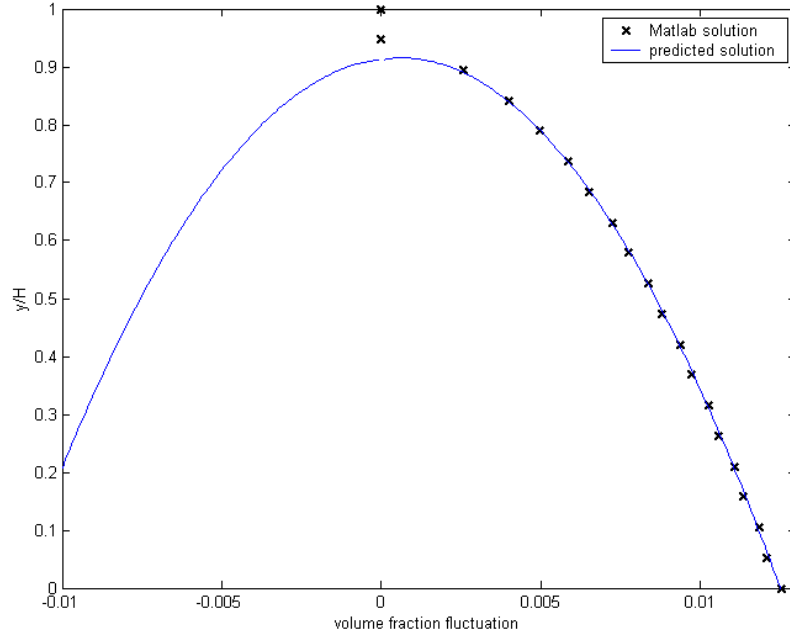


Figure 9.16: Steady state results and predicted solution for  $v_a = -0.0002$ ,  $v_b = 0$ ,  $v_c = 0.001$ .

The discretised form of equations 9.30 and 9.31 is

$$\begin{aligned}
 j = 1 \ (Y = 0) & : \begin{cases} \dot{V}_1 = 0 \\ \dot{v}_1 = -v_0 \left( \frac{V_2}{H/(n-1)} \right) \end{cases} \\
 2 \leq j \leq n-1 & : \begin{cases} \dot{V}_j = -\frac{1}{v_0} p_{1,j}' - \frac{T_{0,j}'}{v_0} \frac{p_{1,j}}{T_{0,j}} + \frac{8}{5} \sqrt{\frac{T_{0,j}}{\pi}} G_0 \\ \quad + \frac{4}{5} \frac{G_0}{\sqrt{T_{0,j}\pi}} T_{0,j}' \frac{V_{j+1} - 2V_j + V_{j-1}}{(H/(n-1))^2} - \frac{v_j}{v_0} \cos \phi \\ \dot{v}_j = -v_0 \left( \frac{V_{j+1} - V_{j-1}}{2H/(n-1)} \right) \end{cases} \\
 j = n \ (Y = H/d) & : \begin{cases} \dot{V}_n = -\frac{1}{v_0} p_{1,n}' - \frac{T_{0,n}'}{v_0} \frac{p_{1,n}}{T_{0,n}} + \frac{1}{v_0} p_{1,n} \frac{(n-1)}{H} \\ \quad - \frac{8}{5} \sqrt{\frac{T_{0,n}}{\pi}} G_0 + \frac{4}{5} \frac{G_0}{\sqrt{T_{0,n}\pi}} T_{0,n}' \frac{V_{n-1} - V_{n-2}}{(H/(n-1))^2} - \frac{v_n}{v_0} \cos \phi \\ \dot{v}_n = -\frac{5}{8G_0} \sqrt{\frac{\pi}{T_{0,n}}} p_{1,n} \end{cases}
 \end{aligned} \tag{9.33}$$

where

$$p_{1,j}' = T_0 C_1 \left[ (v_j - v_a)(v_j - v_b) + (v_j - v_a)(v_j - v_c) + (v_j - v_b)(v_j - v_c) \right] \times \frac{v_{j+1} - v_{j-1}}{2H/(n-1)}, \quad (9.34)$$

and

$$T_{0,j}' = \frac{T_{0,j+1} - T_{0,j-1}}{2H/(n-1)} \quad (9.35)$$

for  $2 \leq j \leq n-1$ , and

$$p_{1,n}' = T_0 C_1 (v_a v_b + v_a v_c + v_b v_c) \frac{-v_{n-1}}{H/(n-1)}, \quad (9.36)$$

and

$$T_{0,n}' = \frac{T_{0,n} - T_{0,n-1}}{H/(n-1)}. \quad (9.37)$$

The following results were obtained with a distribution for  $T_0$ , decreasing linearly in  $Y$ , but non-zero at  $Y = H$ , and similar initial conditions to the first computation.

Figures 9.17 and 9.18 show the volume fraction fluctuations for  $v_0$  corresponding to a stable and an unstable force-equilibrium respectively. At the stable force-equilibrium, the oscillations of frequency  $0.12 \sqrt{g/d}$  decay to almost-zero values. At the unstable force-equilibrium the volume fraction exhibits large excursions of frequency  $0.033 \sqrt{g/d}$  encompassing all three force-equilibrium points, before reaching an steady state inhomogeneous in volume fraction. These results are similar to those obtained for constant  $T_0$ , which supports the idea that the crude approximation still contains all the essential physics.

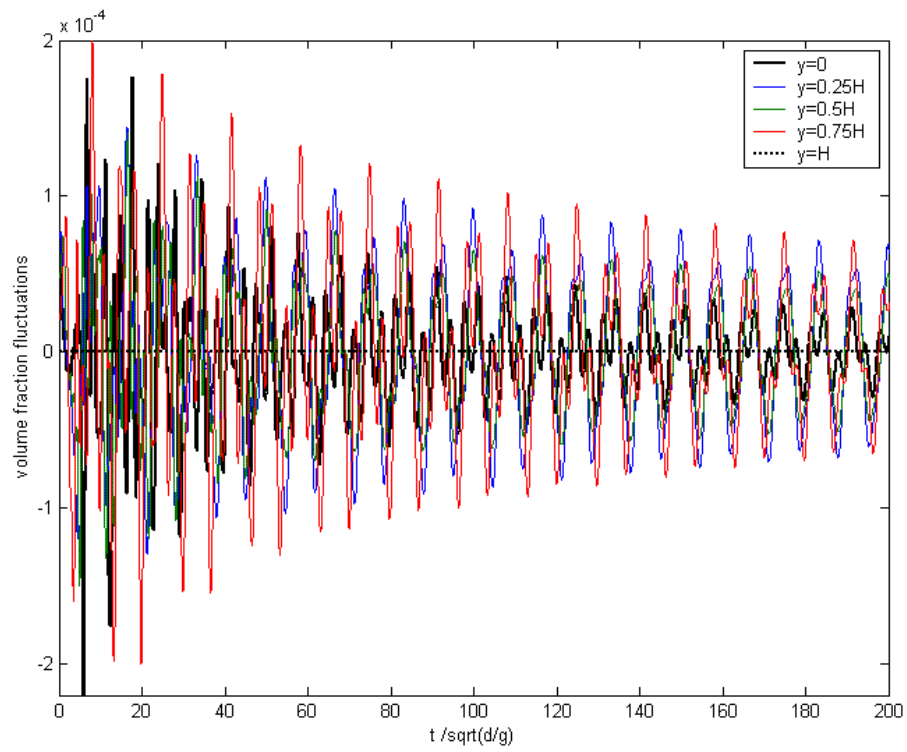


Figure 9.17: Volume fraction fluctuations against time for varying  $T_0$ .  $\nu_a = 0$ ,  $\nu_b = 0.0002$ ,  $\nu_c = 0.0012$ .

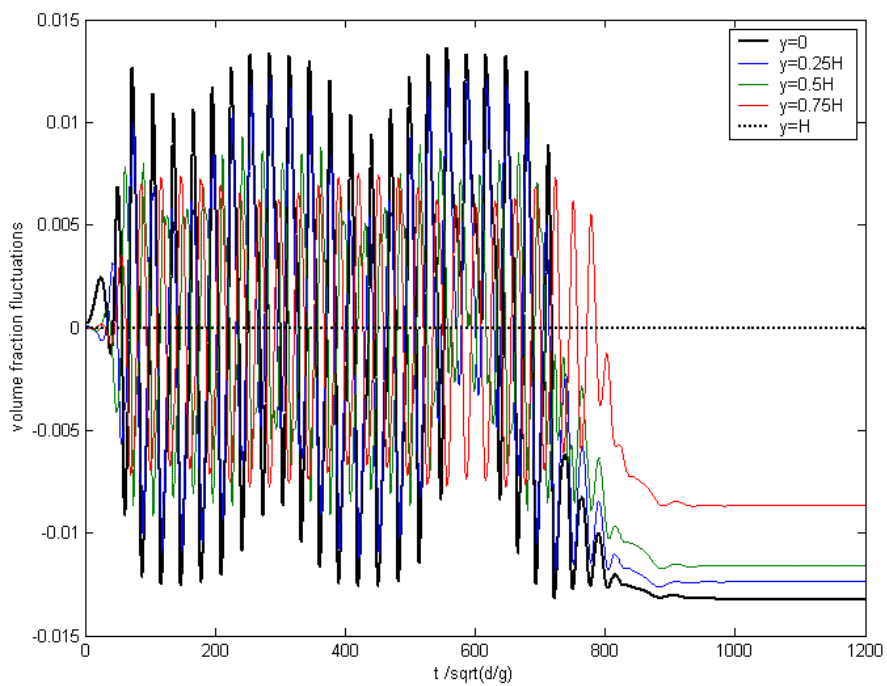


Figure 9.18: Volume fraction fluctuations against time for varying  $T_0$ .  $\nu_a = -0.0002$ ,  $\nu_b = 0$ ,  $\nu_c = 0.001$ .

## CHAPTER 10

### SUMMARY

The main results from the experiments are listed in Tables 10.1 and 10. The large inclined chute and big shaker experiments are excluded as no ‘burping’ was produced.

A perturbation model, based on kinetic theory, was used to predict the oscillation frequency of an inclined shear flow. The initial model was a fully-dense flow, but the measured inclination angle was larger than the maximum angle for which the theory remained valid, because of the presence of sidewalls. Indeed using a lower inclination angle yielded a frequency of 133 Hz, which is within the broadband frequency range detected by the microphone during the experiments.

This model was improved to have a dilute layer above the dense layer to accommodate the larger inclination angle sustained by having sidewalls. However because the theory was based on spherical particles, the low value of effective restitution coefficient employed was insufficient to account for energy dissipation, which resulted in underestimation of the dense layer height. A sensitivity to the average volume fraction also caused the predicted frequencies being much lower than that detected in the small inclined chute and rotating flask.

Finally, a phase transition model was inspired by Silbert’s [33] numerical simulations in which he observed oscillations in inclined flow near stopping angles. The model uses a cubic curve to represent the phase change between random packing and ordered packing in the collisional regime, with a straight line

Table 10.1: Experimental Results Summary - Avalanching and Shearing

Motion Type	Avalanching		Shearing with a stylus
	Small Chute	Rotating Flask	
Motion	Flow over inclined heap in narrow (25 diameters) chute with sidewalls, from hopper overhead.	Material in 4-litre glass flask, rotating at $\approx 100$ rpm about long axis.	Stylus dragged through surface of material.
Frequency (Hz)	90-145	100-150	150-600 possible
Observations	Very low amplitude. Broadband peak present only with high flowrate.	Very low amplitude. Broadband peak at tail-end of Helmholtz frequency (88.9 Hz); present only at high rotation speed.	<p>Freq <math>\downarrow</math> if</p> <ul style="list-style-type: none"> <li>• velocity <math>\downarrow</math></li> <li>• stylus width <math>\uparrow</math></li> <li>• force applied <math>\uparrow</math></li> <li>• close to sidewalls</li> <li>• strokes are shallow (not obvious)</li> </ul> <p>Amplitude <math>\uparrow</math> if velocity <math>\uparrow</math>.</p>

Table 10.2: Experimental Results Summary - Pouring

Motion Type	Pouring		
	Jar Shaking	Bucket Pouring	Tube Sliding
Motion	Partially-filled glass jar shaken at $\approx 2\text{Hz}$ and 10cm amplitude.	Material poured from one rigid bucket into another.	Long tube tilted upwards from horizontal about one end.
Frequency (Hz)	$\approx 100$	$\approx 500$ , drops to and stays at $\approx 250$	$\approx 170$
Observations	Amount of material required minimal, but best results if $\frac{1}{3} - \frac{1}{2}$ full.	Freq $\downarrow$ if flowrate $\uparrow$ .	Tube has to be tilted to an angle $> 60^\circ$ . Sound produced even when tilting is slow.

representing additional pressure due to particles forming chains. This model exhibits oscillations of significant amplitude when past the local maxima in the curve, which corresponds to the appearance of oscillations below a particular inclination angle. At higher particle stiffness, the curve is contracted, which results in higher oscillation frequencies and smaller amplitudes; this agrees with further observations made by Richard [29]. However, the oscillation frequency obtained with the model for an inhomogeneous system is 20 times larger than that obtained by Richard at a similar particle stiffness. While this model produces oscillations in an inclined flow, it is not certain that the sound produced is related to 'burping'.

The earlier version of the perturbation model, with a fully-dense layer, is similar to the phase transition model when the steady state corresponds to a stable force-equilibrium point i.e. the system produces small oscillations about its steady state in the random collisional regime. However the perturbation model is based on kinetic theory which requires the existence of chains of particles in its dense flow, and hence the perturbation model's steady state is much closer in volume fraction to the contact branch, than the left-most part of the cubic collisional curve in the phase transition model.

## CHAPTER 11

### FUTURE WORK

Regarding the work reported here, there are still improvements to be made. One of the most obvious is to acquire quantitative data on the relationship between the frequency produced during stroking and the force applied to the stylus. This would likely involve an automated system so that each factor involved in stroking can be controlled independently of each other. An automated system to perform jar-shaking would also be beneficial to provide information on the necessary displacement and acceleration, and facilitate a closer study.

Another important issue is the relationship between stroking and pouring. Since they both involve shearing to some extent, yet appear to have contradicting frequency-velocity trends, it would be interesting to determine how two different mechanisms could produce such similarly-related sounds, or if, perhaps, they are in reality the same mechanism.

To some extent, stroking could be modelled in a way similar to avalanching. Instead of an inclined flow, the steady state would be a horizontal sheared flow, between some depth of pushed sand above it and a layer of stationary sand underneath it. The motion of the stylus causes the shearing motion and, assuming that force applied on the stylus is purely vertical, that would translate to an additional pressure overload. In this situation, however, the kinetic theory previously applied to avalanching cannot be used here directly to provide expressions for the steady state packing fraction and granular temperature due to zero inclination. Disregarding this, the solution obtained for normal velocity perturbations would appear similar to the solutions obtained for inclined flow with both dense and dilute layers, and would depend on the heights of both the

layer being sheared and the pushed sand above it.

For ‘sounding’ sand, humidity plays an important role in the ability to produce sound. However, we were unable to quantify the ‘humidity’ of the granular materials used in our experiments, and could only represent increasing water content indirectly through the passing of time after removal from the oven. Hence, it would be extremely useful to determine an exact ‘humidity’ at any particular time; to state quantitatively what effect this humidity has on the mechanical properties of granular material, and to identify those parameters required for numerical simulations such as frictional coefficients, particle stiffness and the coefficient of restitution.

An overlooked issue in our experiments was the effect of electrostatics. Newly-dried sand was very highly charged, particularly the Dumont and Eureka dune sands, as they have small particle diameters. Electrostatics was not a significant issue in the pouring and stroking experiments, but in the inclined chute and rotating flask setups, the sand was observed to stick to the walls and valve, possibly hindering the flow and, hence, the ‘just dried’ results. Dried sand kept in a tightly closed jar could still ‘burp’ audibly after a lengthy period of time, when electrostatic effects had disappeared, so electrostatics was deemed insignificant in terms of producing sound from sand. However it does affect the flow velocity and possibly changes the boundary conditions.

As mentioned at the end of the chapter on the kinetic theory model for inclined shear flow, the sensitivity of oscillation frequency to the average volume fraction in the dense layer could possibly be explored through the use of numerical simulations. It would also be advantageous to investigate the average stress ratio in the dense layer, as there are suspicions of it being overestimated

by the theory.

Finally, the phase transition model leaves a lot of room for further improvement. Here an asymmetric cubic curve was used to approximate the composite curve, with the right-hand slope being much steeper than both the left-hand slope and the negative slope in the middle. There is the possibility of using a 4th-order polynomial to retain the two smaller slopes as well as the larger slope on the right, which would model the difference in stiffnesses in the collisional cubic curve and the contact branch better. Also, the model could be expanded to an adiabatic system, i.e.  $T = T_0(Y) + T_1(t, Y)$ . Finally, because particle stiffness has an effect during collisions, it should have some effect on the amount of energy dissipated. There is also the possibility that this effect is different during the collisional regime and when particle chains start forming.

APPENDIX A  
**SEISMIC REFRACTION SURVEY**

Waves are initiated from a source at the surface. Upon encountering a boundary delineating regions of different density, some of these waves are reflected back, while the rest are refracted. Because the density of the material is higher than the air, the waves travel at a higher velocity than those in air and, hence, beyond a certain distance from the source, critically refracted waves reach geophones, which are arranged linearly over the surface, faster than the direct waves do. Figure A.1 shows a sketch of some first-arrival waves refracted from increasingly dense layers.

Given that the boundary and surface are approximately parallel, the time lag in first-arrivals between two consecutive geophones is equal to the distance between them divided by the velocity of the layer. Consequently, in a plot of travel-times against the positions of the geophones, the slope is the reciprocal of the velocity. A change in slope indicates a change in velocity and, hence, implies the presence of a denser layer. Knowing the velocity of an upper layer then allows for the calculation of the thickness of the denser layer immediately below it. Consequently the various velocities and layer thicknesses can be calculated starting from the surface downwards [12, 20, 26].

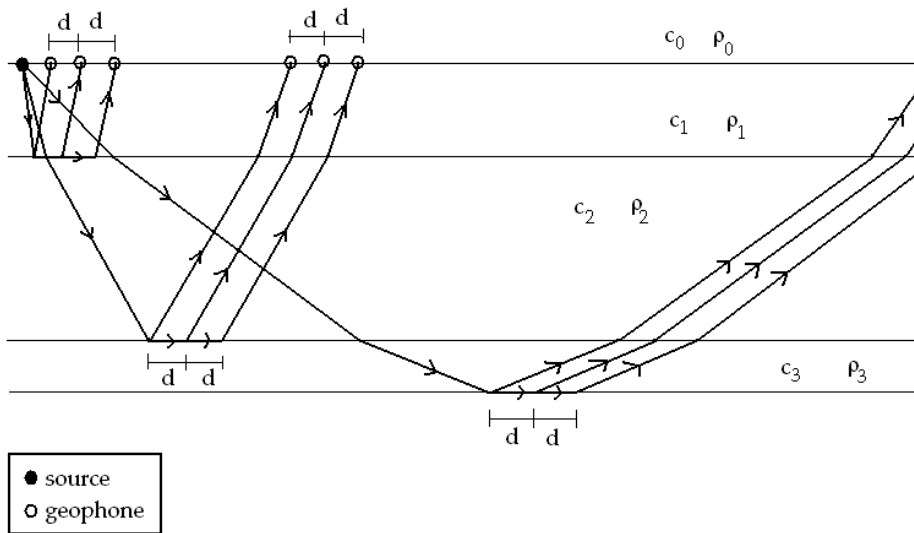


Figure A.1: Seismic Refraction Survey

## APPENDIX B

### ‘DEPTH-AVERAGE’ PDE APPROXIMATE SOLUTION

The PDE with depth-averaged coefficients for the dense shear flow is:

$$\ddot{\tilde{v}}_1 = \tilde{v}_1'' \left[ \frac{1.20 - \nu_0}{2(0.60 - \nu_0)} \right] + \tilde{v}_1' \left( \frac{-0.60}{0.60 - \nu_0} \right). \quad (\text{B.1})$$

Assuming the solution is separable so that  $\tilde{v}_1(\tilde{t}, \tilde{y}) = \Gamma(\tilde{t})Y(\tilde{y})$ , we obtain

$$\Gamma(\tilde{t}) = a_1 \sin \lambda \tilde{t} + a_2 \cos \lambda \tilde{t} \quad (\text{B.2})$$

for the temporal part, and two solutions for the spatial part:

$$Y(\tilde{y}) = b_1 \exp \left[ \left( \frac{B}{A} + \frac{\sqrt{B^2 - 2A\lambda^2}}{A} \right) \tilde{y} \right] + b_2 \exp \left[ \left( \frac{B}{A} - \frac{\sqrt{B^2 - 2A\lambda^2}}{A} \right) \tilde{y} \right] \quad (\text{B.3})$$

and

$$Y(\tilde{y}) = b_3 \tilde{y} \exp \left[ \frac{B}{A} \tilde{y} \right] + b_4 \exp \left[ \frac{B}{A} \tilde{y} \right], \quad (\text{B.4})$$

where  $A = (1.20 - \nu_0) / (0.60 - \nu_0)$  and  $B = 0.60 / (0.60 - \nu_0)$  are both constants, and

$$k = \frac{B}{A} \pm \frac{\sqrt{B^2 - 2A\lambda^2}}{A}.$$

These two solutions correspond to the cases in which  $k$  has two distinct real values, or only one. Assuming no-slip conditions at the base of the flow  $\tilde{y} = 0$ , the spatial parts become

$$Y(\tilde{y}) = b_1 \exp \left( \frac{B}{A} \tilde{y} \right) \sinh \left( \frac{\sqrt{B^2 - 2A\lambda^2}}{A} \tilde{y} \right) \quad (\text{B.5})$$

and

$$Y(\tilde{y}) = b_3 \tilde{y} \exp \left( \frac{B}{A} \tilde{y} \right). \quad (\text{B.6})$$

The Taylor expansion about 0 of  $\sinh x \approx x$ , for small  $x$ , so equations B.5 and B.6 are approximately equal for  $0 < \tilde{y} < 1$ . Therefore, we can take  $k$  to have

only one distinct real root, and equation B.6 as the solution. For this to be true,  $\lambda = B/\sqrt{2A}$ . Combining equations B.2 and B.6, the non-dimensional solution for the normal velocity is then

$$\tilde{v}_1(\tilde{t}, \tilde{y}) = \tilde{y} \exp\left(\frac{B}{2A}\tilde{y}\right) \left[ c_1 \sin\left(\frac{B}{\sqrt{2A}}\tilde{t}\right) + c_2 \cos\left(\frac{B}{\sqrt{2A}}\tilde{t}\right) \right]. \quad (\text{B.7})$$

## BIBLIOGRAPHY

- [1] Vibrationdata. [www.vibrationdata.com/Newsletters/March2006\\_NL.pdf](http://www.vibrationdata.com/Newsletters/March2006_NL.pdf).
- [2] B. Andreotti. The song of dunes as a wave-particle mode locking. *Phys. Rev. Lett.*, 93(238001), 2004.
- [3] B. Andreotti and L. Bonneau. Booming dune instability. *Phys. Rev. Lett.*, 103(238001), 2009.
- [4] R. A. Bagnold. *The Physics of Blown Sand and Desert Dunes*. Chapman & Hall Ltd, 2 edition, 1954.
- [5] H. Bailey. Motion of a hanging chain after the free end is given an initial velocity. *American J. Physics*, 68(8):764–767, 2000.
- [6] D. Berzi and J. T. Jenkins. Surface flows of inelastic spheres. *Phys. Fluids*, 23(013303), 2011.
- [7] D. A. Bies and C. H. Hansen. *Engineering Noise Control: Theory and Practice*. Spon Press, 4 edition, 2009.
- [8] D. Criswell, J. Lindsay, and D. Reasoner. Seismic & acoustic emissions of a booming dune. *J. Geophysical Research*, 80(35):4963–4974, 1975.
- [9] S. Dagois-Bohy, S. Ngo, S. Courrech du Pont, and S. Douady. Laboratory singing sand avalanches. *Ultrasonics*, 50:127–132, 2010.
- [10] S. Douady, A. Manning, P. Hersen, H. Elbelrhiti, S. Protiere, A. Daerr, and B. Kabbachi. Song of the dunes as a self-synchronised instrument. *Phys. Rev. Lett.*, 97(018002), 2006.
- [11] D. W. Humphries. The booming sand of korizo, sahara, and the squeaking sand of gower, s. wales: A comparison of the fundamental characteristics of two musical sands. *Sedimentology*, 6:135–152, 1966.
- [12] Enviroscan Inc. Seismic refraction versus reflection, 2009. [www.enviroscan.com/html/principles.html](http://www.enviroscan.com/html/principles.html).
- [13] J. T. Jenkins. Dense shearing flows of inelastic disks. *Phys. Fluids*, 18(103307), 2006.

- [14] J. T. Jenkins and D. Berzi. Dense inclined flows of inelastic spheres: Tests of an extension of kinetic theory. *Granular Matter*, 12(2):151–158, 2010.
- [15] J. T. Jenkins and S. B. Savage. A theory for the rapid flow of identical, smooth, nearly elastic, spherical particles. *J. Fluid Mech.*, 130:187–202, 1983.
- [16] J. T. Jenkins and O. D. L. Strack. Mean-field inelastic behavior of random arrays of identical spheres. *Mech. Matls.*, 16:25–33, 1993.
- [17] M. Leach and H. Chartrand. Recent progress in the development of musical sand. *Progress in Acoustic Emission*, VII:499–504, 1994.
- [18] A. D. Lewis. Roaring sands of the kalahari desert. *South African Geographical J.*, 19(33):33–49, 1936.
- [19] J. Lindsay, D. Criswell, T. Criswell, and B. Criswell. Sound-producing dune & beach sands. *Geological Society of America Bulletin*, 87:463–473, 1976.
- [20] Geo-Services International (UK) Ltd. Seismic techniques, 1999. [www.geophysics.co.uk/mets3.html](http://www.geophysics.co.uk/mets3.html).
- [21] S. Luding, E. Clement, A. Blumen, J. Rajchenbach, and J. Duran. Anomalous energy dissipation in molecular-dynamics simulations of grains: The “detachment” effect. *Phys. Rev. E*, 50(5):4113–4122, 1994.
- [22] GDR MiDi. On dense granular flows. *Eur. Phys. J. E*, 14:341–365, 2004.
- [23] P. Mills and F. Chevoir. Rheology of granular materials and sound emission near the jamming transition. In M. Nakagawa and S. Luding, editors, *Powders and Grains 2009, Proceedings of the 6th International Conference on Micromechanics of Granular Media*, AIP Conference Proceedings 1145, pages 511–514, Golden, Colorado, 2009.
- [24] F. Nori, P. Sholtz, and M. Bretz. Booming sand. *Scientific American*, 277(3):64–69, 1997.
- [25] M. Nosonovsky and G. Adams. Dilatational and shear waves induced by the frictional sliding of two elastic half-spaces. *International Journal of Engineering Science*, 39:1257–1269, 2001.
- [26] C. B. Officer. *Introduction to the Theory of Sound Transmission*. McGraw-Hill Book Company, Inc, 1958.

- [27] J. H. Poynting and Sir J. J. Thomson. *A Text-book of Physics; Sound*. Charles Griffin & Company, Limited, 8th edition, 1922.
- [28] L. Quartier, B. Andreotti, S. Douady, and A. Daerr. Dynamics of a grain on a sandpile model. *Phys. Rev. E*, 62(6):8299–8307, 2000.
- [29] P. Richard, S. McNamara, and M. Tankeo. On the relevance of numerical simulations to booming sand. *Phys. Rev. Lett.* (under review), 2011.
- [30] E. J. Routh. *Advanced Part of a Treatise on the Dynamics of a System of Rigid Bodies*. Macmillan & Co., 5th edition, 1892.
- [31] S. W. Shaw and P. J. Holmes. A periodically forced piecewise linear oscillator. *J. Sound and Vibration*, 90(1):129–155, 1983.
- [32] P. Sholtz, M. Bretz, and F. Nori. Sound-producing sand avalanches. *Contemporary Physics*, 38(5):329–342, 1997.
- [33] L. E. Silbert. Temporally heterogeneous dynamics in granular flows. *Phys. Rev. Lett.*, 94(098002), 2005.
- [34] L. E. Silbert, G. S. Grest, and S. J. Plimpton. Boundary effects and self-organization in dense granular flows. *Phys. Fluids*, 14(8):2637–2646, 2002.
- [35] D. T. Trexler and W. N. Melhorn. Singing and booming sand dunes of california and nevada. *California Geology*, 39(7):147–152, 1986.
- [36] A. Vainchtein and P. Rosakis. Hysteresis and stick-slip motion of phase boundaries in dynamic models of phase transitions. *J. Nonlin. Sci.*, 9:697–719, 1999.
- [37] N. M. Vriend, M. L. Hunt, R. W. Clayton, C. E. Brennen, K. S. Brantley, and A. Ruiz-Angulo. Solving the mystery of booming sand dunes. *Geophysical Research Lett.*, 34(L16306), 2007.